國立交通大學

物理研究所

博士論文

兩個介觀物理的主題:
壹：低溫電子散射時間
貳：量子點中自旋傳輸

Two topics on mesoscopic electron transport:
Part Ⅰ：Low temperature electron dephasing time
Part Ⅱ： Spin transport in vertical double quantum dots

研究生：黃旭明

指導教授：林志忠 教授

中華民國九十七年七月

兩個介觀物理的主題:
壹：低溫電子散射時間
貳：量子點中自旋傳輸

Two topics on mesoscopic electron transport:
Part Ⅰ：Low temperature electron dephasing time
Part Ⅱ： Spin transport in vertical double quantum dots

研究生：黃旭明 Student：Shiu-Ming Huang
指導教授：林志忠 Advisor：Juhn-Jong Lin

國立交通大學
物理研究所
博士論文

A Thesis
Submitted to Institute of Physics
College of Science
National Chiao Tung University
in Partial Fulfillment of the Requirements
for the Degree of
Doctor
in

Physics

July 2008

Hsinchu, Taiwan, Republic of China

中華民國九十七年七月

A Thesis Done Under
NCTU-RIKEN Joint Graduate School Program

Student：Shiu-Ming Huang
NCTU Advisor：Juhn-Jong Lin
RIKEN Advisor：Kimitoshi Kono
Keiji Ono
Hideko Akimoto

兩個介觀物理的主題:

壹：低溫電子散射時間

貳：量子點中自旋傳輸

學生：黃旭明　　　　　　　　指導教授：林志忠　教授

國立交通大學物理研究所　博士班

摘　　要

在這本博士論文中，我們將討論兩個介觀物理的主題。第一個是銅鍺金合金薄膜在低溫下電子的非彈性散射時間的研究、第二個是電子在砷化鎵垂直雙量子點中自旋傳輸的研究。

電子非彈性散射時間是一個度量電子處在其基態時間長短的物理量。根據費米液體理論（Fermi-liquid theory）的預測，電子在絕對零度時，電子的非彈性散射時間會是無窮長。然而，多年來眾多的實驗結果顯示，當溫度低於某個溫度後，電子的非彈性散射時間會呈現一個不隨溫度改變的定值。這個奇異的現象吸引了許多理論和實驗學家的注意。有些理論學家認為不同於費米液體理論的預測，這個現象是一個新的本徵物理性質。一開始在這方面有非常多的爭議，許多研究的結論漸漸地澄清了

這個現象。經過長時間的研究，大部分的人都相信樣品中磁性雜質的存在將會導致一個不隨溫度變動的散射率，這等效於實驗上常常被觀測到的不隨溫度變動的非彈性散射時間。在此之後，大不分的人都會將觀測到奇異的非彈性散射時間歸因為近藤效應（Kondo effect）。我們也做了一些銅鍺金合金（$Cu_{93}Ge_{4}Au_{3}$）薄膜的電子非彈性散射時間研究。我們的結果顯示了三個非常特異的現象：第一、對於不規則程度不同的樣品中，所有的樣品都在１０度（１０Ｋ）跟６度（６Ｋ）之間呈現一個不隨溫度變動的非彈性散射時間，而且對於所有的樣品在這區間非彈性散射時間都是相同的。第二、當溫度低於６度（６Ｋ）時，非彈性散射時間急速的增加而且增加的速率跟樣品的不規則程度有關。對於一個不規則程度較高的樣品，非彈性散射時間增加的速率比較快。第三、在１０度（１０Ｋ）到３０毫度（３０ｍＫ）區間，外加高達１５Ｔ的磁場依舊對電阻全無影響。所有的證據顯示動態結構缺陷效應（dynamic structure defeat effect）主宰整個系統行為。我們的結果是第一個有系統分析這個效應的研究。

這幾年，因為在量子資訊上潛在的應用，量子點中電子自旋的傳輸吸引了非常多研究上的注意。我們也做了兩個垂直量子點的題目。

第一個是有關於自旋選擇法則。我們量測了銦鎵砷（$In_{0.05}Ga_{0.95}As$）垂直雙量子點的傳輸頻譜。利用大

偏壓法（large source-drain voltage），從雙電子到三電子傳輸基態跟激發態的頻譜同時可以被觀測到。在觀測到的頻譜中，從１Ｓ^{2}單重態到１Ｓ２Ｐ三重態的基態過渡在５Ｔ被觀測到。在高於５Ｔ的磁場下，可以清楚的看到黎蔓分離（Zeeman splitting），而g值（g factor）是０．３６。藉由自旋選擇法則我們可以解釋在從雙電子到三電子的傳輸中只有兩條黎蔓分離線而不是三條黎蔓分離線‧對於躍遷前後的電子自旋數大於１／２是不被允許的。因為電子在自旋雙態（doublet state）的遲逾時間（relaxation time）遠大於電子穿隧傳輸的時間，所以上自旋（spin up）跟下自旋（spin down）都可以成為傳輸的起始態。總共會有四個可能的傳輸貢獻，但只有兩個有效能量可以在傳輸頻譜上被觀測到。

第二個主題是有關於在黎蔓非吻合的量子點中的自旋傳輸。我們量測了在不同g值的雙量子點的穿隧電流（tunneling currents）。結果是完全的不同於相同g值的雙量子點的穿隧電流。特別的，因為兩個電子點間黎蔓不吻合的穿遂，人們預測兩個分裂的電流峰將會被觀測到。另外，聲子（phonon）的散射強烈地影響到傳隧的電流值。在弱的聲子散射只有上自旋電子可以共振（resonance）地穿遂，而下自旋電子則不行。除此之外，帶寬（bandwidth）共振穿遂電流峰在這個黎蔓不吻合的系統中被觀測到。

Abstract

We report two mesoscopic topics in the thesis. First one is about the low temperature dephasing time in $Cu_{93}Ge_4Au_3$ thin films and second one is about the spin transport in $In_xGa_{1-x}As$ (GaAs) vertical double quantum dots.

The electron dephasing time is a time scale that how long an electron can stay at its eigenstate. Fermi-liquid theory predicts that the lifetime of an electron at the Fermi surface at $T = 0$ is infinite. However, many experiments show that the dephasing times are always constant at low temperature. The anomalous low temperature desphasing time catches many theorists' and experimentalists' interest. Some theorists propose that the saturating low temperature dephasing time is intrinsic physics which is contrast to the Fermi-liquid theory. It makes a lot of controversy on the phenomenon. Many works were done to clarify the physics. After a lot of studies on the field, people believe that magnetic impurities would induce a constant scattering time which is equal to the observed saturating dephasing time. After that, people often refer the anomalous low temperature dephasing time to the Kondo effect. We study the low temperature dephasing time in $Cu_{93}Ge_4Au_3$ thin films. There are three distinct features. First one is that the dephasing time is a constant value between 10 K and 6 K for all of measured films with different levels of disorder. Second one is that the dephasing time increases drastically as temperature is lower than 6 K. The increasing rates depend on the levels of disorder. For a more disordered film, the increasing rate is more drastic. Third one is that the temperature dependent resistance from 10 K down to 30 mK is insensitive to the magnetic filed up to 15 T. All of the results

support that the dynamic structure defeat effect dominates the behaviors. Our experiment is the first systematic study on the dynamic structure defeat effect.

The electron spin transports in quantum dots have caught considerable increasing of interest because of potential development on quantum information. We have done two subjects on spin transport in vertical double quantum dots.

First subject is about the spin-selection rule. We measured electron transport state spectra of an $\mathrm{In}_{0.05}\mathrm{Ga}_{0.95}\mathrm{As}$ vertical double quantum dot. Both the ground and excited states of transport spectra from two electrons to three electrons are measured using a large source-drain voltage. In the obtained transition spectrum, the ground state transition from the $1S^2$ singlet state to the $1S2P$ triplet state is observed at 5 T. Zeeman splitting with a g-factor of 0.36 is clearly observed at magnetic fields higher than 5 T. The observation of two Zeeman sublevels instead of three for the triplet state is explained by the spin selection rules for the S_Z components between the two-electron and three-electron spin states. Transition with the total spin difference between the initial and final states larger than 1/2 is forbidden. Because the relaxation time between doublet states is much longer than electron tunneling time, both spin up and spin down can be the initial states from spin transitions. There are four transitions contributing to tunneling processes, but only two energy differences lead to the two Zeeman sublevels in the excitation spectra.

The second subject is related to spin transport in Zeeman mismatch double quantum dots. We measure tunneling currents in a vertical double quantum dot with different g factors for the two dots. The results are substantially different from those in a double quantum dot with a homogeneous g factor. In particular, two split peaks are expected to be observed due to the Zeeman mismatch of inter-dot tunneling. In contrast to the case of a homogeneous g factor, the coupling to phonons strongly affects the tunneling current in the system with an inhomogeneous g factor. For weak coupling strengths, only up-spin electrons can resonantly tunnel through the dots while the down-spin tunneling is spin blockaded. Besides, a bandwidth resonance tunneling peak also appears in the system with mismatched g factors.

I would like to dedicate this thesis to my loving families.

Acknowledgements

First, I would like to thank Prof. Dr. Juhn-Jong Lin who guides me into the field of low temperature mesoscopic transport and study so many interesting topics together.

Second, I would like to thank Prof. Dr. kimitoshi Kono who gives me a chance to do research in his laboratory under the *NCTU-RIKEN Joint Graduate School Program* and supports me living allowance and research cost in Japan for three years.

Third, I would like to thank Dr. Hikota Akimoto who teaches me a lot of low temperature experimental technique. I would like to thank Dr. Keiji Ono who guides me into the field of quantum dot.

I also would like to thank people who ever help me in somewhere and someway.

Last but not least, I would like to thank my families who always give me a wide freedom to do what I decide.

Contents

List of Figures

List of Tables

Chapter 1

Introduction

Low temperature mesoscopic transport is a very interesting topic in research no matter on the technique application or basic scientific study. The more we study, the more new and fantastic physics and phenomena are discovery and invented. In the thesis, I report two mesoscopic topics which I have studied in the years. The first one is concerning low temperature electron dephasing time in $Cu_{93}Ge_4Au_3$ thin films and the second one is concerning the electron spin transport in $In_xGa_{1-x}As$ (GaAs) vertical double quantum dots. I will discuss the first one topic, low temperature dephasing time, in the part 1 from chapter 2 to chapter 5 and discuss the second topic, spin transport in dotble quantum dots, in the part 2 from chapter 6 to chapter 9. Last, I would give conclusions and future works in the chapter 10.

Part1:

Low Temperature Electron Dephasing Time

Chapter 2

Introduction to Low Temperature Dephasing Time

The motion of conduction electron in solids has long been a subject of interest and fascination. In a crystalline or ordered material, where the potential is periodic, the conduction electron are well described by Bloch theory which the electron wave function are specially extended throughout the system. The electrical conduction in such a system can be described by the Boltzmann transport. The results of the theory are that at high temperatures the resistivity is dominated by phonon scattering and at low temperature the resistivity is dominated by the impurities. The Boltzmann equation predicts, in the low temperature regime, a resistivity which is given by

$$\rho(T) = \rho_e + AT^5, \tag{2.1}$$

where A is a constant, and ρ_e is the residual or impurity resistivity, which is caused by collision of electron with impurities. Since the impurities are treated as static, the residual resistivity is temperature independent. It is also well known that in the formalism of Boltamann transport theory the impurity concentrations are assumed to be extremely low. In the extremely disordered limit, the scattered electrons can be described by superpositions of Bloch waves.

In 1958, Anderson(1) pointed out that,when the randomness or disorder in the potential is sufficient high, i.e., in the strong disorder limit, the electron wave functions may be altered from the Bloch forms. He showed that the electron wave would be localized in regions where the potential is particularly suitable. Thouless(2; 3) and co-workers(4; 5) had tempted to formulate a scaling description of the localization problem. They predicted that in one dimensional system, once the residual resistance of a wire exceeded a critical value of the order of $\hbar/e^2$ ($\sim 4K\Omega$), hence the electronic states would be localized. Several experiments had been reported to check this prediction.

In 1979, Abrahams, Anderson, Licciardello, and Ramakrishnan(6) based on those arguments of Thouless and co-works(2; 3; 4), successfully constructed a scaling theory of localization. They concluded that, in the presence of any amount of impurities, there would be no extended states in two dimensional systems. They showed that the conductance would undergo a crossover from a logarithmic decrease to an exponential decrease with increasing the linear dimension of the system. In three dimensional system, the scaling theory predicted that the metal-insulator transition would be continuous.

The localization theory is a single particle description. Considering many body effects, Al'tshuler and Aronov(7; 8) pointed out that the interaction between the conduction electrons, in the presence of weak disorder, would have strong effects on the transport properties. They studied the Coulomb interactions between screened, two dimensional electrons whose motion is diffusive. They found the interactions between electrons are greatly enhanced in this case, causing a logarithmic singularity in the density of states in turn results in a non-ohmic conductivity which is similar to that predicted by localization.(9; 10) This theory is commonly referred to as electron-electron interaction theory. Such a singularity in the density of states led to very similar effects on the electronic transport properties as those predicted by the weak localization theory.

There have been a number of experimental studies in the past several years of various types of disordered conductors, which have been aimed at testing these predictions. The behavior of the resistance as a function of temperature agreed qualitatively with the theory. These experiments have also shown that the behavior is strongly dependent on the system dimensionality.(11; 12; 13; 14)

To differentiate between the weak localization effects and the electron-electron interaction effects, magnetoresistance measurements are extremely important.

Hikami, Larkin, and Nagaoka,(15) and Al'tshuler and co-worker(9; 10; 16) considered the effects of a magnetic field on the behavior of resistivity at low temperatures. These studies showed that localization and interaction respond very differently to a magnetic field. It turns out that localization effects result in an anisotropic magnetoresistance in a very low magnetic field regime. Interaction effects, on the contrary, result in an isotropic magnetoresistance, but the magnitude of this magnetoresistance is important only at significantly high magnetic fields. It was also found that the effects of spin-orbit scattering and spin-spin scattering can be very important. If the spin-orbit scattering is strong enough, it can cause an effect with a sign opposite to that of localization.(17) That is, it cause the resistance to decrease as the temperature is lowered, rather than increase. This effect is known as anti-localization. A number of very successful measurements have been performed to test these predictions.(17; 18; 19; 20; 21; 22; 23) In particular, magnetoresistance measurements have been used to infer the electron inelastic scattering time, the spin-obit scattering time, and the spin-spin scattering time, and hence the overall contribution to the zero field behavior from localization an be determined.

It is well established that one can extract the electron-phonon scattering time, electron-electron scattering time, spin-orbit scattering time, and spin-spin scattering time from magnetoresistivity measurements. There have been many experiments done in this direction to obtain these phase breaking times which have proved that this is a very reliable method. There have been many experiments using this method to obtain the phase breaking times in different dimensional systems. Bergmann does a lot of works on spin-orbit inelastic scattering time.(24; 25; 26) Lin and Giordano(27; 28) study the electron-electron scattering time in 1D and 2D in AuPd films. Their results are good agreement with theoretical predictions and widely accepted. In experimental side, Lin and Wu(29; 30; 31) and many scientists study the electron-phonon inelastic scattering time, τ_{ep}, in many different systems(32; 33; 34; 35). They point out that the $\tau_{ep} \propto T^{-p}$ where p ranges from 2 to 4. In theoretic side, Sergeev and Mitin establish a phonon-drag theory which can explain experiment results well.(36; 37; 38)

Lin and Giordano perform systematic measurements of inelastic scattering times in several AuPd films. They point out the the saturated inelastic times depend on the sheet resistance, $R_\square$, and conclude that the observed saturation inelastic scattering time cannot be explained in terms of magnetic scattering. After that, more and more experimental works observe the same behaviors. In 1997 Mohanty(39) collects many experimental results and points out that experiment always observe a constant τ_ϕ when temperature is sufficiently low. The saturation of τ_ϕ occurs in both one and two dimensional metal and semiconductor mesoscopic structures. The observation of τ_ϕ saturation immediately triggered many experimental and theoretical groups asking whether the saturation might be universal in all material systems and dimensions.

The electron dephasing time τ_ϕ is one of the most important quantities governing quantum interference phenomena. Recently, the behavior of the dephasing time near zero temperature, τ_ϕ^0 has attracted many experimental(39; 40; 41; 42; 43; 44; 45; 46; 47) and theoretical(48; 49; 50; 51; 52; 53; 54; 55; 56) attentions. One of the central themes of this renewed interest is concerned with whether τ_ϕ^0 should reach a finite or an infinite value as temperature approach 0 K. The connection of the τ_ϕ^0 behavior with fundamental condensed matter physic problems, such as the validity of the Fermi-liquid picture, has been intensively addressed. Conventionally, it is accepted that τ_ϕ^0 should reach an infinite value in the presence of only electron-electron and electron-phonon scattering.

For a long time, the saturation behavior of τ_ϕ^0 has often been ascribe to a finite spin-spin scattering time, due to the presence of a tiny amount of magnetic impurity in the sample. Such a finite scattering rate will eventually dominate over the relevant inelastic scattering in the limit of sufficiently low temperatures. The idea of magnetic scattering induced dephasing immediately became widely accepted. Hikami greatly shaped the current understanding of the effect of spin-flip scattering on the weak localization magnetoresistance. According to the description, magnetic scattering can lead to decoherence between the two time-reversed wave traversing a closed loop, resulting in a suppression of weak localization and related quantum interference effects. Generally, the spin-spin scattering time is taken to be essentially independent of temperature, compared with the relatively strongly temperature-dependent electron-phonon and electron-electron scattering times. With this Understanding, it is natural to interpret any saturated τ_ϕ^0 measured in the experiments in terms of a finite spin-spin scattering time.

The Saclay-MSU group has measured the dephasing time of quasiparticles in several noble metal narrow wires. They found that the τ_ϕ varies as $T^{-2/3}$ which is the prediction of one dimension Nyquist electron electron scattering time down to 40 mK. Once, several ppm magnetic impurities are doped into the wires, measured inelastic scattering times show a weak temperature dependent at low temperature. They concluded that a saturation of τ_ϕ occurs only in wires that contain a small amount of magnetic impurity.(57; 58)

In contrast to the conclusion reached by the Saclay-MSU group discussed above, Mohanty *et. al.*,(45; 59) have tested and argued for a non-magnetic origin for the saturation behavior of τ_ϕ^0. Mohanty *et. al.*, first study very pure Au wires (containing less than 1 ppm of magnetic impurities), finding that there is always a saturation of τ_ϕ^0. From these measurements, they find realizes that both the values of τ_ϕ^0 and the onset temperature of saturation could be tune by adjusting the sample parameters such as the wire length, resistance, and diffusion constant. To explore this idea, Webb *et. al.*, repost further measurements on several carefully fabricated Au wires, whose onset temperature of saturation is indeed push down to very low temperatures. Webb *et. al.*, argue that τ_ϕ^0 should still saturate in these wires at a temperature $\ll$ 40 mK.

To clarify the effect of magnetic scattering on τ_ϕ, Webb *et. al.*, ion implant several ppm of Fe impurities in their pure Au wires. They find that τ_ϕ decreases by more than an order of magnitude upon adding these impurities, but remains temperature dependent down to 40 mK. Therefore, they concludes that the saturation behavior of τ_ϕ^0 observed in pure Au wires can not be due to magnetic scattering. In addition, they point out that saturation behavior of τ_ϕ^0 is also often observed in semiconductor mesoscopic structures. Since such structures are thought to contain only the smallest concentration of magnetic impurities, they conclude that the widely observed saturation must be universal and can not be simply due to magnetic scattering. It should be noted that the sample properties of the Au wires studied by Webb and co-workers were essentially similar to those studied by Saclay-MSU group.

Beside of the scattering forms discussed above, dynamic structure defeat is another source of saturation of τ_ϕ^0.(60; 61; 62; 63; 64; 65; 66; 67; 68) The simplest realization of the dynamic structure defeat is that of an atom which may sit in a doublet well potential, the two wells being localized along a line directed between their centers which are separated by a displacement. In the absence of coupling to a bath of excitations, the lowest two states of the atom are, approximately, the positional eigenstates associated with harmonic oscillations within either well. The next level usually has energy above the barrier between the well minima and therefore is not localized to either well. Atoms may move between the two positions on quantum-mechanic tunneling. In the process, the atom directly tunnels through the potential barrier between the wells. Because of the thermal activated transitions, this process must dominate at sufficiently low temperatures.

The original motivation for studying such a model was the observation of logarithmic anomalies in the resistivity of metallic glasses.(11; 69) Most of the works also only focused on the resistivity, specific heat, and susceptibilty. Only a few works on electron dephasing time are reported. Lin and co-workers study the annealing effects in a lot of three-dimensional polycrystalline disordered metal films.(70) They perform systematic measurements of τ_φ on several series of sputtered and subsequently annealed AuPd and Sb thick films. Such controlled annealing measurements are crucial for testing theoretical models of dephasing that invoke the role of magnetic scattering and dynamical defeats.

In the first part of the thesis, I will discuss our experimental observation of temperature dependence of dephasing time in $Cu_{93}Ge_4Au_3$ films. Our results indicate that a very short electron dephasing time possessing very weak temperature dependence around 6 K, followed by an upturn with further decrease in temperature below 4 K. The low temperature upturn is progressively more pronounced in more disordered samples. Resistance is logarithmic increase with decreasing temperature in wide temperature range and it is insensitive to magnetic field up to 15 T. In the thesis, we will discuss the temperature dependent resistance at different magnetic field and temperature dependent dephasing time in series of samples with different levels of disorder on weak localization effect, Kondo effect, and two-level system effect. Synthesizing all discussion, we can rule out all others inelastic scattering and make sure out observed low temperature dephasing time is from two-level system scattering. This is the first systematic work discussing the disorder dependence with low temperature temperature dephasing times of dynamic structure defeat effect.

Chapter 3

Theory and Background

3.1 Weak Localization

The usual Boltzmann transport theory is based on that, between two collision events, the electrons move along classical trajectories. Every scattering and two trajectories are treated as independent. For this classical transport theory to be valid, the scattering centers much be independent of each other. Therefore, the theory is valid only when the elastic mean free path, l_e is much larger than the electron Fermi wavelength λ_F. On the other hand, if the condition is no longer satisfied and $l_e \sim \lambda_F$ the electron eigenstates might become localized. This phenomenon was first proposed by Anderson.(1) After this proposition, everyone believes that the electron states are localized states in strong disordered systems and electron states are extended states in good latticed systems. Concerning a system that the condition, $l_e > \lambda_F$ is still holds, but the scattering can no longer be treated as independent. The electron wavefunctions interference can not be neglected any more and this interference causes the electron states to be weakly localized.

The electron motion in weak disordered systems is diffusive rather than ballistic or hopping. Here we assume that the time of all inelastic scattering are much longer than the elastic collision time and the electron wavelength is much short than the mean free path. Under these assumptions, electrons can be treated wave packets. As shown in Fig. 3.1, an electron diffuses from point A to point B along different paths 1, 2, 3. The form of the individual path reflects the nature of diffusive motion of electrons in a system with impurities. According to general principles of quantum mechanics, the total probability, P, of reaching point B from point A is

$$P = \left| \sum_i A_i \right|^2 = \sum_i |A_i|^2 + \sum_{ij} A_i A_j^*, \tag{3.1}$$

where A$_i$ is the probability amplitude of path i. In the first part from right hand side of Eq. 3.1, the first term is the sum of the probabilities corresponding to separate trajectories and is also the probabilities corresponding to classical diffusion. The second term is the interference terms that different wave pockets interfere along the trajectories. In the classical transport, the interfering term is not important and contributes nothing to the conductivity.

However, there is an exception, when point A and point B coincide, the electrons have two different ways to propagate around the loop, either clockwise or counterclockwise. As shown in Fig. 3.2 one partial wave goes in the direction of $0 \rightarrow 1 \rightarrow 2 \rightarrow 3 \rightarrow 4 \rightarrow 5 \rightarrow 0$, and the other partial wave goes in the opposite direction $0 \rightarrow 5 \rightarrow 4 \rightarrow 3 \rightarrow 2 \rightarrow 1 \rightarrow 0$. If all the propagating processes along the loop are elastic scattering, the phases of two partial waves are in phase at point O, and the interference term is full constructed. As a result, the probability of finding the electron at point O is enhanced, twice higher than the case of out of phase. In other words, quantum particles are less mobile in a random potential than that would be expected from Boltzmann transport theory. The enhanced "localized" probability contributes a decrease in conductivity or, equivalently an increase in resistance. This is the well known weak localization.

Instead of calculating the quantum corrections to the conductivity following diagrammatic techniques and the Kubo formula, we estimate the corrections by probability arguments. We consider an electron diffuses in a random potential and describe its motion using diffusion equation. At time t, the probability of an electron staying at the position r is

$$P(r,t) = \frac{1}{(4\pi Dt)^{d/2}} e^{-r^2/4dt}, \tag{3.2}$$

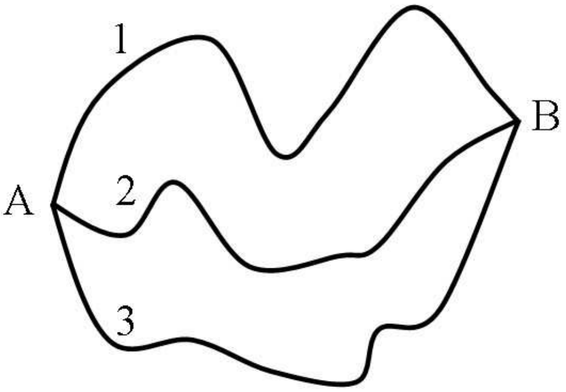

Figure 3.1: A conduction electron diffuses from point A to point B along various paths.

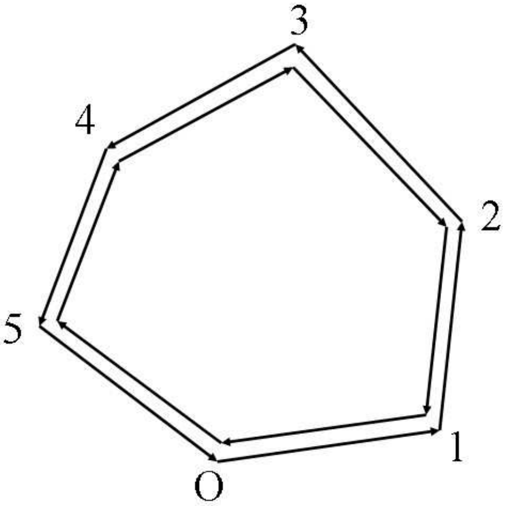

Figure 3.2: Electron diffuses in opposite directions of a loop and forms a construction at point O.

where D is the diffusion constant and d is the system dimensionality. The probability of electron localized in origin point is

$$P(0,t) = \frac{1}{(4\pi Dt)^{d/2}}. \tag{3.3}$$

Considering a condition that a electron diffuses in a path, as shown in Fig. 3.3. The electron travels a length $v_F dt$ during a time interval dt and cross section is $(\hbar/mv_F)^{d-1}$ in d dimensions space. The corrections to the conductivity, $\Delta\sigma/\sigma$, are proportional to the ratio of the back-scattering volume to the total diffusion volume. so the magnitudes of the quantum corrections to the conductivity are given by

$$\frac{\Delta\sigma}{\sigma} \sim -\int_{\tau_e}^{\tau_\phi} \frac{v_F \times (\frac{\hbar}{mv_F})^{d-1}}{(Dt)^{d/2}} dt = -\int_{\tau_e}^{\tau_\phi} \frac{\lambda_F^{d-1} v_F}{(Dt)^{d/2}} dt, \tag{3.4}$$

where τ_e is the elastic scattering time and τ_ϕ is the phase-relaxation time. The τ_ϕ means that how long the electron stays at its eigenstate and keeps the electron wave phase coherence. The negative sign in Eq. 3.4 indicates that the conductivity is reduced from the Boltzmann conductivity. It comes from the interference of two partial wave as shown in the interference term of the Eq. 3.1. Integrating Eq. 3.4, one can get that

$$\begin{aligned} \Delta\sigma &\sim -\frac{e^2}{\hbar} L_\phi, \quad \text{for} \quad d = 1, \\ \Delta\sigma &\sim -\frac{e^2}{\hbar} l_n(\frac{L_\phi}{l_e}), \quad \text{for} \quad d = 2, \\ \Delta\sigma &\sim -\frac{e^2}{\hbar}\frac{1}{L_\phi}, \quad \text{for} \quad d = 3, \end{aligned} \tag{3.5}$$

where L_ϕ is the phase-coherence length which is defined by $L_\phi = (D\tau_\phi)^{1/2}$.

3.2 Phase Breaking Mechanics

From the above discussion, it is clear that the quantum corrections to conductivity are very sensitive to the phase of the electron wave. There are several kinds of electron scattering can destroy the phase coherence of the wavefunction. Next, we will discuss them respectively.

3.2.1 Magnetic Field

It is well known that in quantum mechanics the hamiltonian for a charged particle in a magnetic field is obtained by replacing the momentum operator $\vec{p}$ by $\vec{p} - e\vec{A}$, where $\vec{A}$ is the vector potential, and hence that the basic effect of a magnetic field is to introduce an extra factor

$$\Delta\Phi = -\frac{e}{\hbar}\oint \vec{A}(\vec{r},t)\cdot d\vec{r}, \tag{3.6}$$

to phase of the corresponding wave function.

If a magnetic field is applied perpendicular to the closed loop, both of the partial waves will acquire an extra phase of the same magnitude, but with opposite sign because the directions of the integration path are opposite. Therefore the coherence interference of the electron waves is diminished and the corrections to conductivity is reduced. Assuming the $\vec{A}$ is time independent, the relative change of the phase of the two partial waves is two times larger than that in Eq. 3.6

$$\Delta\Phi = -\frac{2e}{\hbar}\oint \vec{A}\cdot d\vec{r} = \frac{2e}{\hbar}\Phi, \tag{3.7}$$

where the integration is along the closed loop traveled by the two partial waves and the Φ is the magnetic flux penetrating the closed loop area. If the phase difference $\Delta\Phi \sim \pi$, the weak localization effect is entirely suppressed

$$\pi = \frac{2e}{\hbar}H \times (\text{closed loop area}). \tag{3.8}$$

For a diffusive electron, the closed loop area is order of $D\tau_i$ where D is the diffusion constant and τ_i is inelastic scattering time. We get that localization effect will be entirely suppressed at a magnetic field of order

$$H_c \approx \frac{\hbar}{eD\tau_i}, \tag{3.9}$$

which is of order of 1kG in real cases. Here H_c is referred to as the "critical magnetic field." It is important to note that the destroy phase coherence leads to a negative magnetoresistance with increasing magnetic field.

3.2.2 Spin-Orbit Scattering

A moving charge in a lattice will feel an effective magnetic field

$$\vec{B}_{eff} = -\frac{\vec{v}}{c} \times \vec{E}, \tag{3.10}$$

where $\vec{v}$ is velocity of the moving charge, c is the speed of light, and $\vec{E}$ is the electric field comes from nucleus electric charges. A simple picture explaining the spin-orbit scattering effects on weak localization is introduced by Bergmann.(17) For each spin-orbit scattering, a electron spin rotates a small angle. Because the rotation operator does not commute, the two final spin states of the two partial waves are not the same. Therefore, the constructive interference of the two partial wave is destroyed. To consider two partial waves in spin-state $\vec{S}$, we present spin operator $\vec{R}$. As shown in Fig. 3.4, the operator rotates one of the initial spin state $\vec{S}$ to final spin state, $\vec{S'}$. $\vec{S'} = \vec{R} \cdot \vec{S}$. The operator is described by Eulerian angle. In the opposite direction, the final spin state is $\vec{S''} = \vec{R}^{-1} \cdot \vec{S}$. The spin states of the two partial waves are different. The scalar product is $<\vec{S'}|\vec{S''}>=<\vec{S}|R^2|\vec{S}>$, so the two partial waves are coherence only when $R^2 = 1$. The coherence condition corresponds to the spin-orbit scattering time τ_{so} being very large as compared with the inelastic scattering time τ_i. If the condition is not satisfied, then the spin-orbit scattering will suppress the coherent back-scattering and lead to increase of the conductivity.

In the strong spin-orbit coupling limit, Bergmann has shown that phase difference between two partial waves is most equal to 2π. However, this is a destructive interference because the spin electron has a rotational periodicity of 4π. This phenomenon of decreased resistivity in the presence of strong spin-orbit scattering is called weak anti-localization.

Stephan and Bergmann(71) have suggested that the spin-orbit scattering cross section should also depend on the total orbital angular momentum L and total spin angular momentum S. They predicted that the spin-orbit scattering cross section is

$$\sigma_{so} = \frac{4\pi}{E_F} \sum_{l} \frac{l(l+1)}{2l+1} sin^2[\delta^{so}_{l+1/2,l}(E_F) - \delta^{so}_{l-1/2,l}(E_F)], \tag{3.11}$$

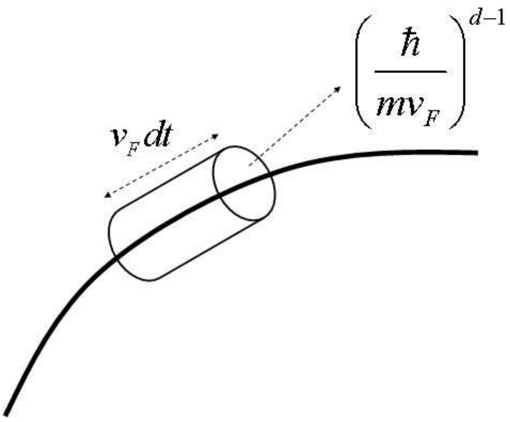

Figure 3.3: A electron diffuse in a d-dimensions space.

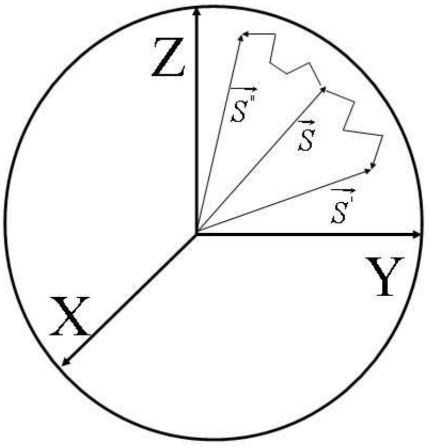

Figure 3.4: Schema of spin-orbit interaction. The initial spin state is *S*. After several scattering of spin-orbit coupling, two final states of two partial waves are *S'* and *S"*.

where E_F is the Fermi energy of the host, δ^{so} is the phase shift contributed by spin-orbit scattering which depends both on the total angular momentum, $j = l \pm 1/2$ and angular momentum, l.

3.2.3 Spin-Spin Scattering

The presence of localized spins or magnetic impurities introduces a pertubation part in the Heisenberg coupling

$$H_s = J\vec{S_1} \cdot \vec{S_2}, \tag{3.12}$$

where J is an exchange constant and $\vec{S_1}$ and $\vec{S_2}$ mean the spins of electron and ion spins respectively. This perturbation destroys the time-reversal symmetry of the hamiltonian. The localized moment breaks the coherence of the two partial waves. It is noticeable that the influence on the weak localization is similar to that of the inelastic scattering on the weak localization. The spin-spin scattering time can be expressed as

$$\frac{1}{\tau_s} \sim 2\pi N(E_F) n_i J^2 S^2, \tag{3.13}$$

where $N(E_F)$ is the density of state at the Fermi energy and n_i is the density of the magnetic impurities.(72)

3.3 Correction to Conductivity

It is well known that both localization and electron-electron interaction play fundamental roles in disordered systems. It is also clear that, especial since the work of Thouless, that the behavior is strongly dependent on the dimensionality. The first theoretical work predicted that the behavior would depend on the resistance (sheet resistance in two dimensions) and on the electron inelastic scattering time. Later works have shown that other types of scattering, namely the spin-orbit scattering and spin-spin scattering (magnetic impurity scattering), are also important. Moreover, the theory makes explicit predictions for the behavior of the resistance as a function of both temperature and magnetic field. Next, I would like to discuss the corrections of several interactions to conductivity.

3.3.1 Localization: Two Dimensions

In two dimensions, it is convenient to consider the resistance per square, $R_\square$ (also known as the sheet resistance), which is just the resistivity divided by the thickness d, $R_\square = \rho/d$. For a system in which spin-orbit scattering and spin-spin scattering are negligible and in the absence of a magnetic field, localization makes a contribution to the sheet resistance which is of the form

$$\frac{\Delta R_\square(T)}{R_\square(T_0)} = -\frac{\alpha e^2 p}{2\pi^2\hbar} R_\square(T_0) ln(\frac{T}{T_0}), \tag{3.14}$$

where α is a constant which depends only on general symmetry and parameter p is determined by the temperature dependence of the inelastic scattering time. In generally, the αP is an integer of order unity. T_0 is an arbitrary reference temperature which is about 10 K in our experiments. In general case, when a magnetic field is present and other types of scattering cannot be neglected, it is considerably more complicated. It is found at a fixed temperature that

$$\begin{aligned} \frac{\Delta R_\square(H)}{R_\square^2(0)} &= -\frac{e^2}{2\pi^2\hbar}\{\Psi(\frac{1}{2}+\frac{H_1}{H}) - \Psi(\frac{1}{2}+\frac{H_2}{H})\} \\ &+\frac{e^2}{4\pi^2\hbar}\{\Psi(\frac{1}{2}+\frac{H_3}{H}) - \Psi(\frac{1}{2}+\frac{H_2}{H})\} \\ &-\frac{e^2}{2\pi^2\hbar}\{ln(\frac{H_1}{H}) - \frac{3}{2}ln(\frac{H_2}{H}) + \frac{1}{2}ln(\frac{H_3}{H})\}. \end{aligned} \tag{3.15}$$

where Ψ is the digamma function and the "fields" H_1, H_2, and H_3 are described by

$$\begin{aligned} H_1 &= H_e + H_{so} + H_s, \\ H_2 &= H_i + \frac{4}{3}H_{so} + \frac{2}{3}H_s, \\ H_3 &= H_i + 2H_s, \end{aligned} \tag{3.16}$$

H_e, H_{so}, H_s, and H_i mean elastic, spin-orbit, spin-spin, and inelastic scattering "magnetic field" respectively. Here the magnetic field, H, is assumed to be perpendicular to the plane of the film. The respective "magnetic field" connects to the corresponding scattering time by the formula

$$H_x = \frac{\hbar}{4eD\tau_x}. \tag{3.17}$$

Note that the H_e is generally much larger than any of the other fields in the problem.

It is important to keep in mind several points concerning these predictions. First, a film will behavior two dimensionally only when its thickness is less than the phase breaking length, $L_\varphi = (D\tau_\varphi)^{\frac{1}{2}}$, where the phase-breaking time, τ_φ, is the time scale over which phase coherence is maintained. This condition on the film thickness provides a consistency check on the analysis. Also, the conventional or classical magnetoresistance which is of order

$$\frac{\Delta R(H)}{R(0)} \approx (\omega_c\tau_e)^2, \tag{3.18}$$

Where ω_c is the electronic cyclotron frequency, is generally much smaller than that predicted in Eq. 3.15 in the low magnetic field regime of interest, so it can be ignored.

Finally, spin-orbit scattering plays a very important role, since it determines the sign of both the magnetoresistance and the change of the resistance in zero magnetic field. The magnetoresistance is negative and the zero field resistance change is positive for weak spin-orbit scattering. In the opposite case, the correction to the resistance changes sign and is magnitude is reduced by a factor two. The later case is often referred to anti-localization.

3.3.2 Electron-Electron Interactions: Two Dimensions

It is well known that the behavior of the resistivity resulting from electron-electron interactions, in zero magnetic field, are very similar in form to that due to localization. The theory of electron-electron interactions has been studied. In two dimensions, they found that the correction to conductivity, in the absence of a magnetic field, as a function of temperature is

$$\frac{\Delta R_\square(T)}{R_\square(T_0)} = -\frac{e^2}{2\pi_2\hbar}(1-\frac{3}{4}F)R_\square ln(\frac{T}{T_0}), \tag{3.19}$$

where F is a screening factor. In a well screened system, F approaches unity and in the opposite limit, F approaches zero.

In the presence of a magnetic field, the interaction theory predicts an positive, isotropic magnetoresistance. However, since this prediction is concerned with the splitting of the electron spins energy bands, it is not noticeable at low magnetic fields. Therefore, this effect will not be considered in this thesis.

3.3.3 Kondo Effect

Since first experimental observation of increasing resistivity with decreasing temperature in gold, the resistance minimum was a long standing theoretical puzzle. The later observation, that the minimum depended on the impurity concentration, indicated it as being an impurity phenomenon. Kodon observed a correlation between the existence of Curie-Weiss term in the impurity susceptibility (a local moment) and the occurrence of the resistance minimum. Kondo calculated the conductivity to higher terms of $s-d$ model and his results can well explain the experimental observation.

In some cases, the impurity atom may retain its magnetic moment in a metal. An isolated atom generally has a spin and orbital angular momentum according to Hund's rule. For a transition metal ion, one that displays evidence of local moment behavior as an impurity in a metal, it might be reasonable to describe it as in an insulator and then consider the effects of the ion magnetic moment on the conduction electrons. Zener proposed a model of ferromagnetic transition metals in which it is assumed that the d electrons are localized at the atomic sites and the s electron are itinerant over the entire crystal. He considered an exchange interaction between the two kinds of electrons,to which he attributed the ferromagnetism of the $3d$ metals. For a single impurity in a metal the interaction takes the form,

$$H_{sd} = \sum_{k,k'} J_{k,k'}(S^+ c^\dagger_{k,\downarrow} c_{k',\uparrow} + S^- c^\dagger_{k,\uparrow} c_{k',\downarrow} + S_z(c^\dagger_{k,\uparrow} c_{k',\uparrow} - c^\dagger_{k,\downarrow} c_{k',\downarrow})) \tag{3.20}$$

where S_z and $S^{\pm}(= S_x \pm iS_y)$ are the spin operator for a state of spin S. It represents a Heisenberg exchange interaction between a local moment and the conduction electrons with a coupling constant $J_{k,k'}$. $c^\dagger_{k,\sigma}$ and $c_{k',\sigma}$ are creation and annihilation operators for the conduction electrons. There are terms in this interaction in which the spin of the conduction electron is flipped on scattering with the impurity.

To calculate the resistivity to third order in J, the form becomes

$$< k', \sigma' | T(\epsilon) | k, \sigma > = < k', \sigma' | H_{sd} G(\epsilon) H_{sd} | k, \sigma > \tag{3.21}$$

where T is a matrix of that between states of Slater determinants in which a conduction electron is scattering from a state (k, σ) to a state (k', σ). $G(\epsilon)$ is green function. There are many contributions to this matrix element, the most important terms are the ones in which the spins of the conduction and localized electron are flipped. The modification required in the calculation of the T matrix in the many body case can be stated quite simply; we have to replace the occupation numbers for electrons (holes) in the intermediate k states by Fermi factor $f(\epsilon_k)$ $(1 - f(\epsilon_k))$.

There are four possible processes: from $< k, \uparrow |$ to $|k', \uparrow>$, from $< k, \uparrow |$ to $|k', \downarrow>$, from $< k, \downarrow |$ to $|k', \uparrow>$, and from $< k, \downarrow |$ to $|k', \downarrow>$. First, we consider the first scattering process, from $< k, \uparrow |$ to $|k', \uparrow>$. The contribution is

$$\frac{J^2}{N_s^2} \sum_{k_1, k_1', k_2, k_2'} < k', \uparrow | S^- c^\dagger_{k_1,\uparrow} c_{k_1',\downarrow} (\epsilon + is - H_0)^{-1} S^+ c^\dagger_{k_2,\downarrow} c_{k_2',\uparrow} | k, \uparrow > \tag{3.22}$$

The form means that the $(k, \uparrow)$ conduction electron scatters with spin flip in to an unoccupied hole state $(k_2, \downarrow)$. The $(k_2, \downarrow)$ electron then scatters into the final $(k', \uparrow)$ state. Intermediate k lines running from left to right carry a hole factor $1 - f(\epsilon_k)$, the probability that they are initially unoccupied, and intermediate lines running from right to left carry a factor $f(\epsilon_k)$. This is non-vanishing if $k_1 = k', k_1' = k_2, k_2' = k$ and gives

$$\frac{J^2}{N_s^2} \sum_{k_2} S^- S^+ \frac{(1 - f(\epsilon_{k_2}))}{\epsilon + is - \epsilon(k_2)}. \tag{3.23}$$

The second possible contribution to $< k, \uparrow |$ to $|k', \uparrow>$ is

$$\frac{J^2}{N_s^2}\sum_{k_1,k_1',k_2,k_2'} < k',\uparrow|S^- c^\dagger_{k_2,\uparrow}c_{k_2',\downarrow}(\epsilon+is-H_0)^{-1}S^+c^\dagger_{k_1,\downarrow}c_{k_1',\uparrow}|k,\uparrow> \tag{3.24}$$

which contributes if $k_2' = k', k_2 = k_1', k_2 = k$ giving

$$\frac{J^2}{N_s^2}\sum_{k_2} S^- S^+ \frac{f(\epsilon_{k_2})}{\epsilon+is-\epsilon(k_2)}. \tag{3.25}$$

In the case an electron in an occupied state $(k_2,\downarrow)$ is scattered with a spin flip into the state $(k',\uparrow)$, and the remaining hole $(k_2,\downarrow)$ is annihilated by the initial $(k,\uparrow)$ with another spin flip, leaving the final state $(k',\uparrow)$. Collecting the first order and the second order terms together, we get

$$< k',\uparrow|T(\epsilon)|k,\uparrow>= S_z\frac{J}{N_s}(1-2Jg(\epsilon)), \tag{3.26}$$

where

$$g(\epsilon) = \frac{1}{N_s}\sum_k \frac{f(\epsilon_k)}{\epsilon_k-\epsilon-is}. \tag{3.27}$$

Figure 3.5 shows the carton of the four scattering processes from $(k,\uparrow)$ to $(k',\uparrow)$.

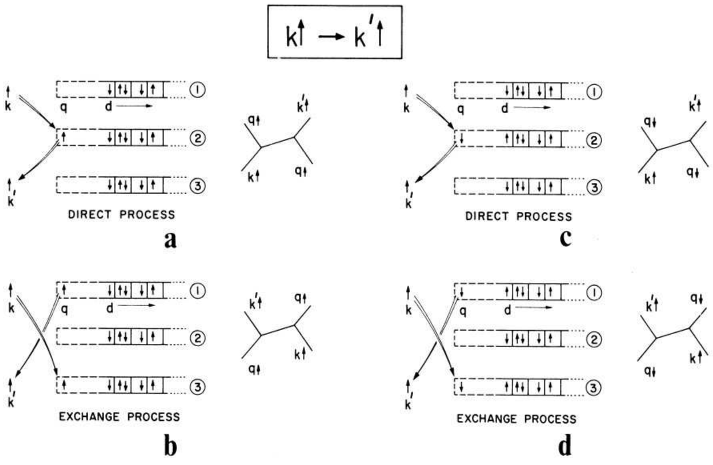

Figure 3.5: A schema of interaction between s electron and d electron. The s electron scatters from the $(k,\uparrow)$ to $(k',\uparrow)$.

Similar terms arise in calculating $< k', \downarrow |T(\epsilon)|k, \downarrow>$, $< k', \uparrow |T(\epsilon)|k, \downarrow>$, and $< k', \downarrow |T(\epsilon)|k, \uparrow>$. Connecting all these terms together, calculating the scattering time and integrating all energy we can get the result

$$R(T) \propto ln(k_B T). \tag{3.28}$$

3.3.4 Two-Level Systems

Most crystalline materials, even after annealing, contain grain boundaries, dislocations, vacancies, interstitial, substitutional impurities. These defects not only break translational symmetry thereby leading to momentum relaxation, but they also behave as dynamical impurities. The role of these dynamical impurities may be even more important in amorphous materials, where the structure is inherently disordered.

The micro-structure of these dynamical impurities is still unclear: Among others, dislocation kinks, dangling bonds and interstitial have been suggested as possible candidates for them. However, it is usual and convenient to describe them in terms of a very simple two-level system (TLS) model, where the dynamical impurity is simply some particles in an effective double well potential as shown in Fig. 3.6. At high temperatures the particle moves thermally from one side to the other, which processes are, however, suppressed at low temperature, where tunneling becomes dominant.(73; 74)

The two lowest states being well separated from the higher excited states, at low temperature it is enough to restrict out considerations to them. These two state Φ_L and Φ_R localized at left and right minima of the potential well. The effective Hamiltonian of the TLS can be expressed as

$$H_{TLS} = \frac{1}{2}\Delta_x(d_R^\dagger d_L + d_L^\dagger d_R) + \frac{1}{2}\Delta_z(d_R^\dagger d_L - d_L^\dagger d_R), \tag{3.29}$$

where the creation operator $d_{R,L}^\dagger$ are associated to the states $\Phi_{R,L}$. Δ_x is the tunneling amplitude of symmetric well and Δ_z is the tunneling amplitude of asymmetric well. The splitting of the states of the TLS is given by $\Delta = (\Delta_x^2 + \Delta_z^2)^{1/2}$.

The interaction Hamiltonian coupling the TLS and conduction electron can take the form

$$H_{TLS-e} = H^z + H^x, \tag{3.30}$$

where

$$H^z = V_z \sum_{\sigma=\uparrow,\downarrow} (d_+^\dagger d_+ - d_-^\dagger d_-)(\Phi^\dagger_{\sigma,+}\Phi_{\sigma,+} - \Phi^\dagger_{\sigma,-}\Phi_{\sigma,-}) = V_z \tau^z (\Phi^\dagger_\uparrow T^z \Phi_\uparrow + \Phi^\dagger_\downarrow T^z \Phi_\downarrow), \tag{3.31}$$

where $\tau^z = d_+^\dagger d_+ - d_-^\dagger d_-$, and T^z denotes Pauli matrices in the spinor indices. The electron operators $\Phi_{\uparrow,\downarrow,L,R}$ are defined as $\Phi_{\uparrow,\downarrow,L,R} = \int d^3k e^{ikr_{L,R}} c_{k,\uparrow,\downarrow}/(2\pi)^3$, with $c_{k,\uparrow,\downarrow}$ the annihilation operator of a conduction electron with momentum k and spins. Similarly

$$H^x = V_x \tau^x (\Phi^\dagger_\uparrow T^x \Phi_\uparrow + \Phi^\dagger_\downarrow T^x \Phi_\downarrow), \tag{3.32}$$

H^z is called screening term and describes the Ohmic dissipative tunneling system. H^x is called assisted tunneling interaction term and describes the simultaneous tunneling of the TLS and scattering of the conduction electrons. The physical origin of later interaction term, tending to *delocalize* the TLS, is very simple: Conduction electron density fluctuations change the barrier height and thus the tunneling amplitude of the TLS. Although its amplitude is rather small, this term is marginally relevant and it is responsible for the two-channel Kondo effect.(48; 53; 56)

The electrical resistivity measures the electronic scattering rate off the TLS. This subject has been first discussed by Cochrane *et. al.*,(75) who introduced an ill-defined model with two sets of conduction electrons heuristically provided. The first calculation was performed by Kondo(76; 77) up to fourth order introducing the assisted tunneling. The resistivity behavior expected at different temperatures depends on the ratio of Δ_0/T_K, and this is illustrated in Fig. 2-7. In the top curve of the Fig. 2-7, $T_K < \Delta_0$ so that the Kondo correlated state is not developed and it goes to the Fermi-liquid state. In the center and bottom

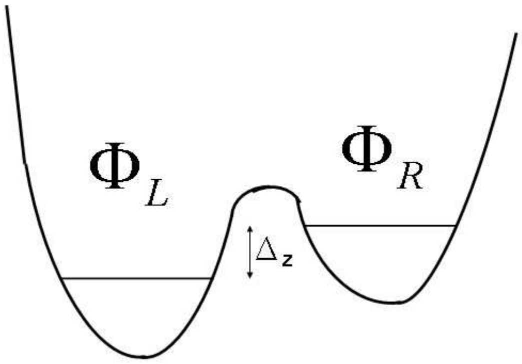

Figure 3.6: A schema of two-level system.

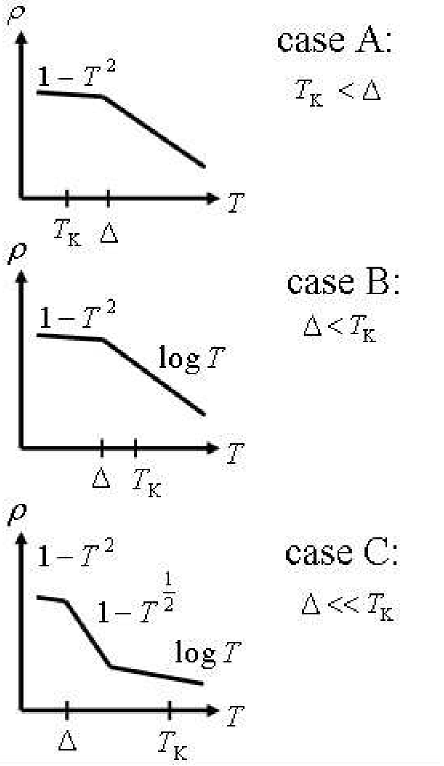

Figure 3.7: Temperature dependence of two-level system in three different cases.

curves of Fig. 2-7 we see the Fermi-liquid behavior developing eventually below T_K, but with a non-Fermi-liquid region possible provided that $\Delta_0 \ll T_K$.

At high temperatures, summation of the logarithmic divergent terms gives the correct logarithmic rise in $\rho(T)$. At low temperature for zero splitting of the levels, the non-Fermi-liquid excitation spectrum produces an anomalous saturation of the resistivity. According to conformal field theory and NCA, $\delta\rho(T) \approx \Delta\rho(0)(1 - aT^{1/2})$ in the weak-coupling limit, where a is a pure number that depends on the presence of ordinary potential scattering at the impurity site.

Chapter 4

Experimental and Technical Considerations

4.1 Introduction

In the measurement of the electron dephasing time at low temperature, we take several experimental techniques and considerations. We divide them into three parts and discuss them respectively. First part is techniques of preparing samples. Second part is low temperature measurement and last part is measuring circuit noise.

4.2 Sample Preparation

4.2.1 Substrate Cleaning

In our experiments, we use corning glass (number: 7059) as substrates. The width is 10 mm square and thickness is 0.3 mm. Before depositing films onto the substrates, we should clean the glass to avoid the unanticipated impurities on the surface. The cleaning processes are as follows. The substrates are cleaned in turn in trichloroethylene (TCE), acetone (ACE), and alcohol solvent for five minutes in an ultrasonic cleaner, and then the substrates are blown-dry with N_2 gas. Once finish the cleaning, a mask will be used to pattern the shape of films. In this series of experiments, we used two kinds of masks, metal mask and photolithography.

4.2.1.1 Metal Mask

The width and the length of the films are 0.4 mm and 5.7 mm, respectively. The film thickness are $195\mathring{A} \pm 5\mathring{A}$ or $147\mathring{A} \pm 3\mathring{A}$. Figure 4.1 shows the processes of the deposition using metal mask. All of the cartons are at front view.

Step A: Preparing a clean glass.

Step B: The metal mask is plastered on the glass using a thin coat of Apiezon 'N' vacuum grease.

Step C: Depositing the wanted material and thickness onto the mask and glass. The deposited thickness should be thinner than the mask to avoid the connecting between the films on glass and on the mask.

Step D: Remove the metal mask carefully. The patterned films are deposited on the substrate.

4.2.1.2 Photolithography

Because of the difficulty of manufacture of metal mask, the narrowest width which one can achieve is about 0.1 mm by using metal mask. When one needs narrower films, the photolithography technique can help us achieve it. The limit of the width of photolithography technique depends on wavelength of light. Typically, the narrowest width is about several μm. Figure 4.2 shows the processes of the photolithography technique. There are five steps to achieve it.

Step A: Coating a photoresist, a liquid polymeric material, onto the substrates. The coating process is performed by spinning the substrates at speeds several thousand rpm. Photoresist is deposited onto the substrate surface during the dynamic movement to ensure coating over the entire substrate surface. The coating thickness depends on the photoresist and spinning speeds.

Step B: Once the substrate has been coated with photoresist, putting the photo mask on the substrate and exposing the substrate on an exposure light. By shining light through the photo mask and onto the substrate, individual areas of the photoresist are selectively exposed to light. This exposure causes a chemical change in the photo resist.

Step C: Once exposed, the substrate is then immersed in a developer solution. Developer solution are typically aqueous and will dissolve away areas of the pho-

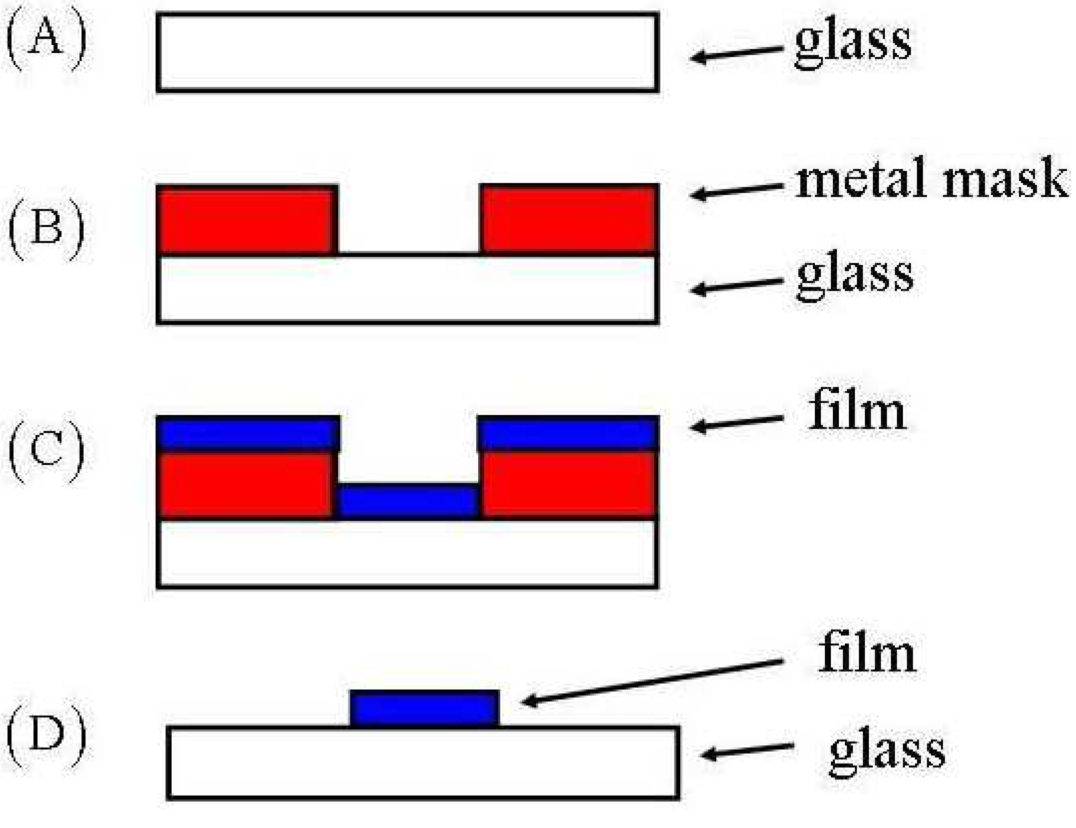

Figure 4.1: Processes of deposition by using metal mask.

toresist that were exposed to light. Therefore, after successful development, the photoresist is patterned with the wanted shape.

Step D: Depositing the wanted material and thickness onto the mask and glass. The deposited thickness should be thinner than the mask to avoid the connecting between the films on glass and on the mask.

Step E: Remove the photoresist by acetone. The patterned films are deposited on the substrate.

4.2.2 Sputtering

All of our thin films are fabricated by sputtering deposition. Our source target is the $\mathrm{Cu_{93}Ge_4Au_3}$ (atomic rate). Before sputtering, we pump the chamber vacuum to high vacuum. Once the vacuum reaches the order of 10^{-6} mbar, we inject 7 sccm argon gas into the chamber and the pressure increases to order of 1×10^{-3} mbar. Because our target is a good conductor, we chose a DC voltage source. The sputtering power ranges from 10 W to 110 W and it affects levels of the randomness (disorder) of the samples. The room temperature resistivity of our films range from 15 $\mu\Omega cm$ to 95 $\mu\Omega cm$.

Here we would discuss a little bit the operating principles of sputtering. Sputtering is a technique used to deposit thin films of a material onto a substrate. By first creating a gaseous plasma and then accelerating the ions from this plasma into a source target, the source material is eroded by the arriving ions via energy transfer and is ejected in the form of neutral particles. As these neutral particles are ejected they will travel in a straight line unless they come into contact with other particles or a nearby surface. If a substrate is placed in the path of these ejected particles it will be coated by a thin film of the source material.

The ”diode sputtering” example given above has proven to be a useful technique in the deposition of thin films when the cathode is covered with sputtering target. Diode sputtering however has two major problems. First one is the deposition rate is slow and second one is the electron bombardment of the substrate is extensive and can cause overheating and structural damage.

The development of magnetron sputtering deals with both of these issues simultaneously. Figure 4.3 shows the schematic of the magnetron sputtering. By

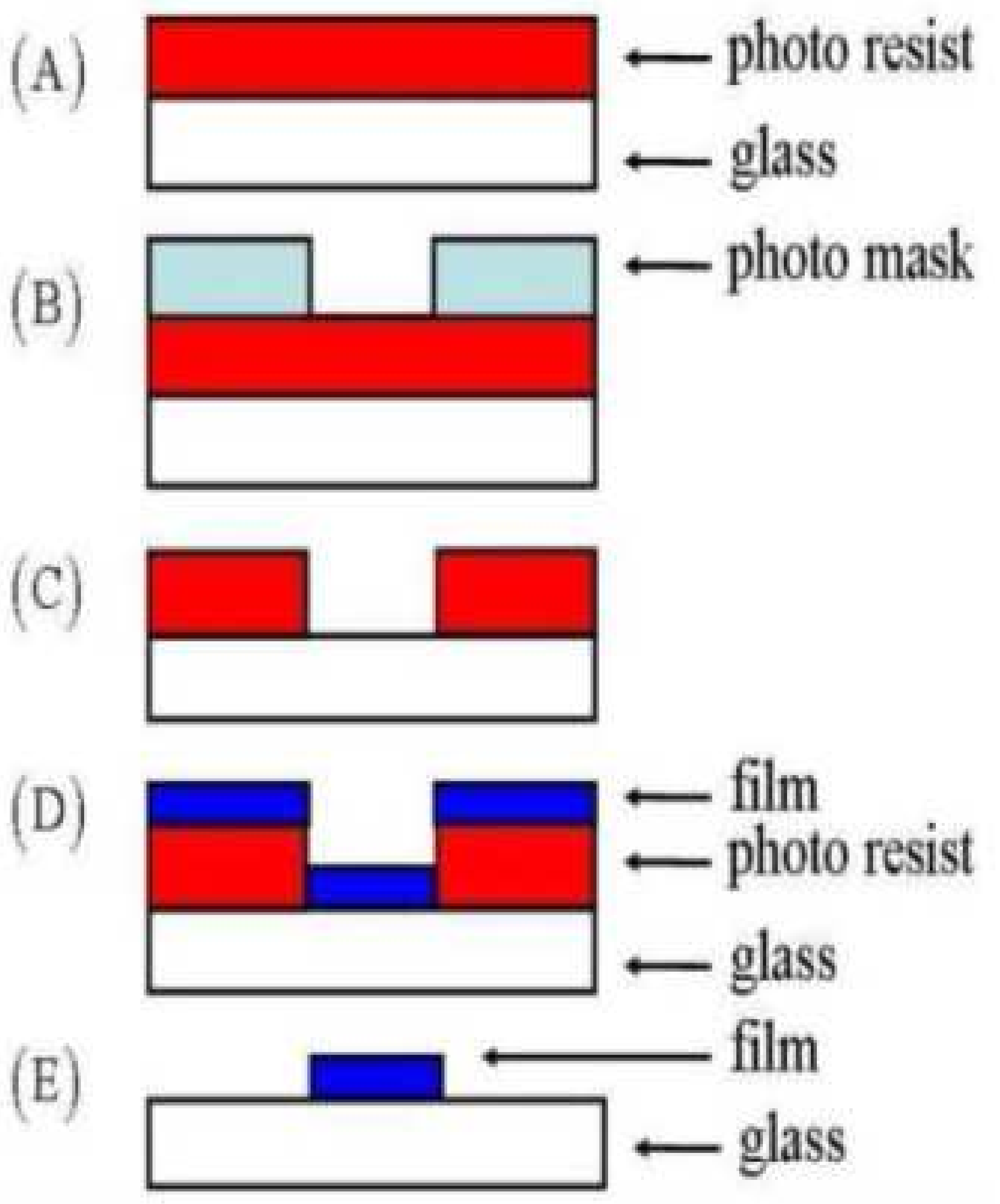

Figure 4.2: Processes of deposition by using photolithography.

using magnets behind the cathode to trap the free electrons in a magnetic field directly above the target surface, these electrons are not free to bombard the substrate to the same extent as with diode sputtering. At the same time the extensive, circuitous path carved by these same electrons when trapped in the magnetic field, enhances their probability of ionizing a neutral gas molecule by several orders of magnitude. This increase in available ions significantly increases the rate at which target material is eroded and subsequently deposited onto the substrate.

The ensuring process might be compared to a find sand blasting in which the momentum of the bombarding particles is more important than their energy. The inserted argon gas is chosen because it is a heavy rare gas and is plentiful. It also has a low ionization potential.

Figure 4.4 shows the film by using photolithography. The width of the film is 50 μm. Silver plaster is used to stick four copper wires with diameter 50μm on the four electrodes with 0.5 mm square.

The talbe 4.1 shows the sputtering parameters for all films. The pressure is the chamber pressure during deposition and thinkness is the deposed thinkness of films. In the system, we use two kinds of mask, metal mask and photomask. The deposition rates are basically proportion to the sputtering powers.

4.3 Low Temperature Resistance and Magnetoresistance Measurement

After finishing preparing the samples, we will mount our samples onto the cryostat to do low temperature transport measurement. In low temperature measurements, it is the first step for accurate measurements that electron temperature is the same as the thermometer temperature, otherwise the hot electron physics occur. There are two easy ways to confirm that whether the samples are real cooled down. First one is that the joule heat of the system, I^2R, is much smaller than the cooling power of refrigerator. The accuracy of the method is not high, because it does not take into account of the joule heat of the conducting wire and therm-conductivity between sample and sample holder. Second way, which

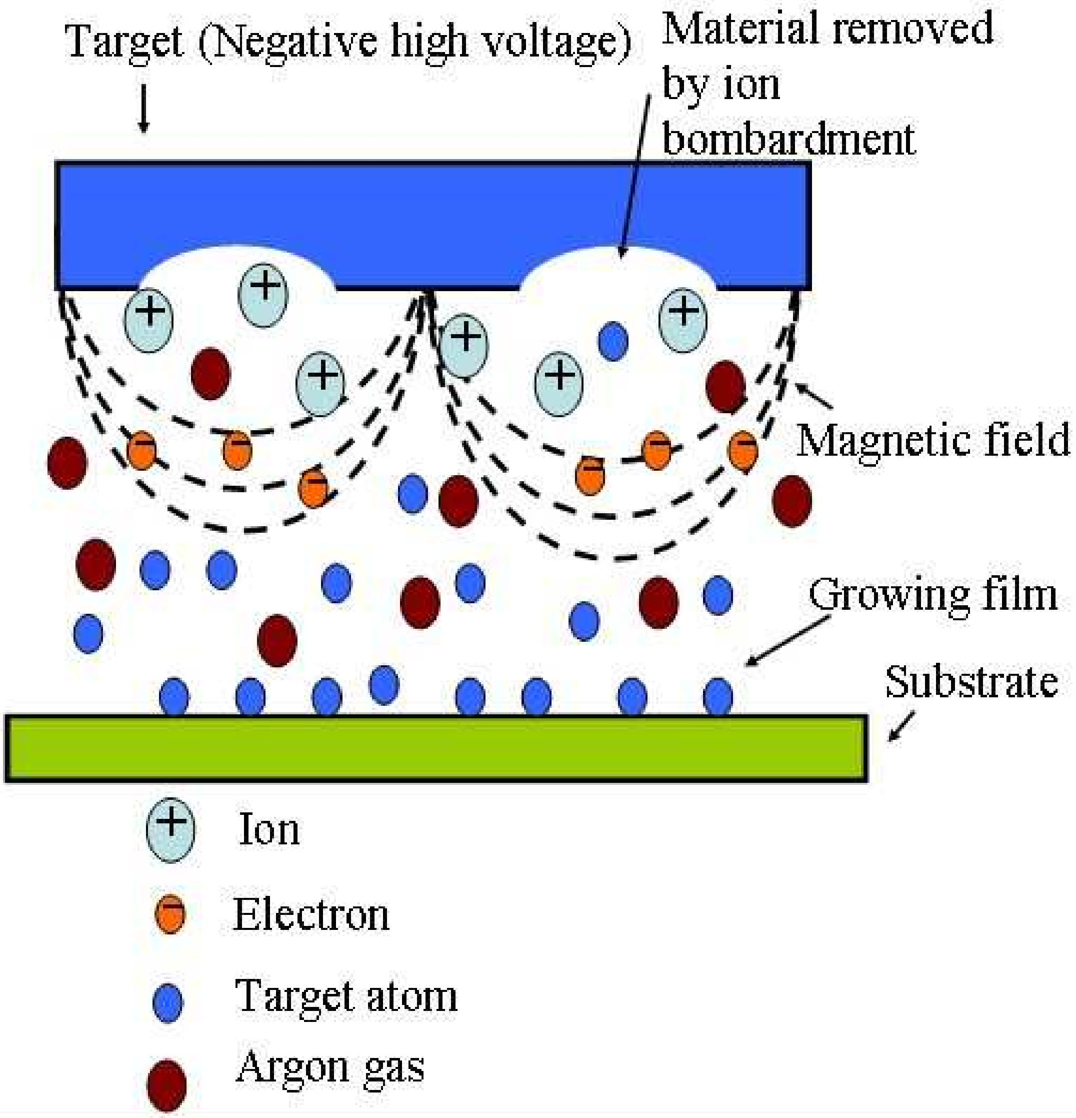

Figure 4.3: Principle of planar magnetron sputtering.

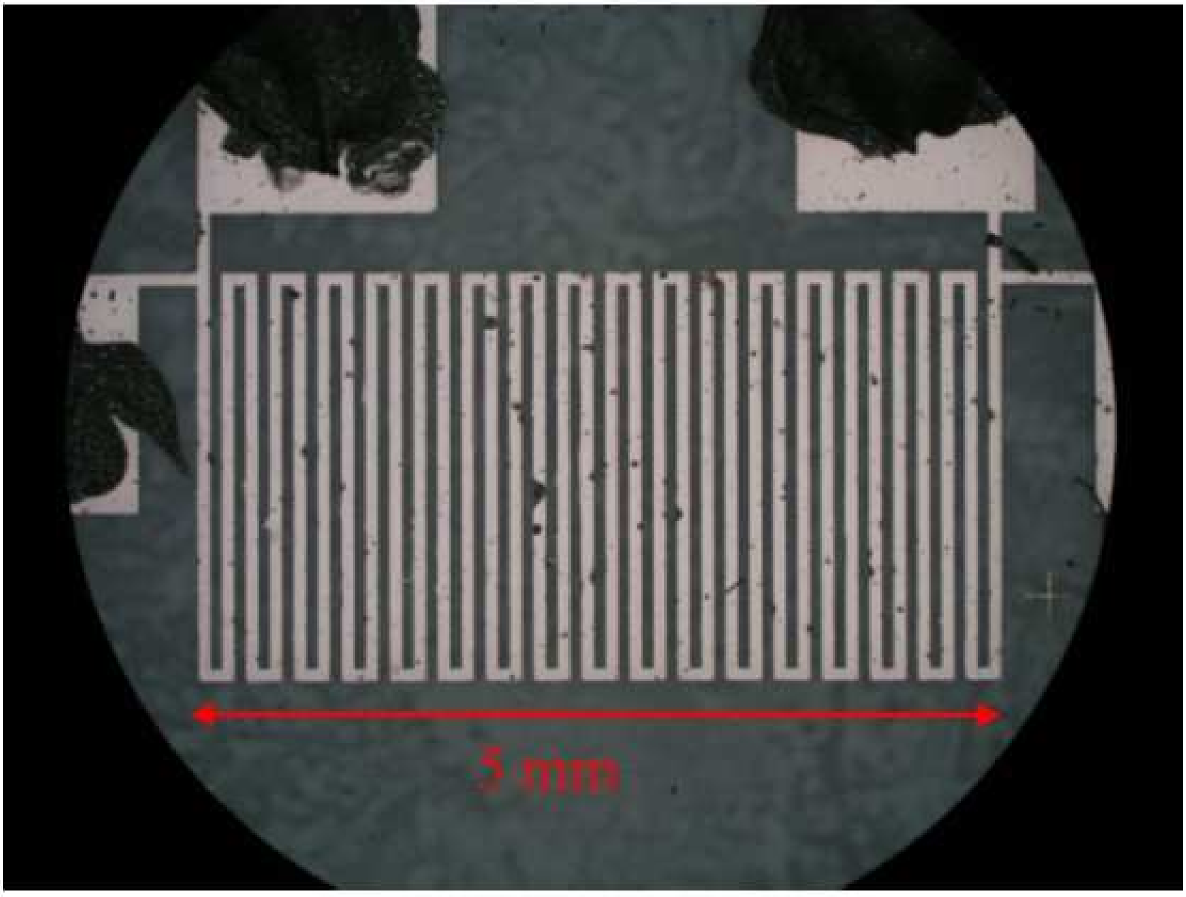

Figure 4.4: The picture of film which is fabricated by photolithography.

Table 4.1: Sputtering parameters of $Cu_{93}Ge_4Au_3$ films.

Sample	Power (W)(DC)	Ar gas (sccm)	Pressure (mbar)	Thickness (Å)	Deposing rate (Å/sec)	Mask
16-3	110	7	1.7×10^{-3}	191	5.0	Metal
18-2	80	7	1.6×10^{-3}	199	4.5	Metal
18-4	80	7	1.6×10^{-3}	199	4.5	Metal
26-2	10	7	1.7×10^{-3}	196	0.4	Metal
27-3	60	7	1.6×10^{-3}	145	3.0	Metal
31-3	90	7	1.6×10^{-3}	149	4.5	Metal
38-1	90	7	1.6×10^{-3}	146	4.2	Photo
40-1	20	7	1.6×10^{-3}	145	0.8	Photo
41-1	30	7	1.6×10^{-3}	150	1.4	Photo
43-1	90	7	1.7×10^{-3}	153	4.3	Photo
44-1	90	7	1.7×10^{-3}	153	4.2	Photo

is more accurate, is that the ”electron-phonon relaxation energy” is much smaller than thermo-energy.

$$k_B T \gg eV_{ep} = eL_{ep}\varepsilon, \tag{4.1}$$

where k_B is Boltzmann constant and T is temperature of sample. e is electron charge, V_{ep} and L_{ep} are the electron-phonon relaxation voltage and length. ε is the applied voltage across the energy relaxation length. We carefully check it in both two ways during both resistance and magnetoresistance measurements to insure the electron temperature is consistent with the thermometer temperature.

In my experiments, we have used three kinds of cryostats which possess different cooling powers and base temperatures. We briefly discuss their operating principles.

4.3.1 ^{4}He Cryostat

As we known, the boiling temperature of liquid helium is 4.2 K at 1 atmospheric pressure. In general, we dip a cryostat with vacuum shell and the temperature would goes down to 4.2 K gradually. We add a little bit heat around samples to increase and stabilize the temperature above 4.2 K. The temperature range between 1.3 K and 4.2 K is determined by the normal boiling point of ^{4}He. There are two ways to access this temperature range using pumped liquid ^{4}He. First one is pumping the vapor above the liquid ^{4}He bath away to decrease its temperature, but this is very uneconomical because about 40% of the liquid ^{4}He has to be evaporated to cool it from 4.2K to 1.3K, due to the large change of its specific heat in this temperature range. The second one is what we use. Figure 4.5 shows the operating principle of 1K cryostat. In this kind of cryostat a small fraction of the liquid from main 4.2 K bath flows through a suitable flow impedance into a small vessel which located in a vacuum cane inside the cryostat. Through the central tube we pump on the liquid arriving in this evaporation vessel. As discussed above, one can control the pumping rate modulating the vapor pressure of the liquid ^{4}He in the vessel to control the temperature. For commercial cryostat the cooling power is about several mW at 1.3 K.

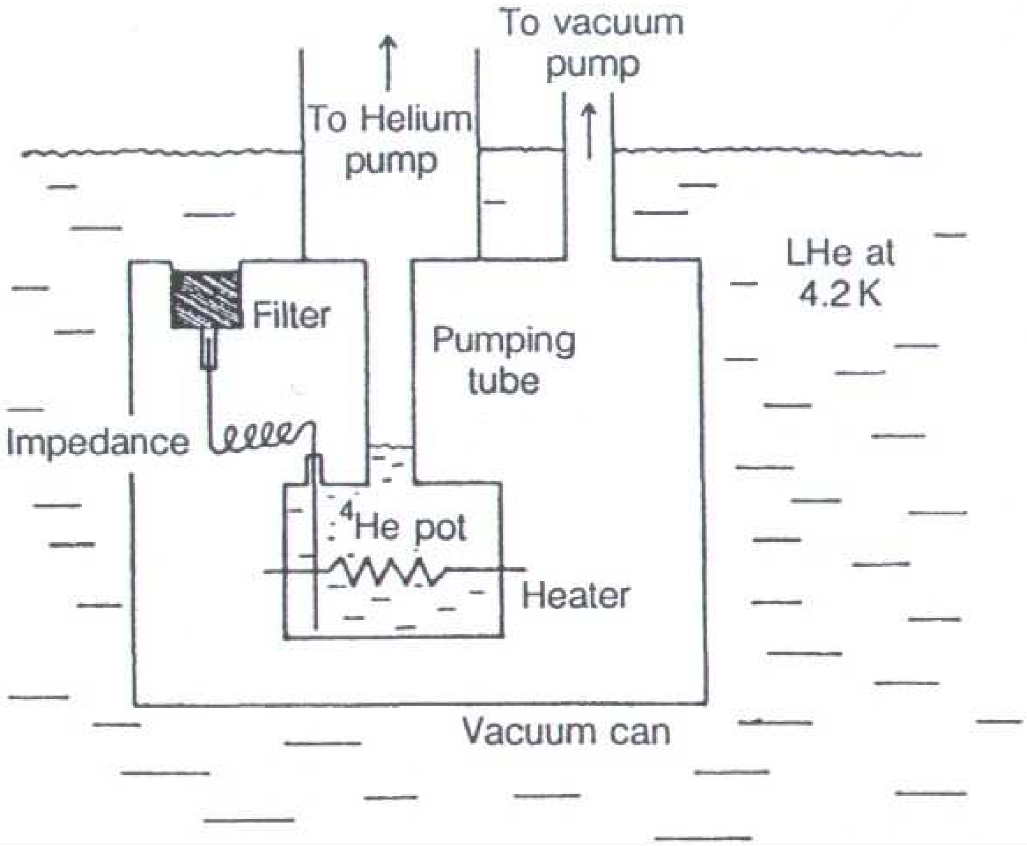

Figure 4.5: The operating principle of 1K cryostat.

4.3.2 ^{3}He Cryostat

The accessible lowest temperature with a liquid ^{4}He bath is typically 1.3 K, but the lowest temperature range can be extended to about 0.3 K if the rare isotope ^{3}He is used instead of the common isotope ^{4}He. The main reason is that ^{3}He has a substantially larger vapor pressure than ^{4}He at the same temperature. The ^{3}He cryostat we use is a commercial cryostat. The ^{3}He bath is pumped using cold charcoal with large surface area. The design is shown in the Fig. 4.6. There is a ^{3}He gas storage at the top of the cryostat. Gas is trapped at the cold area. When the temperature of the ^{3}He pot is below 3 K, the ^{3}He gas from gas storage will start to condense at the ^{3}He pot. During the ^{3}He condensation, we should heat up the charcoal making almost the ^{3}He gas can condense to the ^{3}He pot. After complete condensation, cooling down the temperature of charcoal to adsorption pump the ^{3}He bath and cool it down. When all the ^{3}He has been pumped away, so the ^{3}He pot is empty, we just have to left the charcoal pumping system in to a space at higher temperature in the cryostat desorb the ^{3}He, which will then enter the gas phase, condense at the cold surfaces of the cryostat and eventually drip back down into the ^{3}He pot. The cooling power is about 100 μW at 0.3 K and the base temperature is about 0.25 K.

4.3.3 Dilution Refrigerator

In the 1K cryostat and ^{3}He cryostat the cooling is occurred using evaporation of ^{4}He and ^{3}He. In the dilution refrigerator the cooling occurs because ^{3}He atoms from the pure ^{3}He gas dissolve into a diluent liquid with 6.6 percent ^{3}He an 93.4 percent ^{4}He. The simplest way to realize it is that the strong bonds between the ^{3}He atoms are broken and new weaker bonds appear between the ^{3}He atom in the dilute phase. A net absorption of energy occurs in the process and results in cooling.

Figure 4.7 shows the main components of a working dilution refrigerator and a flow diagram for its liquids. The ^{3}He gas coming from the exit of a pump at room temperature will first be precooled by a liquid ^{4}He bath at 4.2K. It will then be condensed in a second ^{4}He bath at about 1.5K, which we can obtain by using a continuously operating ^{4}He refrigerator. The liquified ^{3}He will flow through

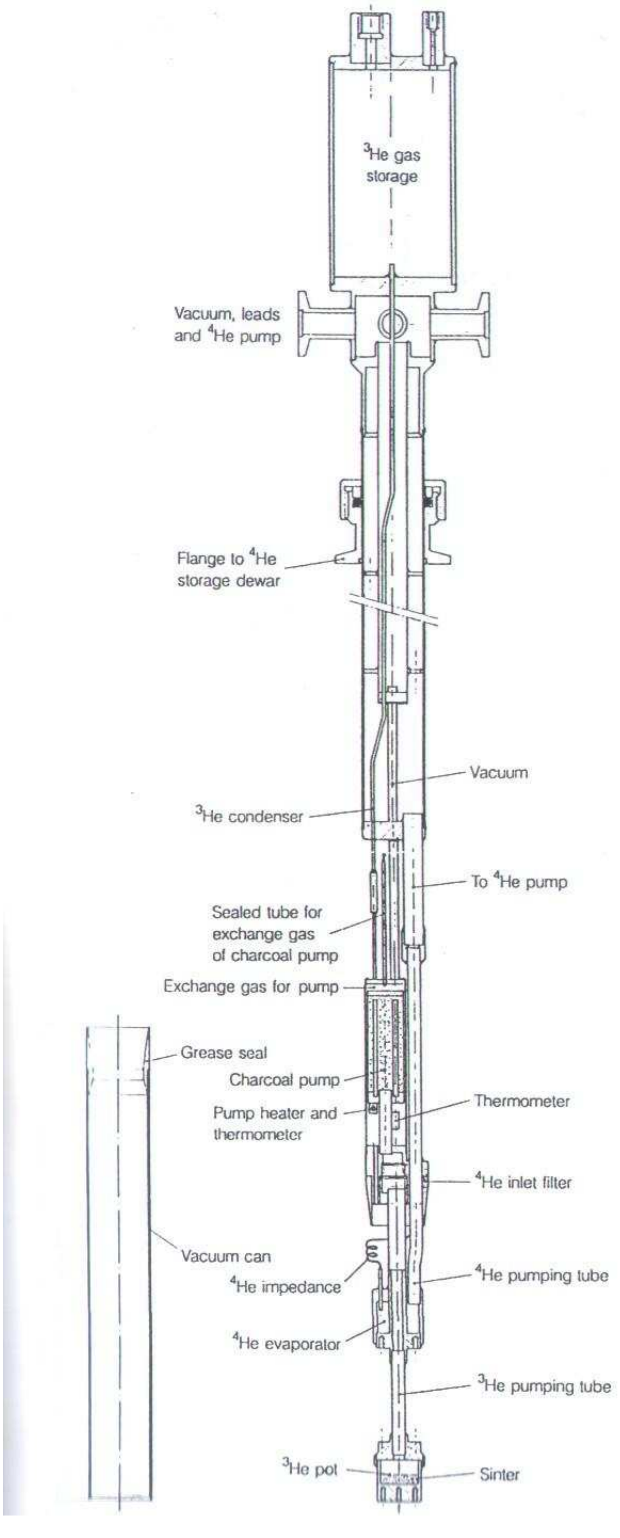

Figure 4.6: The operating principle of ^{3}He cryostat.

a heat exchanger which is in thermal contact with the still at a temperature of about 0.7 K. After that the liquid ^{3}He will flow several heat exchangers to precool it to a low enough temperature before it enter the concentrated phase in mixing chamber.

A wider tube for the dilute phase in the refrigerator leaves the lower, dilute mixture phase of the mixing chamber, and then goes the heat exchanger to precool the incoming ^{3}He. It enters the dilute liquid phase in the still, where we have a liquid ^{3}He concentration of less than 1%. The vapor above the dilute liquid phase in the still has a concentration of typically 90% ^{3}He due to the high vapor pressure of ^{3}He at the temperature of the still. We pump on the still and supply them to the condensation line. It runs cyclically and gives rise to cooling. The base temperature of dilution refrigerator is about several mK and the cooling power is about 1 μW at 10 mK.

4.3.4 Superconducting Magnet

In the series measurements, we measured magnetoresistance at low magnetic fields and temperature dependent resistance at high magnetic fields. In order to save energy and keep the measuring system at low temperature, we use superconductor magnet. The superconductor material is NbTi with $T_c \approx 9K$.

Figure 4.8 shows the schema of a superconductor magnet. There are two main operating mode, sweeping mode and persistent mode. In the sweeping modes, we should heat up the superconductor wire at "persistent current switch" to breaking its superconductivity, so that all of the applied current will go to the main superconductor solenoid. One can sweep the magnetic field and modulate its amplitude by the applied current using power supply. While one would like to keep a magnetic field for a long time, it is better to use the persistent mode to save energy. The method is that sweeping the magnetic field to the anticipated amplitude by sweeping mode. Once the magnetic field reaches the expected value, turn off the heater at the wire at "persistent current switch" and let the wire to cool down to become superconductivity. Last, sweep down the current of power supply and the current in superconductor magnet would permanently flow in the loop of superconductor wire.

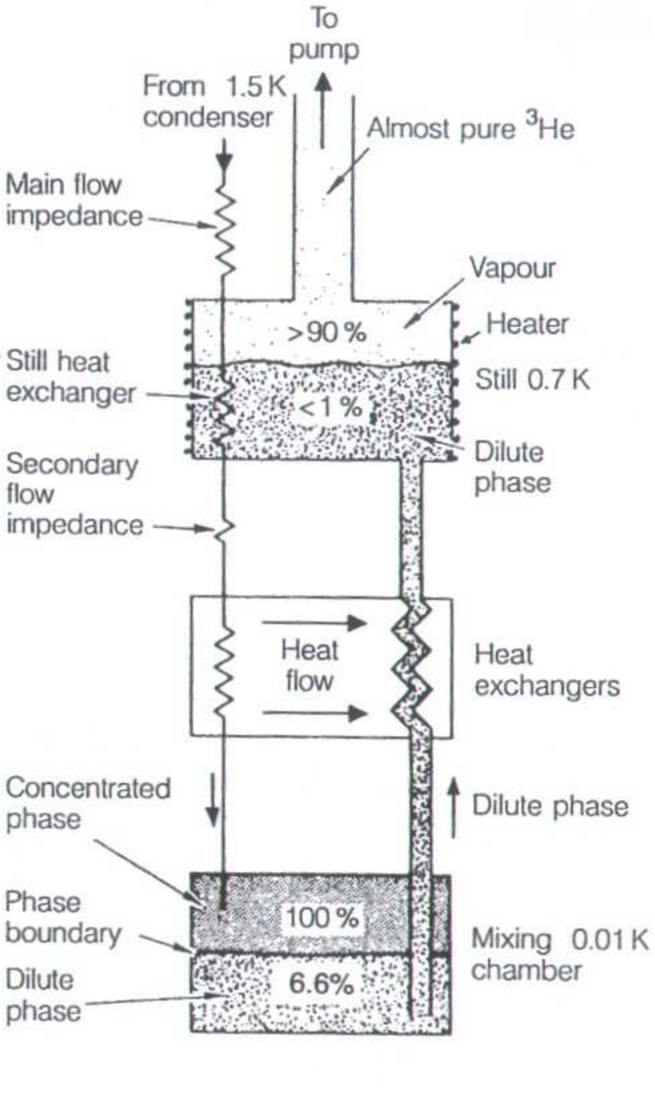

Figure 4.7: The operating principle of dilution refrigerator.

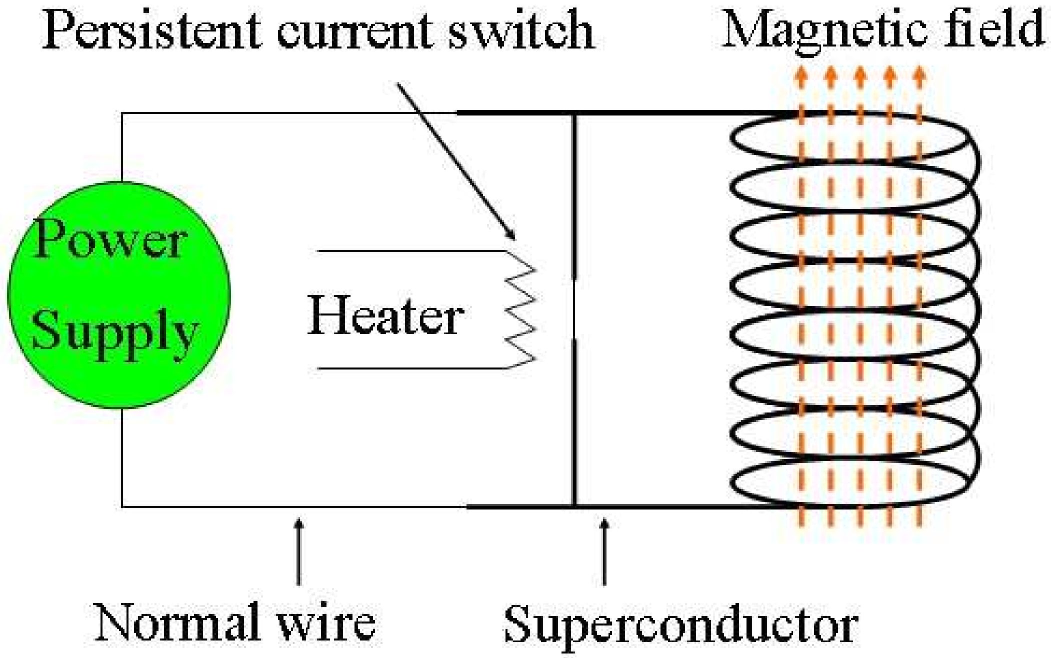

Figure 4.8: Operating principle of superconductor magnet.

4.4 Measuring Circuit and Noise

High accurate measurement is critical for good research. Significant errors can be generated by noise sources, which include Johnson noise, magnetic fields, and ground loops. An understanding of these noise source and the methods available to minimize them is important.

4.4.1 Measuring Circuit

Figure 4.9 is the schema of our measuring circuit. Four-probe measuring method is used to avoid the contact resistances. Constant currents come from connecting the AC voltage with a large value resistor which is high accurate and insensitivity to the environments. The voltage drop is enlarge by a pre-amplifier. The ratio transformer is used to offset a constant voltage and the lock-in amplifier can read a small voltage change by weak localization effect. In our experiment, we use "Linear Research 400 four-wires AC Resistance Bridge" which contains "AC current source", "pre-amplifier", "ratio transformer", and "lock-in" with frequency 15.7 Hz and the analog voltage is extracted by Keithley 182 sensitivity digital voltmeter. The data is continuously taken by computer (it is not shown in the schema).

4.4.2 Johnson Noise

The Johnson noise is also called thermal noise. This noise is the voltage associated with the motion of electrons due to their thermal energy at temperatures above 0 K. This voltage is related to the temperature, noise bandwidth, and the source resistance. The noise voltage developed by a metallic resistance can be calculated from the following equation:

$$V = \sqrt{4k_B TBR}, \tag{4.2}$$

where V is rms noise voltage. k_B is Boltzmann constant. T is absolute temperature. B is noise bandwidth. R is resistance of the source. Johnson noise can be reduced by lowering the temperature of the source resistance and by decreasing the bandwidth of the measurement. Using the "Linear Research 400 four-wires

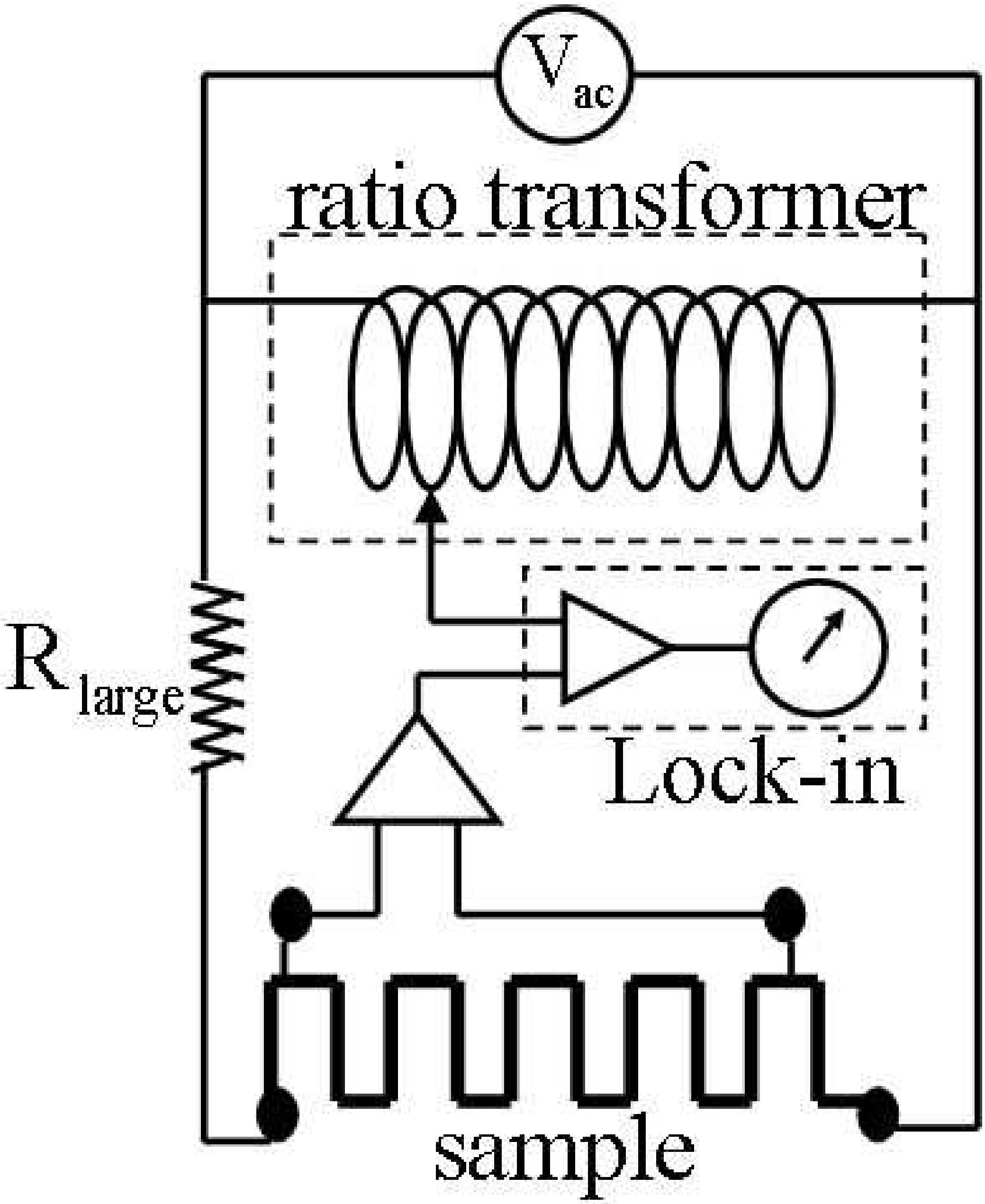

Figure 4.9: The schema of measuring circuit.

AC Resistance Bridge", the thermal noise voltage is about 10^{-8} V for samples with resistance 1 KΩ at room temperature.

4.4.3 Eddy Current

Faraday's low tells us that the change of the magnetic flux, Φ_B, would induce a voltage in a circuit.

$$V_B = \frac{d\Phi_B}{dt} = \frac{d(\vec{B} \cdot \vec{A})}{dt} = \vec{B} \cdot \frac{d\vec{A}}{dt} + \vec{A} \cdot \frac{d\vec{B}}{dt}, \tag{4.3}$$

where V_B is the induced voltage. $\vec{A}$ is the loop area. $\vec{B}$ is magnetic field.

There are two main sources to generate the voltage. First one is that the field is changing with time. Second one is that the relative motion between the circuit and the field. The voltage can be generated from the motion of a conductor in a magnetic field, from local AC currents, or from the sweeping of the magnetic field, such as for magnetoresistance measurements.

To minimize induced voltage, lead must be run close together and be kept short and rigidly tied down. A twisted pair is used to reduce the loop area and cancel magnetically induced voltage, because each adjacent twist couples a small but alternating polarity voltage.

In our experiments, we swept the magnetic fields very slowly to avoid the noise. The sweeping rates range from 3 Gauss per sec to 0.5 Gauss per second.

4.4.4 Ground Loop

Noise also can come from the ground loop. When there are two connections to earth, such as when the source and measuring instruments are both connected to a common ground, a loop is formed as shown in Fig. 4.10. A voltage, $V_g = V_m - V_s$, between the source and instrument grounds will cause a current to flow around the loop. This current will create an unwanted voltage in series with the source voltage.

A typical example of a ground loop can be seen when a number of instruments are plugged into power strips on different instrument racks. Frequently, there is a small difference in potential between the ground points. This potential difference can cause large currents to circulate and create unexpected voltage drops.

The easiest way too avoid this ground loop noise is ground all equipment at a single point and use isolated power sources and instruments. This noise also can be reduced by using a voltage with high common mode impedance.

4.4.5 Filter

To avoid the high frequency noise goes into the samples to heat up electrons by means of conducting wires, low pass filters are used. we use two kinds of filters in the series of measurements. The first kind of filters is the RC filter and the other kind of filters is ferrite bead. Figure 4.11 shows the schema and the frequency response of low pass filter. Ferrite bead is made of high inductance material. The schema of ferrite bead is shown in Fig. 4.12. When a constant current passes through the ferrite bead, it does not work. Following the Faraday's law $V = -L\frac{dI}{dt}$, once a AC current passes through it, the ferrite bead will create a voltage to attenuate the current. It acts like a inductor. Combined with resistance of wire, it works as a low pass filter.

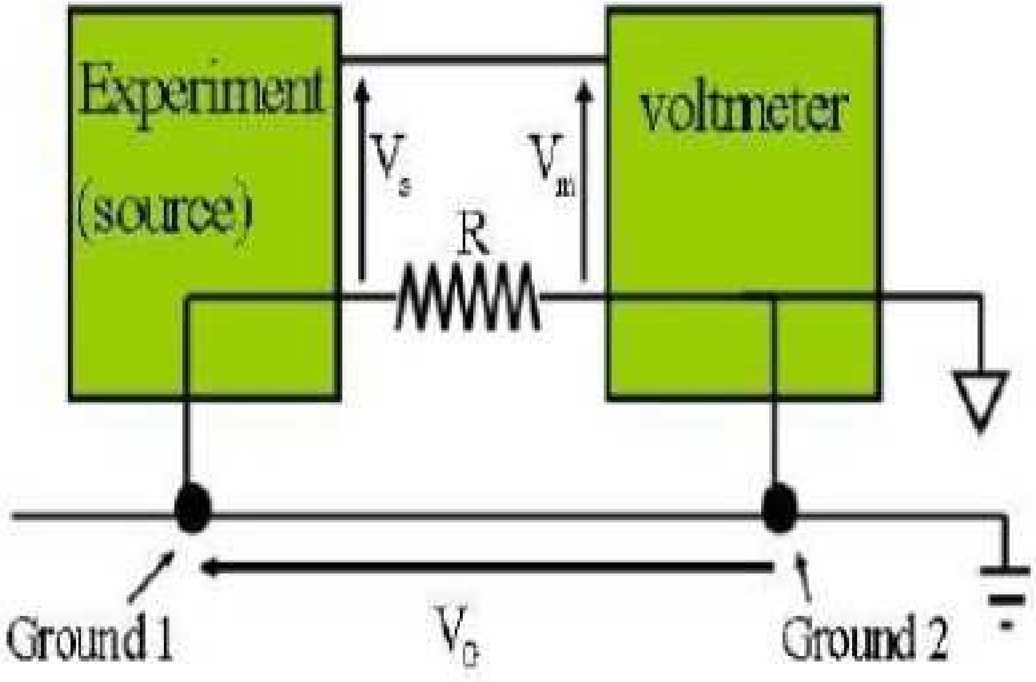

Figure 4.10: The schema of ground loop noise.

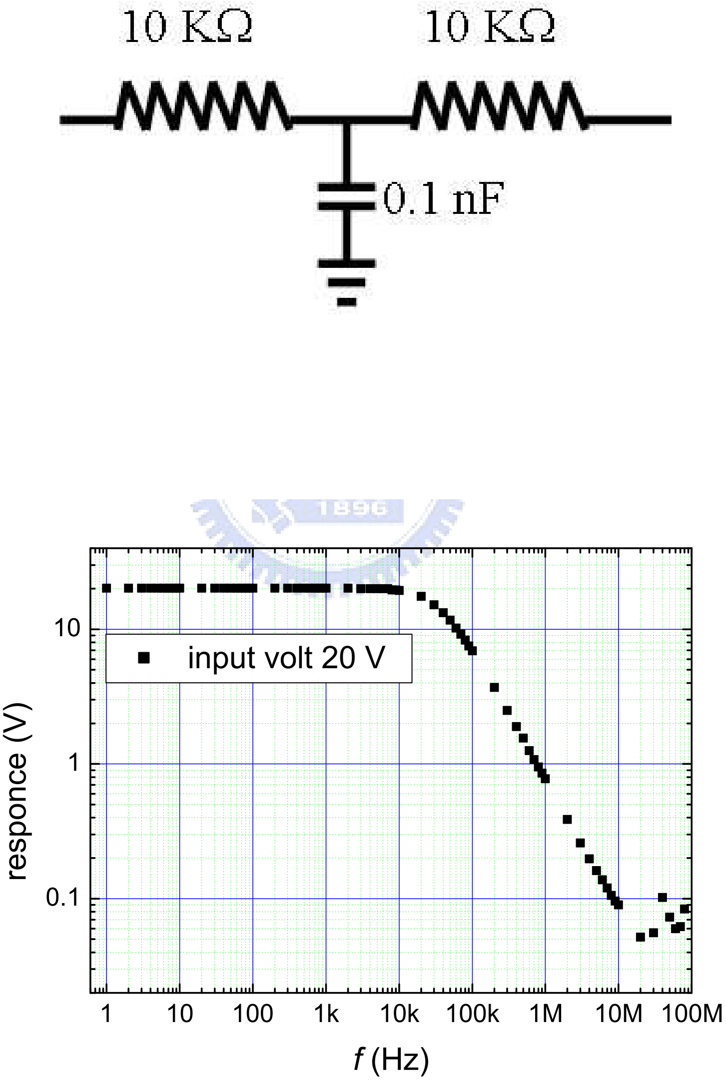

Figure 4.11: The schema and the frequency response of low pass filter.

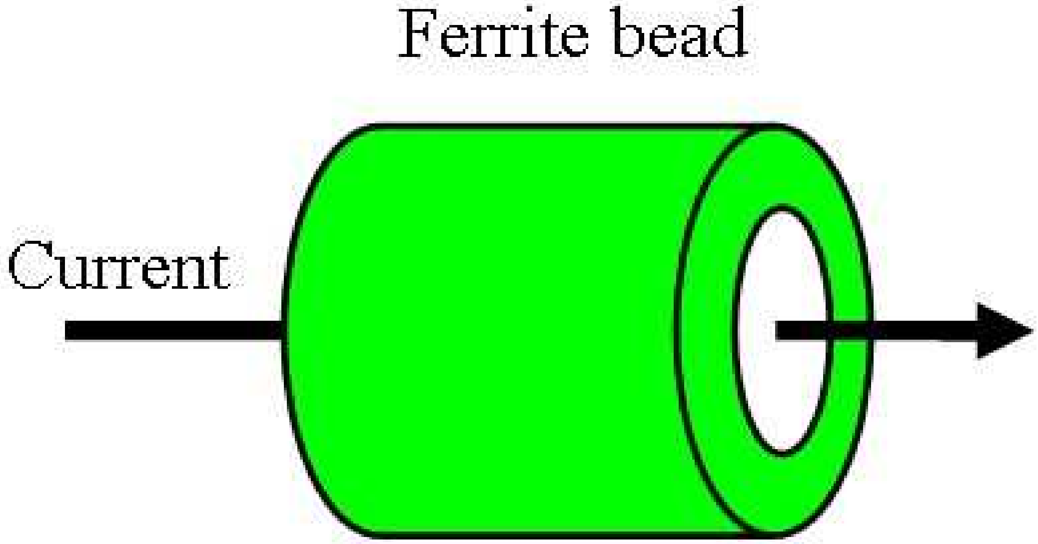

Figure 4.12: The schema of ferrite beat.

Chapter 5

Results and Discussions

5.1 Introduction

In this chapter, we will discuss our experimental results in $Cu_{93}Ge_4Au_3$ thin films. A series of films with different levels of disorder are prepared by DC sputtering deposition of different depositing rates. We measure resistance both as a function of temperatures and magnetic fields. Low magnetic field magnetoresistances (< 1 T) are measured and fitted in weak localization theory to extract electron inelastic scattering times. Roughly speaking, the measured inelastic scattering time can be divided into three different temperature regions. At the temperatures higher than 10 K, electron-phonon scattering dominates the inelastic scattering times. The inelastic scattering time is a constant value at the temperature region between 10 K and 6 K. When temperature is below 6 K, the inelastic scattering time increases as temperature decreasing. The increasing rates are sample dependence. The increasing rates of inelastic scattering times below 6 K are more drastic in more disordered samples. We have discussed the measured inelastic scattering time in electron-electron scattering time, electron-phonon scattering time, and spin-spin scattering time (Kondo effect). The measured inelastic scattering time is 2 order of magnitude smaller than the electron-electron interaction scattering time of theoretical predictions. The Kondo effect fails to explain the results quantitatively. Further discussions support that the dynamic structure defeat scattering dominates the measured inelastic scattering times at low temperatures. The temperature dependent resistances for a wide range, from above

10 K to 30 mK, at different magnetic fields are also measured. The results show that the the temperature dependent resistances are logarithmic increasing as temperature decreasing. In particular, the lnT dependence is insensitive to magnetic field up to 15 T. Moreover, the logarithmic temperature dependent resistance appears in both thin films (150 $\AA$) and thick films (5000 $\AA$ $\sim$ 6000 $\AA$). All of the experimental results support that the dynamic structure (two-level system) scattering dominates the inelastic scattering time.

5.2 Sample Background

Our samples are $Cu_{93}Ge_4Au_3$ films. The host material is copper, and 4% germanium are doped to increase the impurity scattering to enhance the weak localization effect. That increases the change of magnetoresistances and increases the accuracy of measurements. 3% gold are doped to increase the spin-orbit interaction. In the limit of strong spin-orbit scattering, the inelastic scattering time becomes the only free parameter in the comparison of the experimental magnetoresistances with the weak localization theory and it makes the extraction of inelastic scattering time highly reliable. The target is a commercial one. The target is chosen to be a medium purity (99.99%). Figure 5.1 shows the spectrographic analysis of our source target and indicates that there are low levels of magnetic impurities, 4 ppm iron, 0.3 ppm manganese, and 0.003 ppm chromium.

5.3 Magnetoresistance

We have measured the magnetoresistance of all films in small magnetic fields ($<$ 1 T). Figure 5.2 shows perpendicular magnetoresistances at several temperatures. The color dots are the measured data and the black dots are the theoretical prediction of weak localization. The magnetoresistances are positive at all our measured temperature range ($<$ 20 K), and it indicates that spin-orbit interaction is strong in our system. The behaviors of magnetoresistances which are predicted by weak localization theory are shown in Eq. 3.15. Typically, the $H_e \gg H_{so}, H_i,$ and H_s, so the $H_1 \approx H_e$. In the limit of the strong spin-orbit interaction, the $H_{so} \gg H_i$ and H_s, so the $H_2 \approx H_{so}$. It is noticeable that the H_{so} is only material

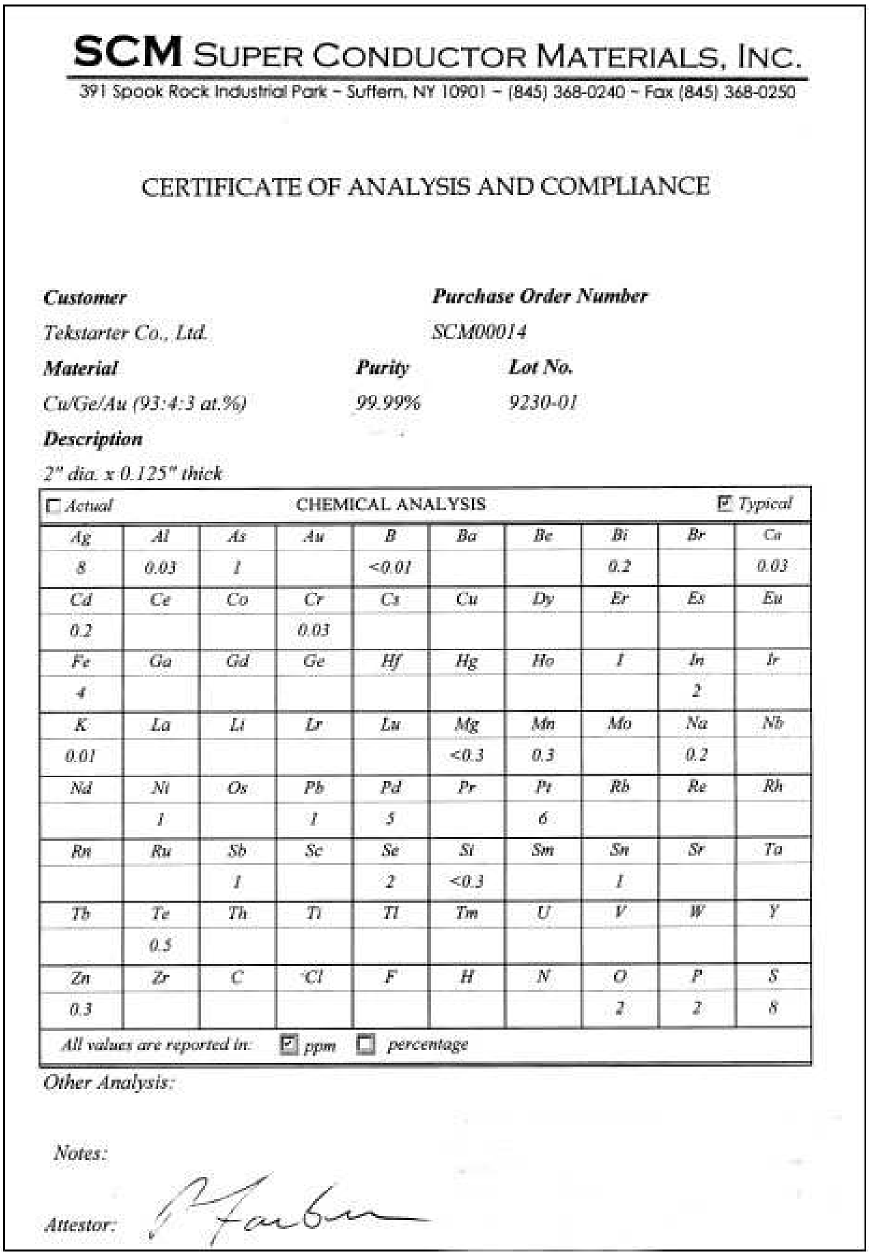

SCM SUPER CONDUCTOR MATERIALS, INC.

391 Spook Rock Industrial Park – Suffern, NY 10901 – (845) 368-0240 – Fax (845) 368-0250

CERTIFICATE OF ANALYSIS AND COMPLIANCE

Customer

Tekstarter Co., Ltd.

Purchase Order Number

SCM00014

Material

Cu/Ge/Au (93:4:3 at.%)

Purity

99.99%

Lot No.

9230-01

Description

2" dia. x 0.125" thick

☐ *Actual* CHEMICAL ANALYSIS ☑ *Typical*

Ag	*Al*	*As*	*Au*	*B*	*Ba*	*Be*	*Bi*	*Br*	*Ca*
8	*0.03*	*1*		*<0.01*			*0.2*		*0.03*
Cd	*Ce*	*Co*	*Cr*	*Cs*	*Cu*	*Dy*	*Er*	*Es*	*Eu*
0.2			*0.03*						
Fe	*Ga*	*Gd*	*Ge*	*Hf*	*Hg*	*Ho*	*I*	*In*	*Ir*
4								*2*	
K	*La*	*Li*	*Lr*	*Lu*	*Mg*	*Mn*	*Mo*	*Na*	*Nb*
0.01					*<0.3*	*0.3*		*0.2*	
Nd	*Ni*	*Os*	*Pb*	*Pd*	*Pr*	*Pt*	*Rb*	*Re*	*Rh*
	1		*1*	*5*		*6*			
Rn	*Ru*	*Sb*	*Sc*	*Se*	*Si*	*Sm*	*Sn*	*Sr*	*Ta*
		1		*2*	*<0.3*		*1*		
Tb	*Te*	*Th*	*Ti*	*Tl*	*Tm*	*U*	*V*	*W*	*Y*
	0.5								
Zn	*Zr*	*C*	*Cl*	*F*	*H*	*N*	*O*	*P*	*S*
0.3							*2*	*2*	*8*

All values are reported in: ☑ *ppm* ☐ *percentage*

Other Analysis:

Notes:

Attestor:

Figure 5.1: Spectrographic analysis

Table 5.1: Physical parameters of samples

Sample	Thickness ($\mathring{A}$)	ρ(300K) ($\mu\Omega\,cm$)	ρ(10K) ($\mu\Omega\,cm$)	D(10K) (cm^2/s)	$R_\square$(10K) (Ω)	αP+1-0.75F
16-3	191	31.2	27.7	6.79	14.17	1.21
18-2	199	72.0	65.7	2.94	33.01	1.36
18-4	199	57.4	50.9	3.79	25.57	1.38
26-2	196	50.9	45.6	4.24	23.26	1.49
27-3	145	60.2	55.4	3.49	38.20	1.32
31-3	149	31.6	27.6	7.00	18.52	1.28
38-1	146	25.2	24.1	8.00	16.53	1.21
40-1	145	94.6	94.3	2.05	65.06	1.32
41-1	150	23.8	22.1	8.73	14.76	2.02
43-1	153	15.2	13.7	14.1	8.96	1.35
44-1	153	16.1	14.5	13 .0	9.47	1.12

dependence and independent of temperatures and magnetic fields and therefore there is only one free parameter for fitting the data with the theoretical predictions. The results show that the measured data go well with the prediction of weak localization theory. It makes us strongly believe that the extracted inelastic scattering is highly reliable. Second, we observe that the magnetoresistances are larger at lower temperatures. This can be understood in the following way. The magnetoresistances of weak localization arise from the inelastic scattering time. As the temperature is reduced, the inelastic scattering time increases.

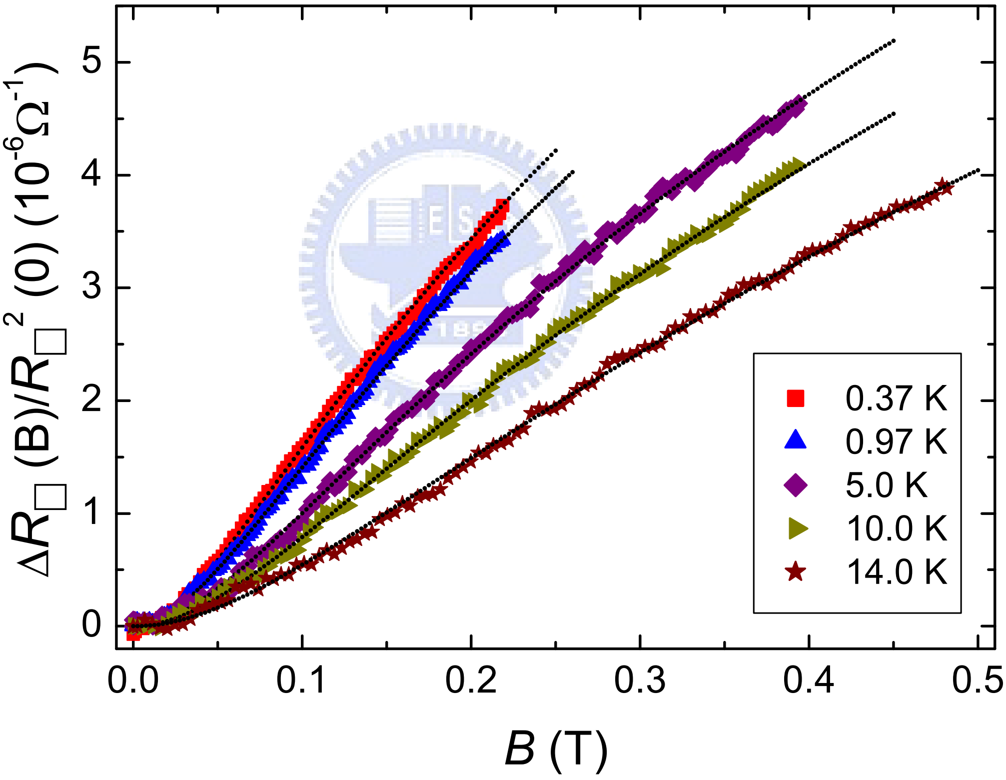

Figure 5.2: Magnetoresistances of Cu 38-1 at several temperatures.

The Fig. 5.3 shows the dephasing time which is extracted from the magnetoresisances of Fig. 5.2 as a function of temperature. The inelastic scattering

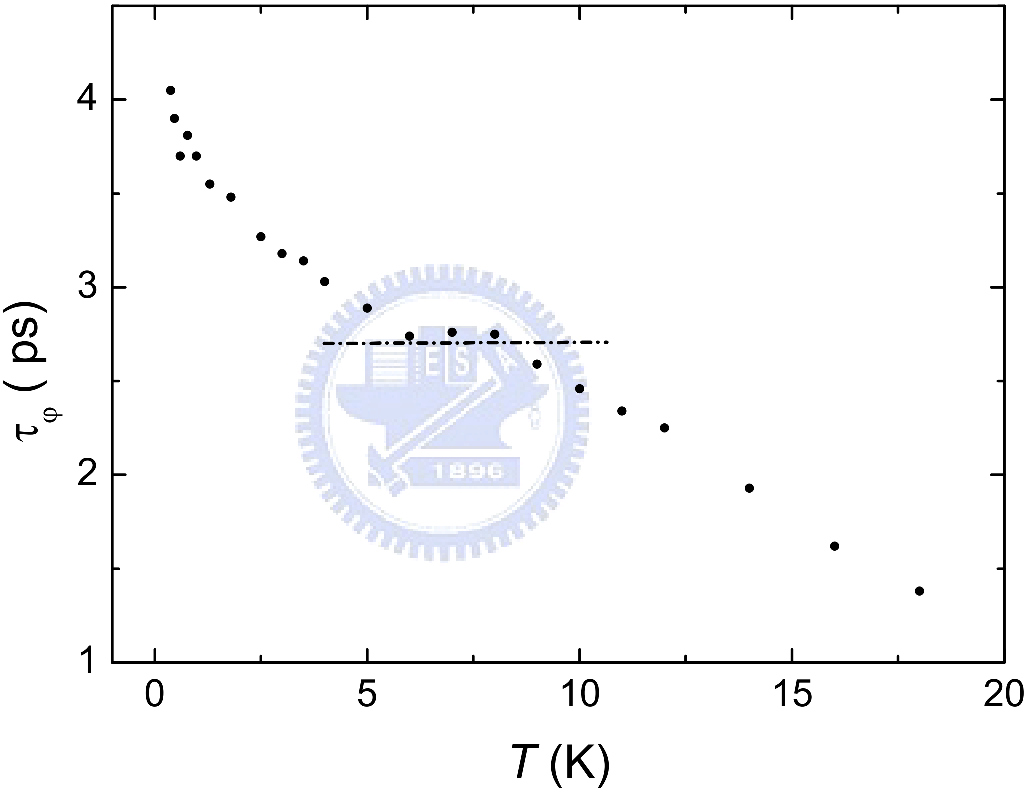

Figure 5.3: Dephasing time of Cu 38-1 as a function of temperature.

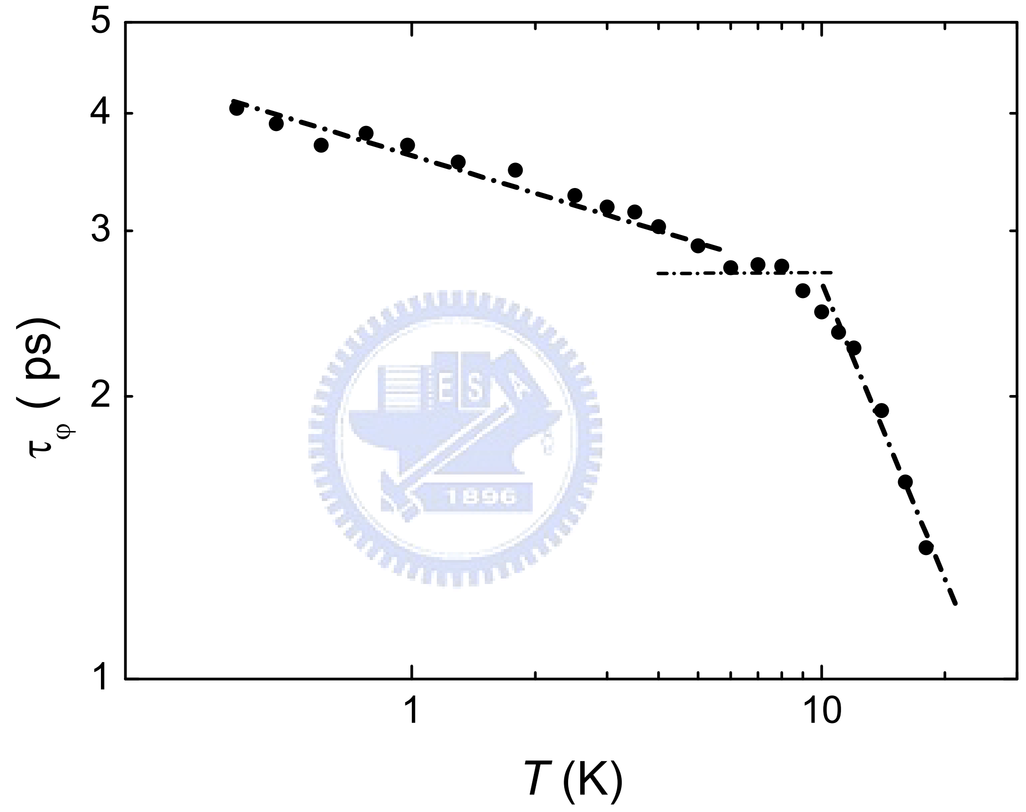

Figure 5.4: Dephasing time of Cu 38-1 as a function of temperature in double-logarithmic scales.

times are several pico-second. It is about 1.3 ps at 20 K and 4 ps at 0.3 K. Roughly speaking, the inelastic scattering times increase as temperature decreasing, except the inelastic scattering between 10 K and 6 K. It behaviors a weak temperature dependence and the inelastic scattering time is about 2.7 ps.

The phonon vibration is strong at high temperature and typically, electron-phonon scattering dominates the inelastic scattering times at high temperature. It is found that the electron-phonon scattering time dominates the inelastic scattering time above 10 K and is only important above 10 K.

Figure 5.4 shows the same data with Fig. 5.3 but in double-logarithmic scales. It shows that the dephasing time above 10 K can be well described by the electron-phonon interaction. It gives the results that $\tau_{ep} \propto T^{-2}$ nsec K^{-2}.

As a first check of the temperature dependence of the measured dephasing time below 5 K, we use an effective power law, $\tau_\varphi \propto T^{-p}$, and compare it with dephasing time to extract the value of p. It shows that the p is about 0.1 for the sample, Cu 38-1.

From fig. 5.5 to Fig. 5.7 show a series of magnetoresistances of samples with different levels of disorder. The magnetoresistances are larger at lower temperatures for all samples. This is consistent with the prediction of weak localization theory. The weak localization theory can describe all of the magnetoresistances well and all of the errors are less than 1%. One more interesting thing in the series of magnetoresistances is that intervals between two magnetoresistances which are measured below 5 K are larger for samples with higher levels of disorder. It is a mimic of sample dependent increasing rates of inelastic scattering times below 5 K.

Figure 5.8 shows the extracted inelastic times of all samples with different sheet resistances as a function of temperature. The respective sheet resistances of 9 K are shown in the insect. Except sample 43-1 and sample 44-1, all of the dephasing times of each samples have been vertically shifted 2 ps one by one for clarity. There are two more distinct features in the serious of inelastic scattering times. First one is that the inelastic scattering times possess a very weak temperature dependence between 10 K and 5 K for all samples and the inelastic scattering times have a very similar magnitude, 2 ps $\sim$ 3 ps, in this plateau regime. Second one is that the dephasing times increase with decreasing

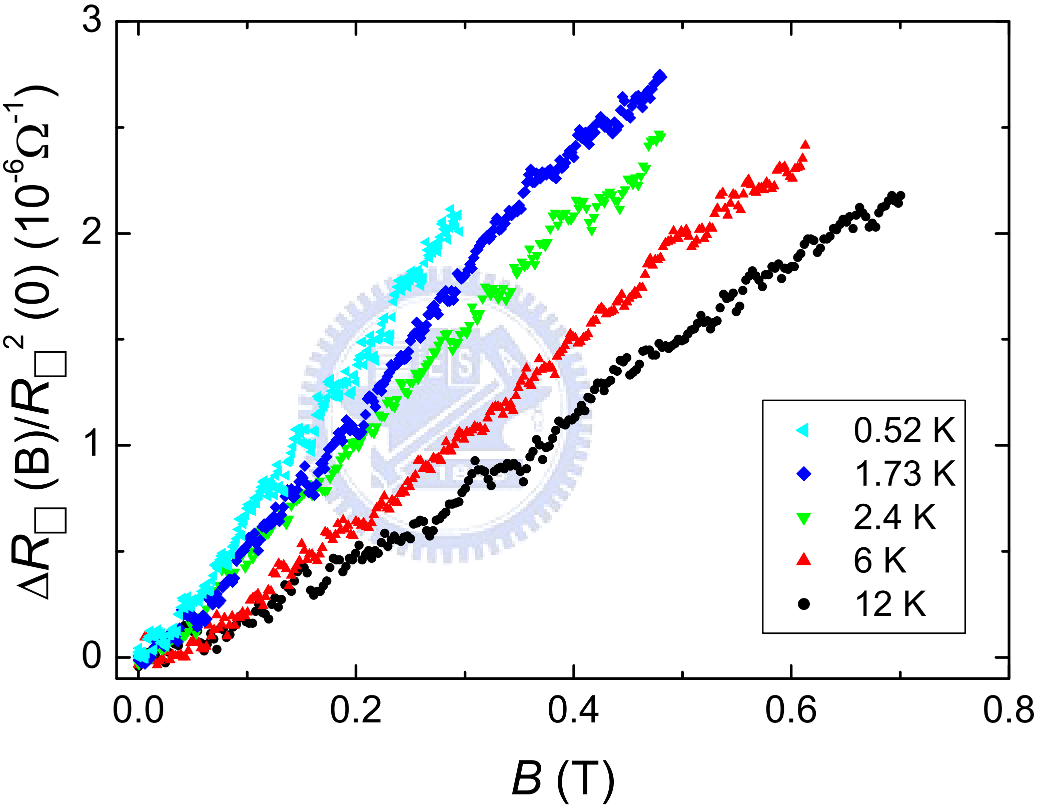

Figure 5.5: Magnetoresistances of Cu 18-2 at several temperatures.

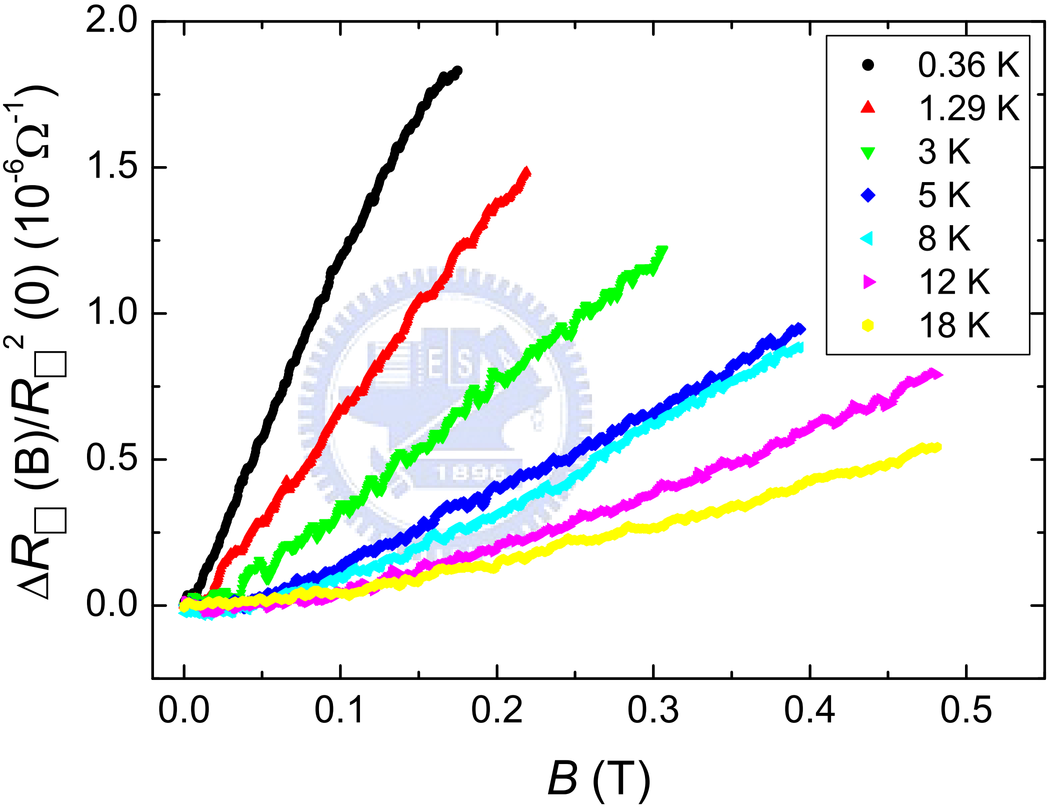

Figure 5.6: Magnetoresistances of Cu 40-1 at several temperatures.

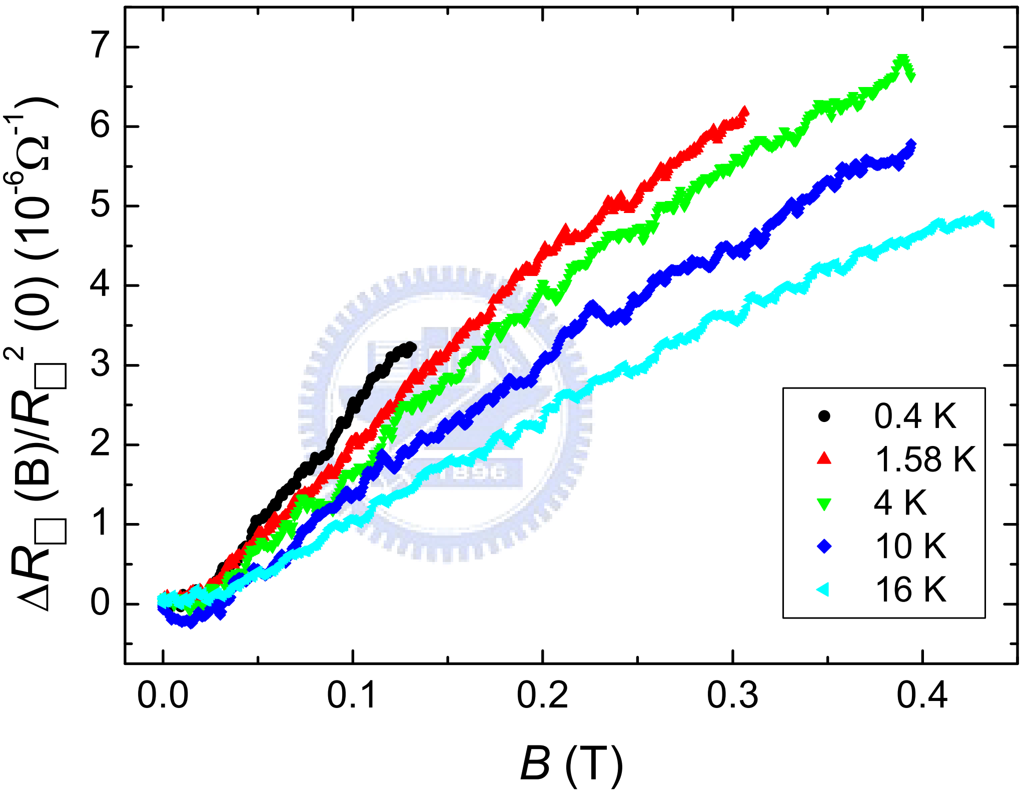

Figure 5.7: Magnetoresistances of Cu 43-1 at several temperatures.

temperature below 5 K and the increasing rates are sample dependent. The increasing rate is faster for a sample with larger sheet resistance, more disordered film. If we use the effective power law, $\tau_{ep} \propto T^{-p}$, to check the dephasing time below 5 K. We found that the p are larger for the samples with larger sheet resistances. For the sample with largest sheet resistance, the p is about 0.57±0.06. For the sample with smallest sheet resistance, the p is close to 0.

Figure 5.9 shows the extracted dephasing time of all samples. It is a long standing problem that the low temperature electron dephasing time should be infinite or finite when temperature is close to absolute zero kelvin. Our results seem indicate that it depends on the sheet resistance or the intrinsic physics appear in our system. Next, I will discuss the results in several well known physical mechanics respectively to clarify the physics.

5.3.1 Electron-Electron Inelastic Scattering Time

B. L. Altshuler(8) and co-workers(78; 79) considered the scattering of electron-electron collisions involving small energy transfer. For two-dimension case, the electron-electron relaxation time is given as:

$$\frac{1}{\tau_{ee}} = \frac{k_B T}{2\pi\nu(0)D\hbar^2} ln(\pi\nu(0)D\hbar), \tag{5.1}$$

where k_B is Boltzmann constant, D is electron diffusion constant, and T is temperature. $\nu(0) = \frac{1}{e^2 R_\Box D}$. $R_\Box$ is sheet resistance which is defined by $R_\Box = R\frac{W}{L}$. W and L mean that the width and length of samples. The electron-electron scattering rate is almost linear with $R_\Box$.

Typically, the electron-electron inelastic scattering dominates the inelastic scattering time at low temperature. The The theory predicts that $\frac{1}{\tau_{ee}} \approx 1.1 \times 10^{-9} T$ sec^{-1} for sample with $R_\Box = 30\Omega$. As we discussed above, the temperature dependent inelastic scattering times are samples dependence below 5 K. For the most disordered sample, the $\tau_\varphi \propto T^{-0.6}$. The temperature dependence of the theoretical prediction is much stronger than our measured results. Moreover The electron-electron scattering rate is 2 to 3 orders smaller than our experimental results.

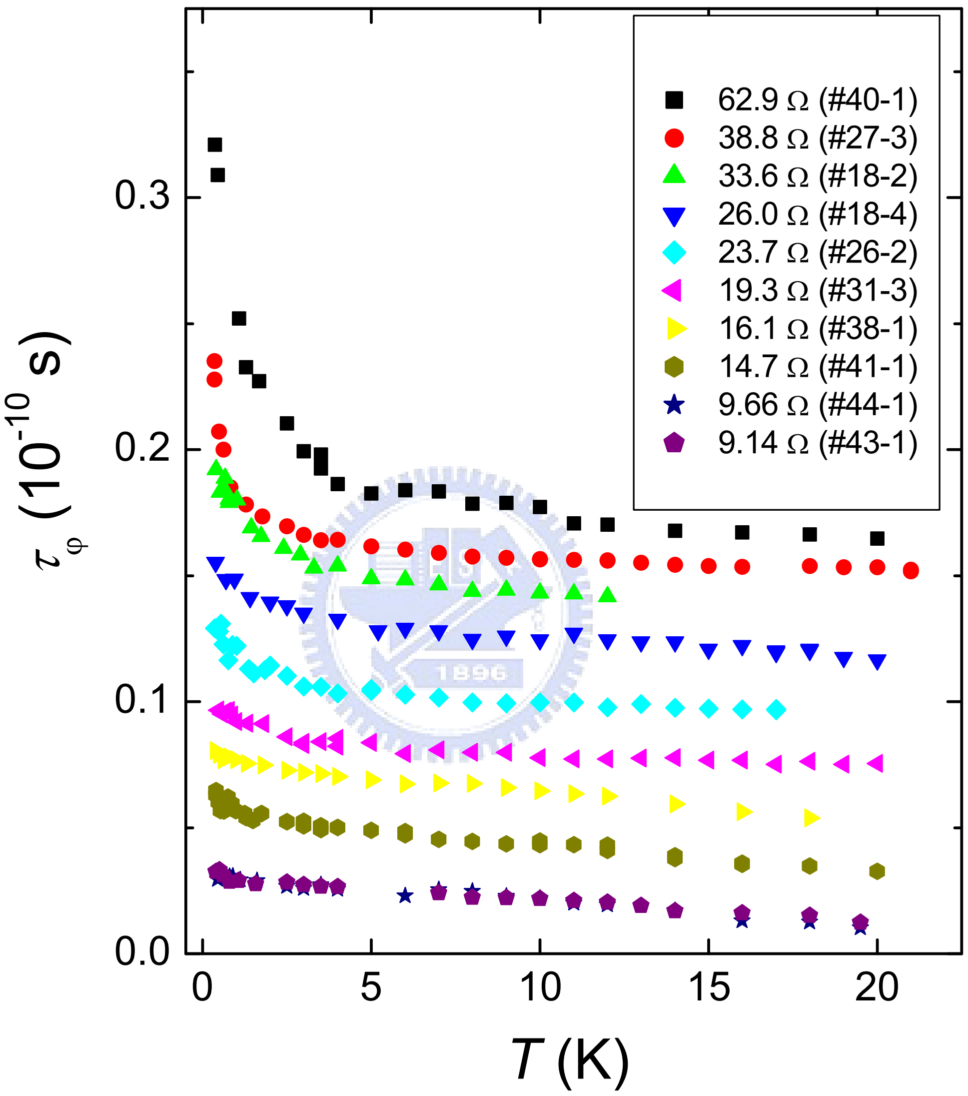

Figure 5.8: Temperature dependence of dephasing times of all samples. All of the dephasing time are shifted 2 ps one by one, except sample 43-1 and sample 44-1. The respective sheet resistances of 9 K are shown in the insect.

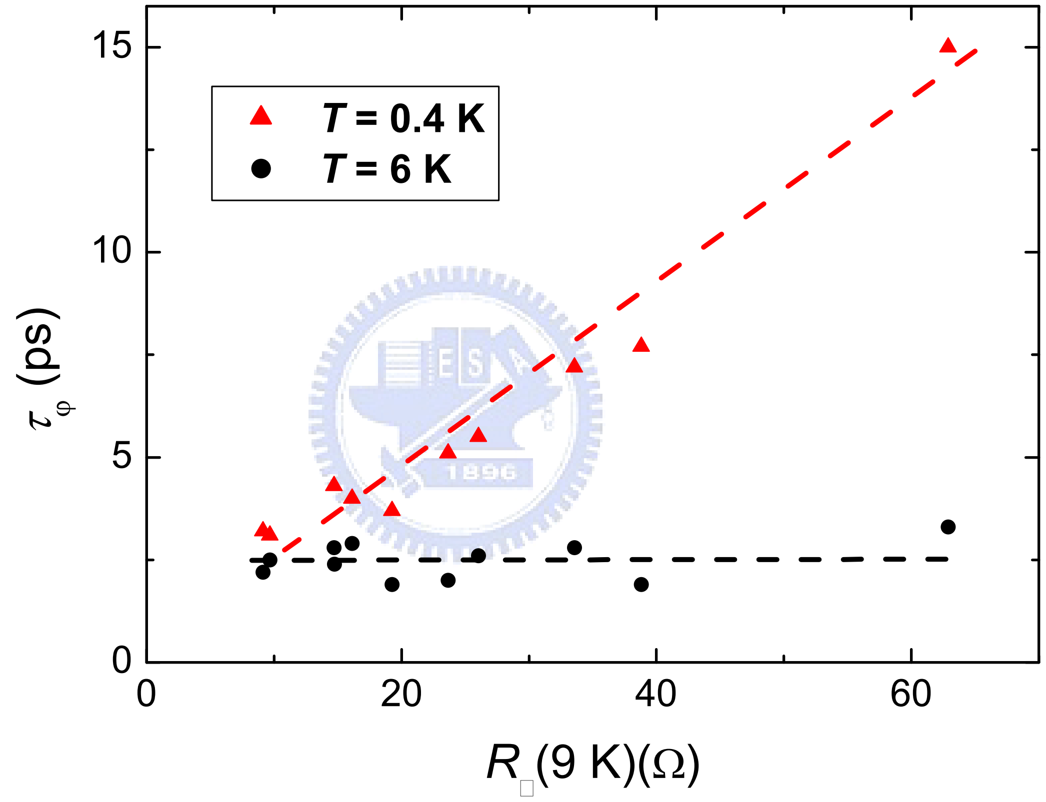

Figure 5.9: Dephasing times at 0.4 K and 6 K.

The discussions of above support that the electron-electron interaction which is often believed that dominating the low temperature inelastic scattering is not important in our system. We would neglect the electron-electron interaction in all of the following discussions.

5.3.2 Electron-Phonon Inelastic Scattering Time

The electron-phonon scattering time in the clean limit is given by

$$\frac{1}{\tau_{ep}} \approx \lambda_{ep}(\frac{k_B T^3}{\hbar \theta_D^2}) \tag{5.2}$$

where λ_{ep} is a material-dependent constant that measures the strength of the electron-phonon coupling and θ_D is the Debye temperature. In the presence of strong impurity scattering, however, the situation is less straightforward. Theoretically, the electron-phonon interaction in disordered metals has been extensively studied by a number of authors for a few decades, but different predictions were made. In particular, different values of the exponent of temperature ranging from 2 to 4 have been predicted. Recently, Sergeev and Mitin(37; 38) have generalized the Pippard-Rammer-Schmid model to take into consideration an additional "static" potential. They introduced an electron mean free path with respect to the static potential, L, in addition to the total electron mean free path, l. They found that even a relatively weak static potential drastically changes the effective electron-phonon coupling and the electron-phonon scattering rate, $1/\tau_{ep}$. Sergeev and Mitin calculated the inelastic electron scattering rate of an electron at Fermi surface due to the interaction with *longitudinal* phonon. In the dirty limit and $T \ll \theta_D$, the equation is given by

$$\frac{1}{\tau_{ep,l}} = \frac{7\pi\zeta(3)}{2}\frac{\beta_l (k_B T)^3}{\hbar^3 (k_F \nu_l)^2}(\frac{2\pi^3 (q_{T,l} l)}{35\zeta(3)} + \frac{3\pi}{7\zeta(3)(q_{T,l} L)}) \tag{5.3}$$

where $\zeta(n)$ is the Riemann zeta function. $q_T \approx k_B T/\hbar\nu_s$ is the wave number and ν_s is sound velocity. l is the mean free path. $\beta_l = (2E_F/3)^2(\nu/2\rho_i\nu_l^2)$ where ν is the electronic density of states and ρ_i is the mass density.

In the dirty limit and $T \ll \theta_D$, the inelastic scattering rate of electron at Fermi surface due to the interaction with *transverse* phonons equation is given by

$$\frac{1}{\tau_{ep,t}} = \frac{3\pi^2\beta_t(k_BT)^2}{\hbar^2(k_F\nu_t)(k_Fl)}(1-\frac{1}{L})(\frac{1}{L}+(1-\frac{1}{L})\frac{\pi^2(q_{T,t}l)^2}{10}), \tag{5.4}$$

where $\beta_t = \beta_l(\frac{\nu_l}{\nu_t})^2$ For the disordered metal case, the longitudinal phonon dominates over the transverse phonon scattering rates.

Experimentally, the temperature dependence of electron-phonon scattering time reported by various measurements on different material systems are not always in agreement with one another. Wu and Lin(29; 30; 31) study electron-phonon scattering time in superconducting Titanium alloys. Their results indicate that in the dirty limit condition, the $\tau_{ep} \propto T^{-2}$ are always observed in many experiments.

The electron-phonon inelastic scattering time is only important above 10 K that is already discussed above. We use a effective power law, $\tau = AT^{-m}$ to fit the measured high temperature inelastic time. The $m = 2$ is the best fitting between data and the power law and $A \approx 0.53 \pm 0.1$ nsec K^2. The measured electron-phonon scattering time can be given in the form

$$\tau_{ep} \approx (0.53 \pm 0.1)T^{-2} \quad \mathrm{ns\,T^{-2}}. \tag{5.5}$$

The electron-phonon scattering time is 530 ps which is 2 orders longer than the measured inelastic scattering time at 1 K. The electron-phonon scattering effect can be ignored at temperature below 10 K.

5.3.3 Nagaoka-Suhl Theory and Numerical Renormalization Group

Concerning the observation of a very weak temperature dependent inelastic scattering time, one immediately suspects that the behavior might be due to spin-spin scattering in the presence of dilute magnetic impurities in the samples. As a quick check, we found that Cu could form Kondo alloys with Cr, Mn, or Fe. The Fig. 5.1 shows that there are several ppm magnetic impurities (Cr, Mn, and Fe) in the target.

As discussed in the Chapter 3, the Kondo effect is an interaction between conduction electron and local magnetic impurity. Electron spin is flipped through the interaction with magnetic momentum of local magnetic impurity by Heisenberg coupling. There is a characteristic temperature which scales the behavior of the Kondo system. The Temperature is called Kondo temperature which means that magnetic momentum of magnetic impurity is screened by the spin of conduction electrons below the characteristic temperature. The environment would not experience the spin of magnetic impurities and the system would go back to the Fermi-liquid system again.

Two kinds of processes contribute to inelastic scattering rates. First one is single-to-single scattering which is also known as spin-flip scattering. Second one is single-to-many particle scattering, since additional electron-hole pairs can carry off phase information. As temperature approaches Kondo temperature from above, total inelastic scattering rate increases. As temperature is decreased past Kondo temperature, total inelastic scattering rate decreases, since below Kondo temperature the formation of a Kondo singlet between the impurity and its screening cloud begins to suppress spin-flip scattering. For temperature is much below the Kondo temperature, the singlet is inert with spin-flip rate $\sim e^{-T/T_K}$ and other conduction electrons experience only potential scattering (elastic scattering) off it. The system forms a Fermi-liquid and a weak residual interaction between electrons of opposite spins yields a dephasing rate $\tau^{-1} \approx (T/T_K)^2$ which vanishes as temperature approach 0 K.

In a Kondo system, the magnetic scattering rate, τ_m, is maximum at Kondo temperature, T_K. Around Kondo temperature it often appears a plateau in the inelastic scattering time.

Nagaoka and Suhl first calculated the spin-spin scattering time above Kondo temperature. They give it in the form

$$\frac{1}{\tau_m} = \frac{c_m}{\pi \hbar \nu_F} \frac{\pi^2 S(S+1)}{\pi^2 S(S+1) + ln^2(T/T_K)}, \tag{5.6}$$

where c_m is the concentration of magnetic impurities in ppm. ν_F is the density of states at Fermi level. S is the electron spin and T_K is Kondo temperature.

To unravel the intriguing inelastic scattering mechanism responsible for our measured inelastic scattering time, we carry out further quantitative analysis below. Assume that the measured inelastic scattering times between 0.3 K and 20 K are given by

$$\frac{1}{\tau_\varphi} = \frac{1}{\tau_{ep}} + \frac{1}{\tau_{ee}} + \frac{1}{\tau_Q}, \tag{5.7}$$

where τ_{ep} and τ_{ee} mean the electron-phonon and electron-electron scattering time respectively. τ_Q means others yet-to-be identified inelastic scattering time. As discussed above, the electron-electron scattering is very weak in our system and we neglect it in the following discussions. The electron-phonon scattering time is given in Eq. 5.4.

Figure 5.10 and Figure 5.11 show the extracted τ_Q of two representative samples as a function of temperature. Both two scattering rates (red solid dots) clearly reveal a maximum at characteristic temperatures which is 7 K and 5 K. The maximum scattering rates, τ_Q^M, are 45×10^{10} sec^{-1} and 30×10^{10} sec^{-1} respectively. The black solid lines are the prediction of NS theory. In the fitting, we adjusted the free parameters (T_K, c_m, and the local spin S) so it seems that the NS theory can explain the τ_Q well above the characteristic temperatures. However, inspection of the fitted values indicates that such agreement is spurious, because such good fits can only be achieved by using unrealistic values for the adjusting parameters. For examples, a local spin of $S = 0.12$ and 0.082 had to be used for the film 27-3 and 38-1 respectively. Using $S = \frac{1}{2}$ or any larger value can never reproduce our data.

Second, based on the Nagaoka-Shul (NS) expression, one can get that the spin-spin scattering time at Kondo temperature is

$$\frac{1}{\tau_m} = \frac{c_m}{\pi\hbar\nu_F}. \tag{5.8}$$

For the Cu as a host material metal, the formula can be written as

$$\frac{1}{\tau_m} \approx \frac{c_m}{0.6} ns^{-1}. \tag{5.9}$$

If we assume the measured τ_Q^M to $\tau_m(T = T_K)$, an unreasonably large value of $c_m = 200 \sim 300$ ppm will be inferred. Such a level of c_m is obviously too high to be realistic. Although accidentally formed CuO on the film surface have $S = 1$ spin

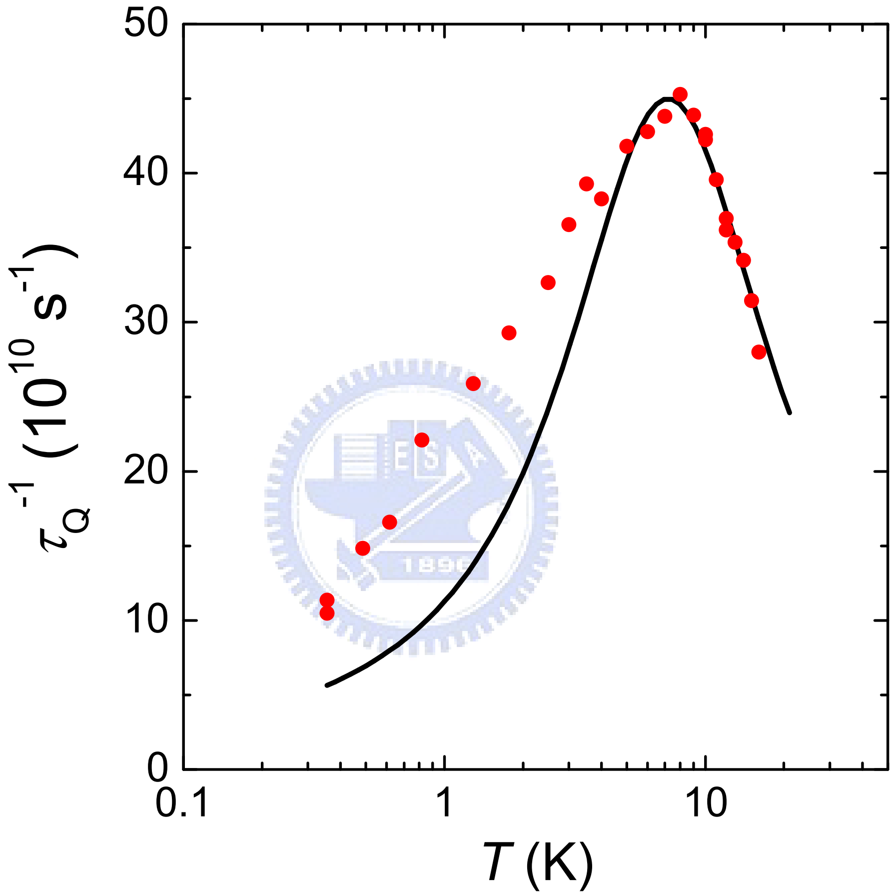

Figure 5.10: Temperature dependence of dephasing times of yet-to-be identified. The dots are the measured data of sample 27-3 and the line is the prediction of NS theory.

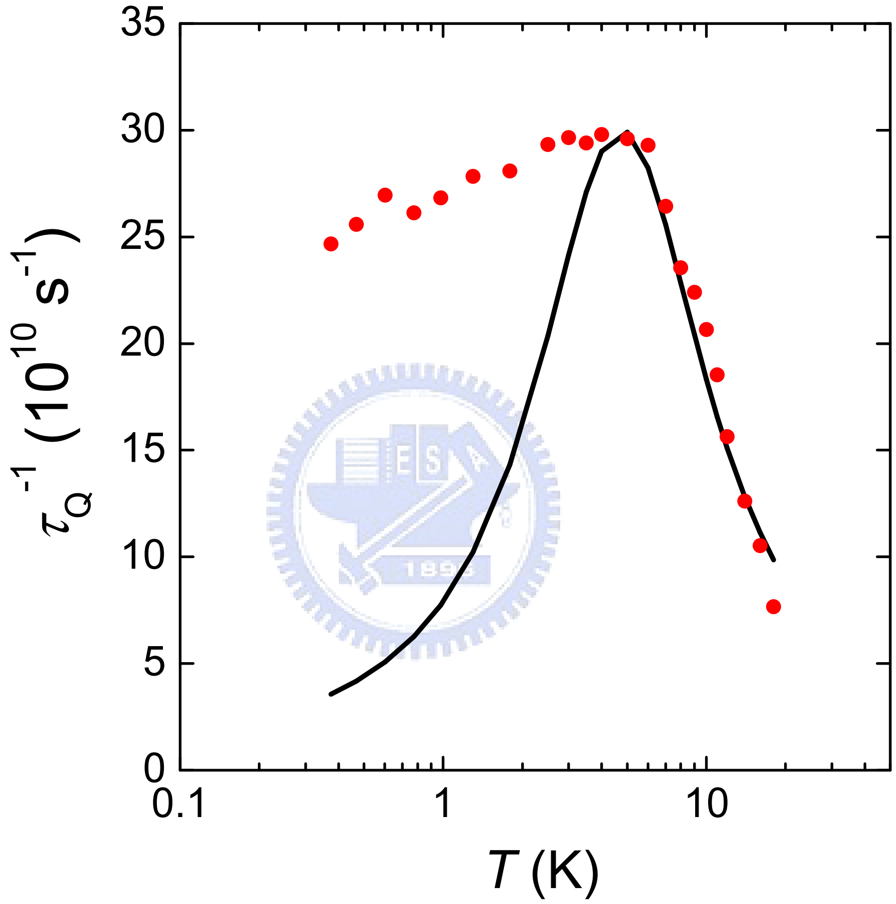

Figure 5.11: Temperature dependence of dephasing times of yet-to-be identified. The dots are the measured data of sample 38-1 and the line is the prediction of NS theory.

or some unavoidable magnetic impurities are formed during fabricated precesses, one would not expect a huge $c_m > 200$ ppm to result from such oxidation and fabricated processes.

Third, the Kondo temperature of $Cu_{95}Au_5$ (Fe 100 ppm) is 13 K, Cu (Fe) is 25 K and Au (Fe) is 0.4 K. There are no known Cu-based Kondo alloys which have values of T_K around 5 K and 7 K.

From the above three discussions, we rule out that the observed inelastic scattering, τ_Q^{-1} is not from the scattering of spin-spin (conduction electron and magnetic impurities) interaction.

The NS theory can only express the Kondo physics above Kondo temperature. Recently, G. Zarand and co-workers(80) use the numerical renormalization group (NRG) method to calculate the conduction electrons scattering by a magnetic impurity at zero temperature. The new theory can describe the physics for all temperatures, ranging from well above Kondo temperature down to zero temperature. The theory is able to predict the full energy, spin, and magnetic field dependence of the inelastic scattering cross section. They found an almost linear temperature dependence of inelastic scattering cross section below Kondo temperature and crosses over to a temperature square dependent behavior at extremely low temperature. The results show that in the case of zero magnetic fields, most of the scattering is inelastic scattering at temperature above the Kondo temperature. Decreasing the temperature, the total scattering increases and it finally saturates at slight below Kondo temperature. This behavior must be contrasted to inelastic scattering, which slowly increases as temperature decreases, has a broad maximum around Kondo temperature, then suddenly drops and vanishes. For a very low temperature region, the inelastic scattering rate is proportion to T^2 which is in agreement with Fermi liquid theory. The inelastic scattering is almost linear in temperature for $0.1T_k < T < T_K$. At temperature much larger than Kondo temperature, the inelastic scattering rate is simply dominated by spin-flip scattering and is therefore expected to scale as $\sim 1/ln^2(T_K/T)$. The theory emphasizes that the NS theory is appropriate only for $T \gg T_K$.

Micklitz and co-workers(81; 82; 83) calculated new theories for spin $S = \frac{1}{2}$ impurities and have confirmed that the $\tau_m^{-1} \propto ln^{-2}(T/T_K)$ for $T \gg T_K$ and the scattering rate τ_m^{-1} is maximum at $T = T_K$. The inelastic scattering rate is linear with temperature for $0.1T_K < T < T_K$. While temperature is much lower than Kondo temperature the $\tau_m^{-1} \sim T^2$ which is consistent with the prediction of Fermi-liquid theory. The prediction is quite consistent with the prediction of G. Zarand. One distinct point is that their corrected peak scattering rate is about 8% lower than the NS prediction. So the estimation of concentration of magnetic impurities, c_m, discussed above will not be substantially altered even if one applies the new theory. It is noteworthy that as shown in Fig. 5.10 and Fig. 5.11, the measured inelastic scattering rates are larger then prediction of NS theory which is also larger than predictions by G. Zarand and Micklitz.

Recently, N. O. Birge(40) and C. Bäuerle(84; 85; 86) measured inelastic scattering time of quasi-one-dimension gold wires containing magnetic impurities which are added into gold wires by ion implant method. Their results support the predictions of the NRG theories. It is noteworthy that the behavior of inelastic scattering is mainly dominated by the concentration of magnetic impurities below the Kondo temperature. As we discuss above, the increasing rates of measured inelastic scattering time below Kondo temperature is sample dependent. For a sample with higher level of disorder the increasing rate is faster. The fastest increasing rate of inelastic scattering time is about $T^{-0.5}$ in our measured results. The temperature dependent of measured inelastic scattering time is much weaker than the prediction of NRG theory. As shown in Fig. 5.9, the measured inelastic scattering times are about 8 times difference for strongest and weakest disordered samples at 0.4 K. On the other hand, based on the prediction of NRG theory the inelastic scattering rate is proportion to concentration of magnetic impurities. One would not expect almost 1 order difference of magnetic impurities between different films which are deposited by using the same source target and the same fabricating processes.

5.4 Low Temperature Resistance

Figure 5.12 shows measured resistance of a representative sample as a function of temperature from 300 K down to 0.3 K. The high temperature resistance is mainly dominated by electron-phonon scattering. It can be described by the Bloch-Grüneisen equaiton.

$$\rho_{BG}(T) = \beta_{BG} T (\frac{T}{\theta_D})^4 \int_0^{\theta_D/T} \frac{x^5 dx}{(e^x - 1)(1 - e^{-x})}. \tag{5.10}$$

where β_{BG} is electron-phonon coupling constant and θ_D is the Debye temperature. The equation predicts that the resistance decreases as temperature decreasing, because of the decreasing of phonon. The inset of the Fig. 5.12 shows the measured resistance between 20 K to 0.3 K. Clearly, the resistance increases as temperature decreasing and the resistance rise is logarithmic below 5 K. The logarithmic rise might come from several quantum transports which will be discussed below.

The Fig. 5.13 shows the resistances as a function of temperature of four representative samples with different levels of disorder. It shows that all of the resistances are logarithmic increase as temperature decreasing and the increasing is samples dependent. For a sample with higher levels of disorder, the increasing is larger.

5.4.1 Kondo Effect

As discussed in Chapter 3, the Kondo effect is an interaction between spin of conduction electron and magnetic moment of local magnetic impurities. The correction to resistance is $\Delta R_K(T) \propto -B_K ln(T/T_K)$, where B_K dependent on the coupling strength of the *s*-shell electron and *d*-shell electron. The correction is very sensitive to the external magnetic field. The external magnetic field reduces the correction to resistance. In order to identify the physics of the behavior, high magnetic field and low temperature measurement is necessary.

Figure 5.14 shows the temperature dependent resistance of 0 T and 9 T. Both resistances are logarithmic increase as temperature decreasing from 1 K down to 50 mK. The increasing rate is insensitivity to high magnetic fields. The increasing rate of 9 T is about 5% smaller than the increasing rate of 0 T. It indicates that the dominating mechanics are not spin-based. The slope should be obviously suppressed in the presence of high magnetic field, if the Kondo effect is real important in the system. Second, assume that the concentration of the magnetic impurities is as high as the estimation, 200 ppm $\sim$ 300 ppm, from the theoretical prediction, the interaction between local magnetic impurities should be strong. The RKKY interaction between the randomly distributed impurity spins compete

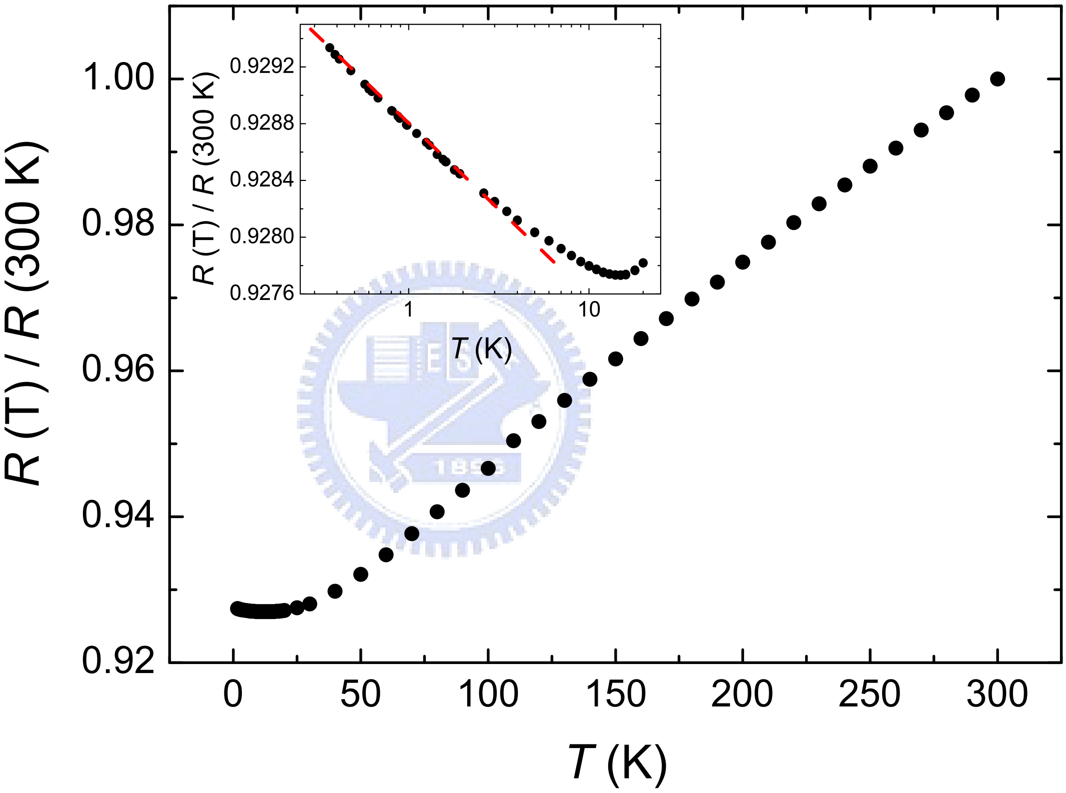

Figure 5.12: Temperature dependent resistance of samples 18-4.

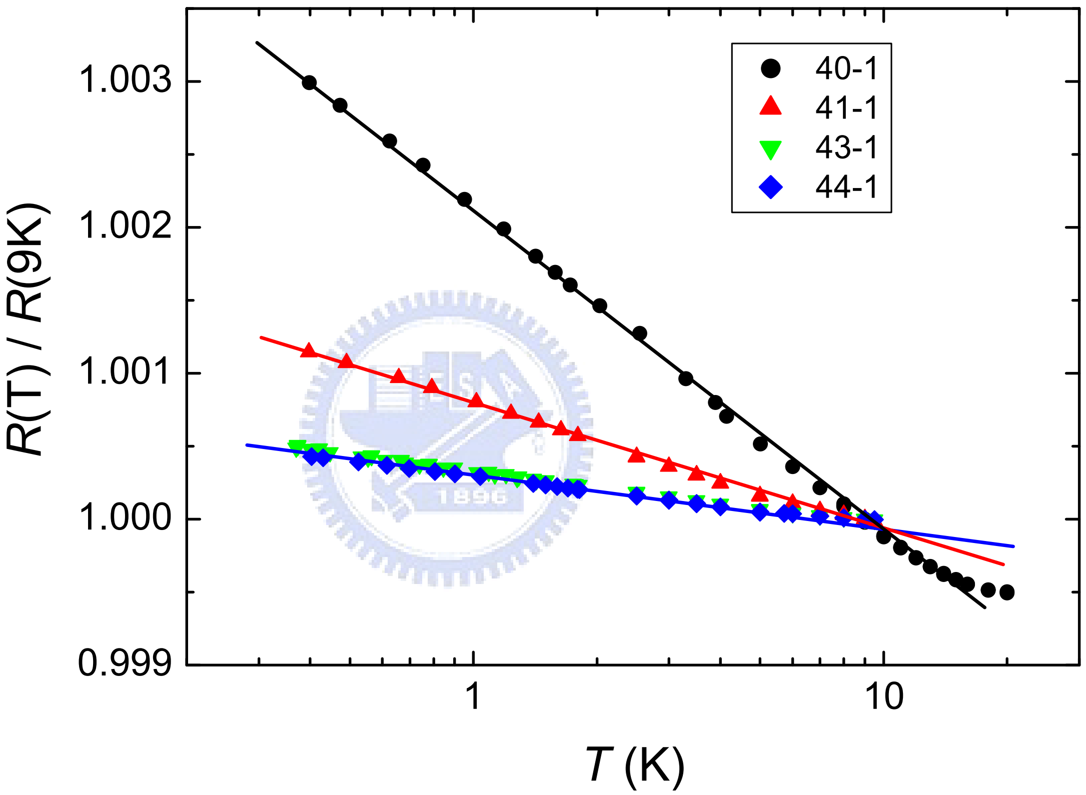

Figure 5.13: Resistances of four samples as a function of temperature. All of the dependence are logarithmic dependence.

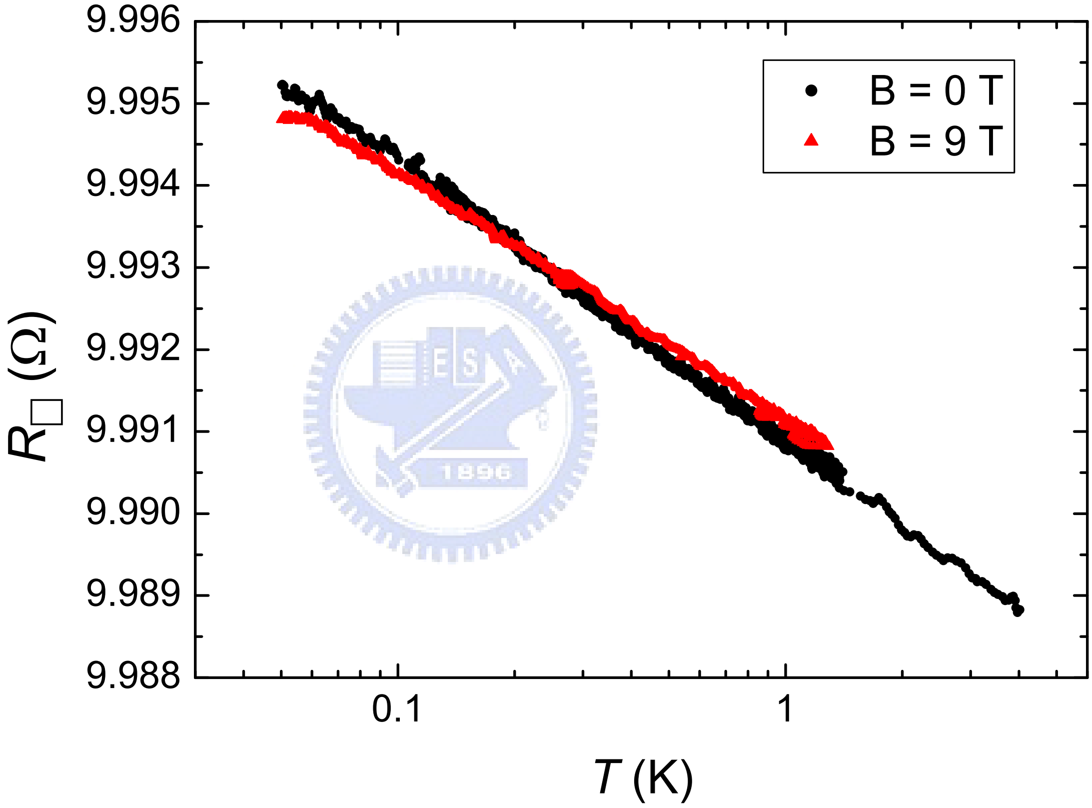

Figure 5.14: Temperature dependent resistance of sample 44-1 at 0 T and 9 T.

with the Kondo effect and causes a freezing of the impurity spins into a disordered configuration call a spin glass. This is reflected by the appearance of a typical broad maximum in resistance since the spin scattering rate again decreases at the lowest temperature due to the freezing process. However, as shown in Fig. 5.14, there is definitely no sign of a saturated resistance signifying the presence of the Kondo effect, and there is no maximum peak of resistance signifying the presence of the spin-glass effect. It indicates that the concentration of the magnetic impurities are not as high as we estimate from NS theory or the magnetic impurity scattering is not important at all in our system. All of the evidences suggest that the magnetic scattering could not be the dominating mechanic in our systems.

5.4.2 Weak Localization

As we discussed in chapter 3. The correction of weak localization to resistance is dimensional dependence. The correction is logarithmic increase in two-dimension system which means the thickness of the samples is thinner than electron inelastic scattering length, l_φ. The l_φ is usually about submicro meter which is larger than the thickness of samples. The correction of weak localization to resistance is given as

$$\frac{\Delta R_\square(T)}{R_\square^2(T_0)} = -\frac{(\alpha P + 1 - \frac{3}{4}F)e^2}{2\pi^2\hbar} ln(T/T_0), \tag{5.11}$$

where the P is dependent on the inelastic scattering time and the αP is close to 1. $1 - \frac{3}{4}F$ is the correction of electron-electron interaction effect and F is the screening factor. For a full screened system, F is equal to 1. In the opposite limit, full unscreened system, the F is close to 0. For disordered metal films in the limit of strong spin-orbit interaction, the screening factor is small and the electron-electron interaction effect dominates the resistance rise while the weak localization contribution is negligibly small. For all films, we obtained $\alpha P + 1 - \frac{3}{4}F = 1.33 \pm 0.13$. This is systematically larger than prediction of theory and strongly implies that there must be extra mechanism which also contributes to the logarithmic increase in temperature.

To further illuminate this anomalous logarithmic increasing resistances, we have also made a few thick films (compare with inelastic scattering length) from the same sputtering under similar deposition conditions and measured the resistances. Figure 5.15 shows the measured resistance as a function of temperature at different magnetic fields which is up to 15 T. The insect shows that the logarithmic increase is wide range from above 10 K. There are two distinct points. First one is that all the resistances are logarithmic rise from 10 K down to 30 mK for all applied magnetic fields. Second one is that the resistances are insensitive to high magnetic fields.

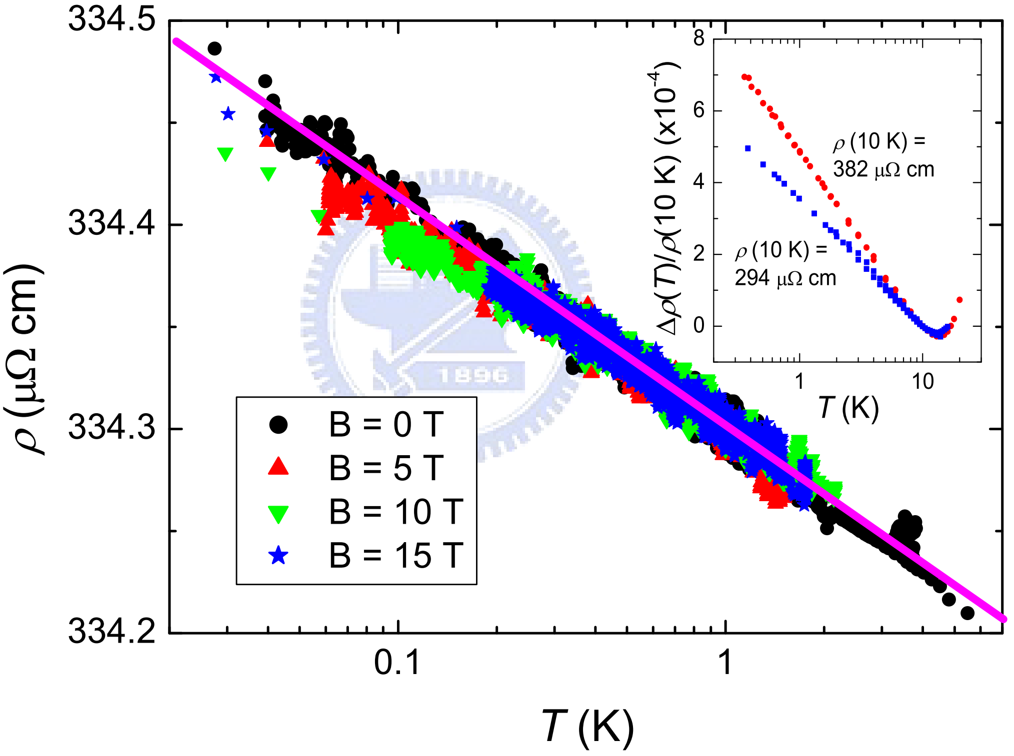

Figure 5.15: Temperature dependent resistance of thick sample at 0 T, 5 T, 10 T, and 15 T.

For a three-dimension sample, the weak localization theory predicts that the correction of temperature dependent resistance is $-\sqrt{T}$. The measured results strongly show the lnT behavior for a wide range. It indicates that other mechanics dominate over the three dimensions electron-electron interaction effect. Also the resistance is also insensitivity to the high magnetic fields.

5.5 Two-Level System

It has been reported that scattering of electrons off two-level system can cause a logarithmic increase. R. W. Cochrane and co-workers(75) calculated a mechanism of structure origin, due to scattering by two-level system. They obtain an analytic expression of the following form:

$$R = R_0 - Aln(T^2 + \Delta^2), \tag{5.12}$$

where Δ is the energy difference between the two atomic tunneling states and A is a constant depending on the number of contributing sites and the strength of the Coulomb interaction. In contrast to the Kondo effect, it has been reported that the resistance due to two-level system scattering is very insensitivity to the external magnetic field. Recent observations in structurally disordered diamagnet ThAsSe show that the electrical resistance displays a logarithmic correction for a wide range in temperature, which is not affected by strong magnetic field up to 16 T.(62; 68) Our observations of temperature dependent resistances which are shown in Fig. 5.14 and Fig. 5.15 are consistent with both experimental and theoretical reports and also support the possibility of two-level system in our system.

Theoretically, A. Zawadowski and co-workers(48) considered the dephasing in metals by two-level system in two-channel Kondo region. In the two-channel Kondo regime, the single-to-single-particle and single-to-many-particle scattering rates are known to respectively decrease and increase with decreasing temperature. The single-to-single-particle scattering rates is proportional to $T^{1/2}$. It is approaching to 0 as temperature is closing to 0. The key point of dephasing is that the single-to-many-particle scattering would cause dephasing, so one can take the single-to-many-particle scattering time as the total dephasing time a low temperature. The theory predicts that there is a broad peak around Kondo temperature. Adding to a power-law decay due to other sources of dephasing (electron-electron interaction or electron-phonon interaction), the total dephasing rates would have a broad shoulder around Kondo temperature that is the same as we observe in the experiments.

Y. M. Galperin(87) calculated the dephasing time using a model based on tunneling states of dynamical structure defeats. He predicts that an inelastic scattering time possessing a very weak temperature dependence in a certain temperature interval and then crossing over to a slow increase with decreasing temperature. Based on the theory, the dephasing rates is proportional to diffusion constant.

Experimentally, Lin and co-workers measured low temperature electron dephasing time in a series of highly disordered three-dimension AuPd films.(44) For all films, saturation of dephasing times, τ_φ^0, are observed below about several K. The saturating temperature is sample dependent and ranges from 0.005 ns to 0.5 ns. Particularly, the τ_φ^0 is proportional to diffusion constant. On the other hand, Z. Ovadyahu and co-workers(64; 65; 66) measured resistances and electron dephasing times in two dimensional In_2O_{3-x} and Au-doped In_2O_{3-x}. The resistances are logarithmical increase as temperature decreasing. The dephasing times are inversely proportional to temperature, except there is a plateau (weak temperature dependent) around several K. Particularly, the plateaus range and width depend on the concentration of doped Au. For an un-doped In_2O_{3-x} films, no plateau is observed in the reports. It indicates that the appearance of the plateau comes from the breaking of the structural symmetry, a mimic of two-level system.

Until now, we discussed temperature dependent resistance at several high magnetic fields and low temperature electron inelastic scattering time for a series of films with different levels of disorder. The resistances are logarithmic rise from above 10 K down to 30 mK and the behavior is dimensional independent (independent of thickness of films). Particularly, the temperature dependence is insensitivity to magnetic fields up to 15 T. Many theorists predicted a plateau (weak temperature dependent) of inelastic scattering time, that is the same as our results, around Kondo temperature in two-level system. Based on the above discussions, we strongly convince that instead of the spin-flip (Kondo) effect, which is always inferred to the effect of observed saturation of dephasing time, the two-level system dominates the physical behavior of the system.(88)

Recently, Imry and co-workers consider a two-level model with loosely bound heavy impurities. In the tunneling model Imry and co-workers take the scatter to reside in a double-minimum potential. The minima are separated by a vector $\vec{b}$, the tunneling matrix element between the two minima is Ω_0, and their energy separation is $2B$. The separation 2Δ between the ground state and excited state in the well, respectively, is given by

$$2\Delta = 2\sqrt{\Omega_0^2 + B^2}. \tag{5.13}$$

The above labelling of the states reflects their spatial symmetry for $B = 0$. First, they assume that all of the energy splitting of two local minimum potential are uniform and the inelastic scattering is given by

$$\frac{1}{\tau_{in}} = \frac{4(\alpha\beta)^2 n_s \nu_F \sigma_0}{cosh^2(\Delta/(k_B T))}, \tag{5.14}$$

where n_s isthe concentration of the soft impurities. α and β are the normalized weights in the two wells. $\alpha\beta = \Omega_0/(2\Delta)$. The combination $2|\alpha\beta|$ is a symmetry parameter, ranging from unity for a symmetric well ($B = 0$) to zero for a very asymmetric one.

The parameters of the various two-level system within the system, are often distributed. Reasonable distributions are a uniform distribution for B in the range $0 \leq B \leq B_{max}$, and a $1/\Omega_0$ distribution for Ω_0, between Ω_{min} and Ω_{max}. The latter distribution follows by taking Ω_0 to be the exponential of a large negative, uniformly distributed quantity in the corresponding range. One generally expects $\Omega_{max} \ll B_{max}$. The combined distribution function reads

$$P(B, \Omega_0) = \frac{1}{\Omega_0 B_{max} ln(\Omega_{max}/\Omega_{min})}. \tag{5.15}$$

one averages over the distribution of Eq. 5.15, and the inelastic scattering is given by

$$\begin{gathered}
\tau_{in} \propto e^{-2\Omega_{min}/(k_B T)} \quad for \quad k_B T \ll \Omega_{min}; \\
\tau_{in} \propto T \quad for \quad \Omega_{min} \ll k_B T \ll \Omega_{max}; \\
\tau_{in} \propto const \quad for \quad \Omega_{max} \ll k_B T.
\end{gathered} \tag{5.16}$$

Recently, our results catch some theorists' attentions. B. Dóra and M. Gulácsi study a nonuniversal contribution to the dephasing rate of conduction electrons due to local vibrational modes.(89) The inelastic scattering rate exhibits strong oscillations at frequencies comparable to the phonon excitation energy, and then saturates to a finite, coupling dependent value. At the extreme strong coupling limit, close to the complete softening of the phonons, the s-matrix vanishes and the inelastic cross section reaches its maximal value. This phonon mediated scattering mechanism is expected to be rather insensitive to the applied magnetic field, in contrast to Kondo-type impurities, and can contribute to the dephasing time in certain alloys containing dynamical defects.

However, the microscopic parameter, the level of symmetry of two wells, Δ, B, and Ω are difficult to know. The more detail discussions of the measured results need further works of theory.

After comparing with all existence theories, it indicates that our system is dominated only by the dynamic structure defeat daphasing. However, the fabricating processes and the microstructures of sample strongly affect the behaviors of the inelastic scattering. Only a few works on the effect, many of ideas are still not clear. For example, the dependence of increasing rate and sheet resistance and an explicit way to define the levels of disorder, the number of two-level system. At this field, we have to study more to clear the physics in the future.

Part2:
Spin Transport in Vertical Double Quantum Dots

Chapter 6

Introduction to Quantum Information and Quantum Dot

Civilization has always advanced as people discovered new ways of exploiting various physical resources, such as materials, forces, and energies. In the twentieth century, information was added to the list when the invention of computers allowed complex information processing to be performed outside human brains. The history of information technology has involved a sequence of changes from one type of physical realization to another, from gears to relays to valves to transistors to integrated circuits and so on. Now, developments of quantum information processing have reached the stage where one bit of information can be encoded in quantum systems, for example using two different polarizations of light, or two different electronic states of an atom. Matter on this scale obeys the laws of quantum mechanics. In a quantum computer, the information is loaded as a string of quantum bits (qubits). A qubit in a quantum object, for example, an atom (an ion) which can occupy different quantum states. Two of these states are used to store digital information. An atom in the ground state corresponds to the value ”0” of the qubit. The same atom in the excited state corresponds to the value ”1” of this qubit.

The main advantage of the quantum computer is not connected with the density of qubits. The difference is that quantum physics allows one to operate with a superposition of quantum states. For one atom, one can produce an infinite number of superpositional states using just two basic quantum states, which correspond to "0" and "1". For example, if two states have energies, E_0 and E_1. Utilization of superpositional states allows one to work with quantum states which simultaneously represent many different numbers. This is call "quantum parallelism". It can take thousands and thousands years for the most powerful digital computers to find the prime factors of a 200-digital number. A quantum computer can operate simultaneously on many numbers and only the few desired numbers are reserved. The undesired numbers are removed by destructive interference.

Entanglement is the other one of the distinct properties of quantum system that makes quantum information processing so different from classical information technology. Quantum entanglement is a quantum mechanical phenomenon in which the quantum states of two or more objects are somehow linked together so intimately that one object cannot be adequately described without full mention of its counterpart X even though the individual objects may be spatially separated. Entanglement makes possible quantum teleportation.(90; 91)

Until now, there are many systems can operate as a qubit, such as: electrons on the surface of liquid helium,(92) Josephson Junction,(93; 94) nuclear spin resonance,(95) electron spin in semiconductor quantum dot.(96; 97; 98; 99) In my work, I focus on the electron spin in semiconductor quantum dot(s). Effects of quantum confinement on the electronic properties of semiconductor heterostructures are well known prior to the study of quantum dots. Growth techniques such as molecular beam epitaxy, allows fabrication of quantum wells and heterostructure with energy levels that are quantized along the growth direction. For proper choice of growth parameters, the electrons are fully confined in the z-direction. The electron motion is free in the x-y plane. This forms a two dimensional electron gas. Quantum dots are emerged when this growth technology is combined with electron-beam lithography to produce confinement in all three directions.

Many of works have done to check the basic physics and properties of quantum dots in different systems.(100; 101; 102) Some of results are using as appliances, such as spin filters. Recently, spin states in quantum dots is expected to be a qubits and many of works are performed in progress. For example, Marcus(103; 104) and Tarucha(105) manipulate the electron spins by the technique of ESR. Kono and co-workers(92) operate the electrons on the surface of liquid helium by microwave. Following, I would discuss some of my works on the electron tunneling in semiconductor vertical double quantum dots in the years.

Chapter 7

Theory and Background

7.1 Quantized Charge Tunneling

The circumstances under Coulomb charging are important. First we consider the electronic properties of a small conductor depicted in Fig. 7.1 which is coupled to three terminals. Particle exchange can occur with only two of the terminals, as indicated by the arrows. These source and drain terminals connect the small conductor to macroscopic current and voltage meters. The third terminal provides an electrostatic or capacitive coupling and can be used as a gate electrode. If we first assume that there is no coupling to the source and drain contacts, then the small conductor acts as an island for electrons. The number of electrons on this island is an integer.

When tunneling occurs, the charge on the island suddenly changes by the quantized amount e. The associated change in the Coulomb energy is conveniently expressed in terms of the capacitance C of the island. An extra charge e changes the electrostatic potential be the charging energy $E_c = e^2/C$. This charging energy becomes important when it exceeds the thermal energy k_BT. A second requirement is that the barriers are sufficiently opaque such that the electrons are located either in the source, in the drain, or on the island. This requirements translates to a lower bound for the tunnel resistances R_t of the barriers. To see this, consider the typical time to charge or discharge the island $\Delta t = R_tC$. Furthermore, for the charge to be quantized, the energy uncertainty ΔE must be much smaller than the charging energy. The Heisenberg uncertainty relation

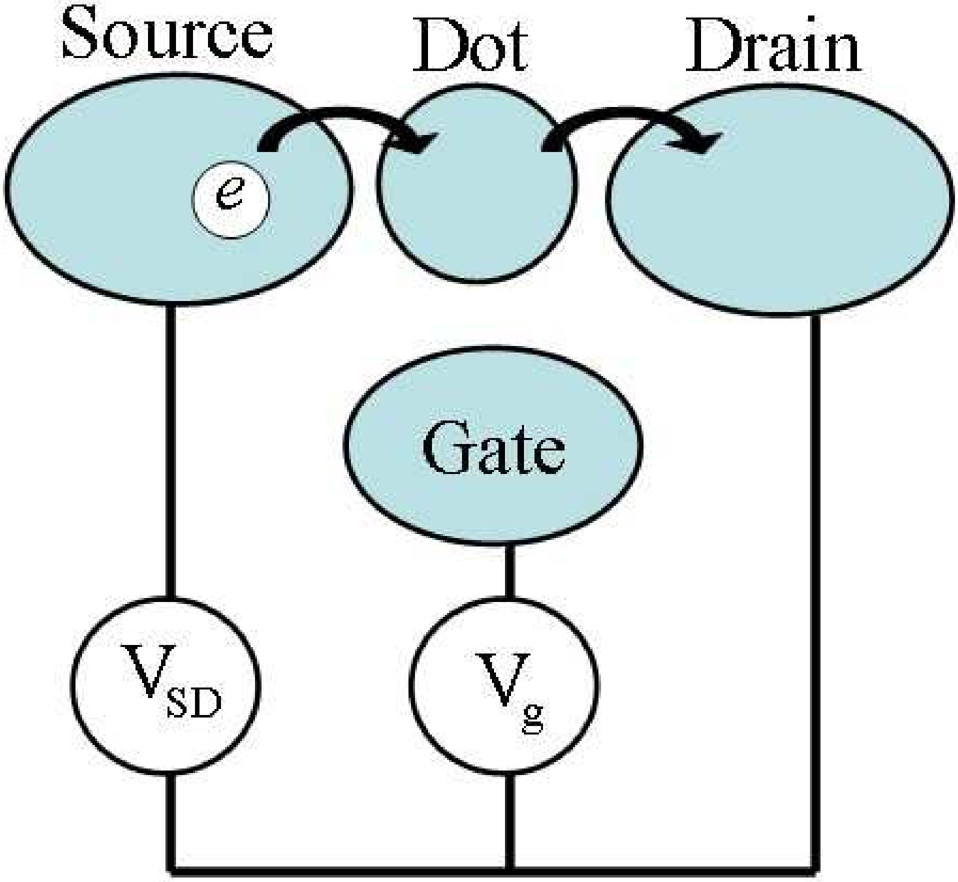

Figure 7.1: Schema of a quantum dot.

$\Delta E \Delta t = (e^2/C)R_tC \geq h$ then implies that R_t should be much larger than the resistance quantum $h/e^2 = 25.8$ kΩ. To summarize, the two conditions for observing effects to the discrete nature of charge are

$$R_t \gg h/e^2, \tag{7.1}$$

$$e^2/C \gg k_BT. \tag{7.2}$$

The first criterion can be met be weakly coupling the dot to the source and drain leads. The second criterion can be met by making the dot sufficiently small.(106)

While the tunneling of a single charge changes the electrostatic energy of the island by a discrete values, a voltage V_g applied to the gate can change the island's electrostatic energy in a continuous manner. In terms of charge, tunneling changes island's charge by an integer while the gate voltage induces an effective continuous charge $q = C_gV_g$ that represents, in some sense, the charge that the dot would like to have. The charge is continuous even on the scale of the elementary charge e. If we sweep V_g the build up of the induced charges onto the dot. This competition between continuously induced charge and discrete compensation leads to so-called Coulomb oscillations in a measurement of the current, as a function of gate voltage at a fixed source drain voltage.

7.2 Two Dimensional Electron Gas

In the section we will briefly introduce basic properties of a two dimensional electron gas (2DEG) in a GaAs/AlGaAs heterostructure. On the GaAs substrate a layer of typically 100nm AlGaAs in grown. Somewhere halfway in the AlGaAs layer there is a thin layer where the Ga atoms are replaced by Si donor atoms. With a proper amount of Si one finds that at low temperature the only mobile electrons are located at the GaAs/AlGaAs interface. These free electrons are attracted by the GaAs since they can lower their energy in this smaller band gap material. They are also held as close as possible to their ionized Si$^+$ donors and thus they form a thin conducting layer near the GaAs/AlGaAs interface.

7.3 Two Dimensional Harmonic Oscillator

In experimentally realized dots, the motion in the z direction is always frozen out into the lowest electric subband. Since the corresponding extent of the wave function is much less than the one in the x-y plane, we can treat the dots in the two-dimensional limit of thin disks. For quantum dots, a harmonic oscillator is a very good approximation to describe the confinement of the electrons.

The familiar spectrum of a one-dimensional harmonic oscillator $E_n = (n + \frac{1}{2})\hbar\omega$ becomes $E_{n,l} = (2n + |l| + 1)\hbar\omega$ in two dimensions. Here $n(= 0, 1, 2, ...)$ is the radial quantum number, $l(= 0, \pm 1, \pm 2, ...)$ is the angular momentum quantum number of the oscillator and ω is the oscillator frequency.

The electronic states are expected to be significantly modified by a magnetic field, B, applied perpendicular to the plane of the dot. The eigenenergies $E_{n,l}$ as a function of B can be solved analytically for a two dimensional parabolic potential $V(r) = \frac{1}{2}m^*\omega_0^2 r^2$

$$E_{n,l}(B) = (2n + |l| + 1)\hbar\sqrt[2]{\frac{1}{4}\omega_c^2 + \omega_0^2} - \frac{1}{2}l\hbar\omega_c, \tag{7.3}$$

where $\hbar\omega_0$ is the electrostatic confinement energy, $\hbar\omega_c = \frac{\hbar eB}{m^*}$ is the cyclotron energy and $m^* = 0.067m_e$ is the effective mass in GaAs. $\hbar\omega_c = 1.7$ meV at 1 T.(107; 108)

Figure 7.2 shows the single-particle energy as a function of magnetic fields for $\hbar\omega_0 = 3$ meV. It shows that the orbital degeneracies at $B = 0$ T are lifted in the presence of magnetic fields. As magnetic field is initially increased from 0 T, a single-particle state with a positive or negative l shifts to lower or higher energy, respectively. At $B = 0$ the lowest energy state has $(n, l) = (0, 0)$ and is two-fold spin degenerate. The next state has a double orbital degenracy $E_{0,1} = E_{0,-1}$. We denote these degenerate states of the second shell. Including spin degenracy this shell can contain up to 4 electrons, so it will be filled when there are 6 electrons on the dots. In the third shell states with quantum numbers (1,0), (0,2), (0, -2) are degenerate. With spin this shell may contain up to 6 electrons, leading to the magic number 12. Note that the degeneracy of the (1,0) state with the (0,2) and (0,-2) states is lifted if the potential has a non-parabolic component.(109)

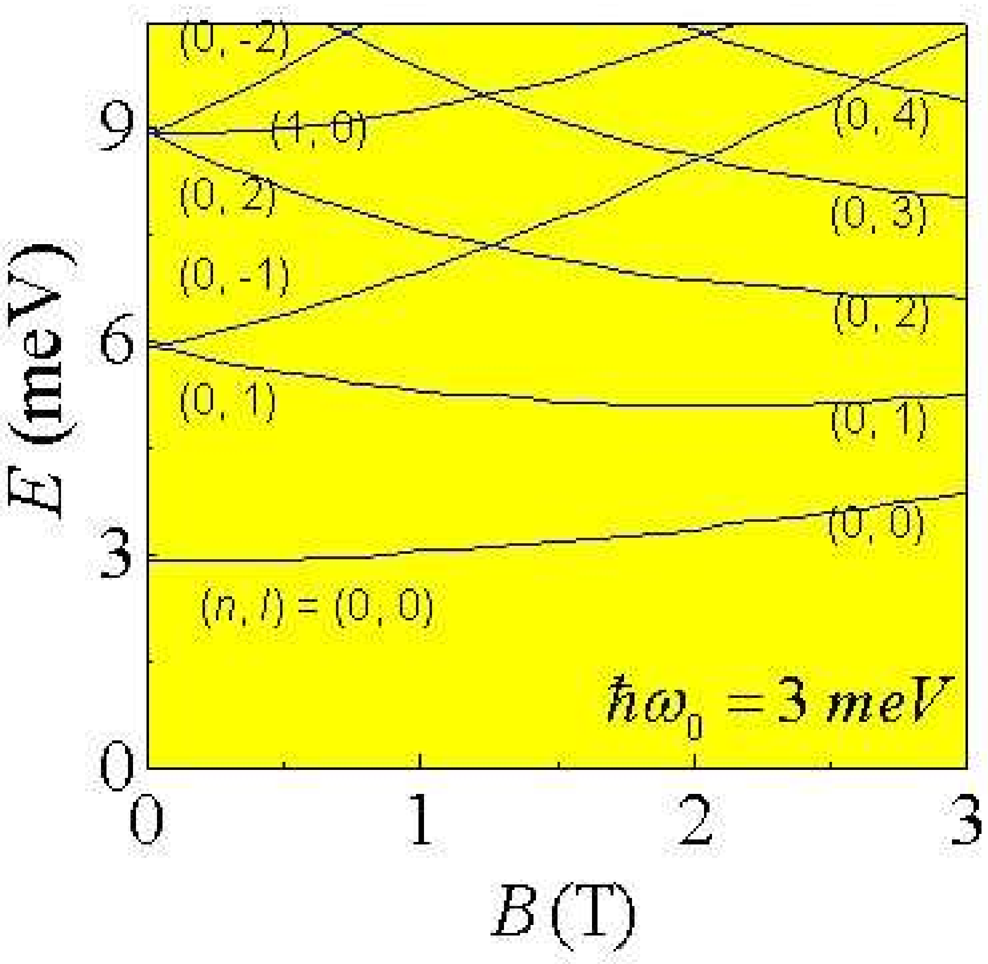

Figure 7.2: Calculated single-particle energy as a function of magnetic fields for a parabolic potential with $\hbar\omega_0 = 3$ meV.

7.4 Constant Interaction Model

Here, we introduce the constant interaction, CI, model that describes the electronic states of the dot.(99; 110) The CI model is based on two important assumptions. First, the Coulomb interactions of an electron on the dot with its environment and with other electrons on the dot are parametrized by a constant capacitance C. Second, the discrete energy spectrum of a single particle on the dot is not affected by the interactions. The CI model approximates the total energy $U(N)$ of an N electrons dot by

$$U(N) = \frac{(e(N - N_0) - C_g V_g)^2}{2C} + \sum_N E_{n,l}(B) \tag{7.4}$$

where N_0 is the number of electrons on the dot at zero gate voltage. The term $C_g V_g$ is a continuous variable and represents the charge that is induced on the dot by the gate voltage V_g through the capacitance C_g. The total capacitance between the dot and the source, drain, and gate is $C = C_s + C_d + C_g$. The last term is a sum over Eq. 7.3 .

The electro-chemical potential of the dot is defined as $\mu_{dot} = U(N) - U(N-1)$. Electrons can flow from source to drain when μ_{dot} is between the electro-chemical potentials, μ_{source} and μ_{drain}, of the leads. From eq. 7.4 we get the electro-chemical potential of the dot

$$\mu_{dot}(N) = (N - N_0 - \frac{1}{2})E_c - e\frac{C_g}{C}V_g + E_N \tag{7.5}$$

The addition energy is given by

$$\Delta\mu(N) = \mu_{dot}(N+1) - \mu_{dot}(N) = E_c + E_{N+1} - E_N \tag{7.6}$$

with E_N the topmost filled single-particle state for an N electron dot.

The electro-chemical potential is changed linearly by the gate voltage with a proportionality factor $\alpha = e\frac{C_g}{C}$. This α factor also relates the peak spacing to the addition energy. We define the spacing between the N^{th} Coulomb peak at V_g^N and the next peak at V_g^{N+1} as $\Delta V_g(N+1) = V_g^{N+1} - V_g^N$. The addition energy follows from $\Delta\mu(N) = \alpha\Delta V_g(N)$.

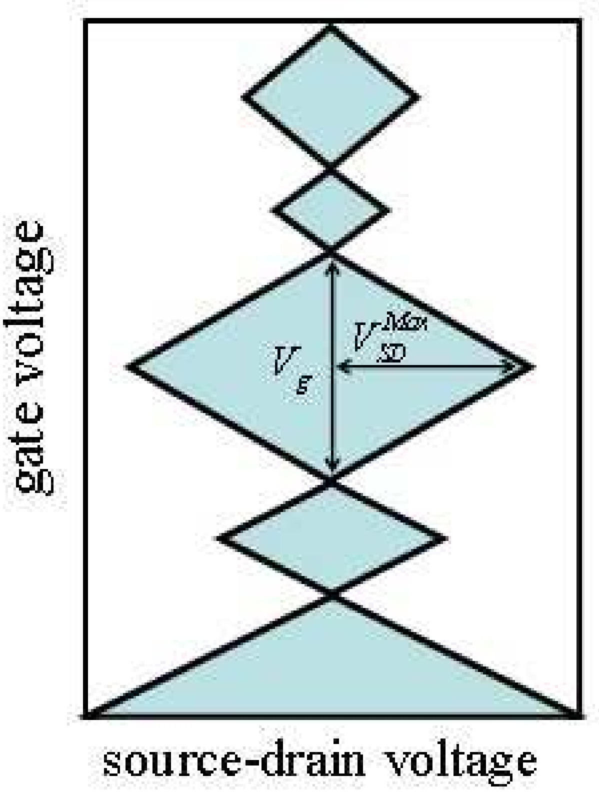

Figure 7.3: determine the α factor from the slope of the sides of the Coulomb diamond.

Figure 7.3 shows how to determine the α factor from the slope of the sides of the Coulomb diamond: $\alpha = |e\frac{V_{SD}^{Max}}{\Delta V_g}|$. Since the gate voltage changes the dot area, the α factor changes with N.

7.5 Low Source-Drain Voltage Region

For a quantum dot system in equilibrium, electron transport is only possible when a level corresponding to transport between successive ground states is in the bias window, i.e. $\mu_s \geq \mu(N) \geq \mu_D$ for at least one value of N. If this condition is not met, the number of electrons on the dot remains fixed and no current flows through the dot. This is known as Coulomb blockade. An example of such a level alignment is shown in Fig. 7.4a. Coulomb blockade can be lifted by changing the voltage applied to the gate electrode, as can be seen from Eq. 7.5. As shown in Fig. 7.4b When $\nu(N)$ is in the bias window one extra electron can tunnel onto the dot from the source, so that the number of electrons increases from $N-1$ to N. After it has tunneled to the drain, another electron can tunnel onto the dot from the source. This cycle is known as single-electron tunneling.

By sweeping the gate voltage and measuring current, a trace is obtained as shown in Fig. 7.4c. At the positions of the peaks, an electrochemical potential level corresponding to transport between successive ground states is aligned between the source and drain electrochemical potentials and a single-electron tunneling current flows. In the valleys between the peaks, the number of electrons on the dot is fixed due to Coulomb blockade. By tuning the gate voltage from one valley to the next one, the number of electrons on the dot can be precisely controlled. The distance between the peaks corresponds to $\Delta\mu$, and therefore provides insight into the energy spectrum of the dot.

7.6 Large Source-Drain Voltage Region

We now look at the region where the source-drain voltage is so high that multiple dot levels can participate in electron tunneling. Typically the electrochemical potential of only one of the reserviors is changed in experiments, and the other one is kept fixed. Here, we take the drain reservior to be ground. When a negative

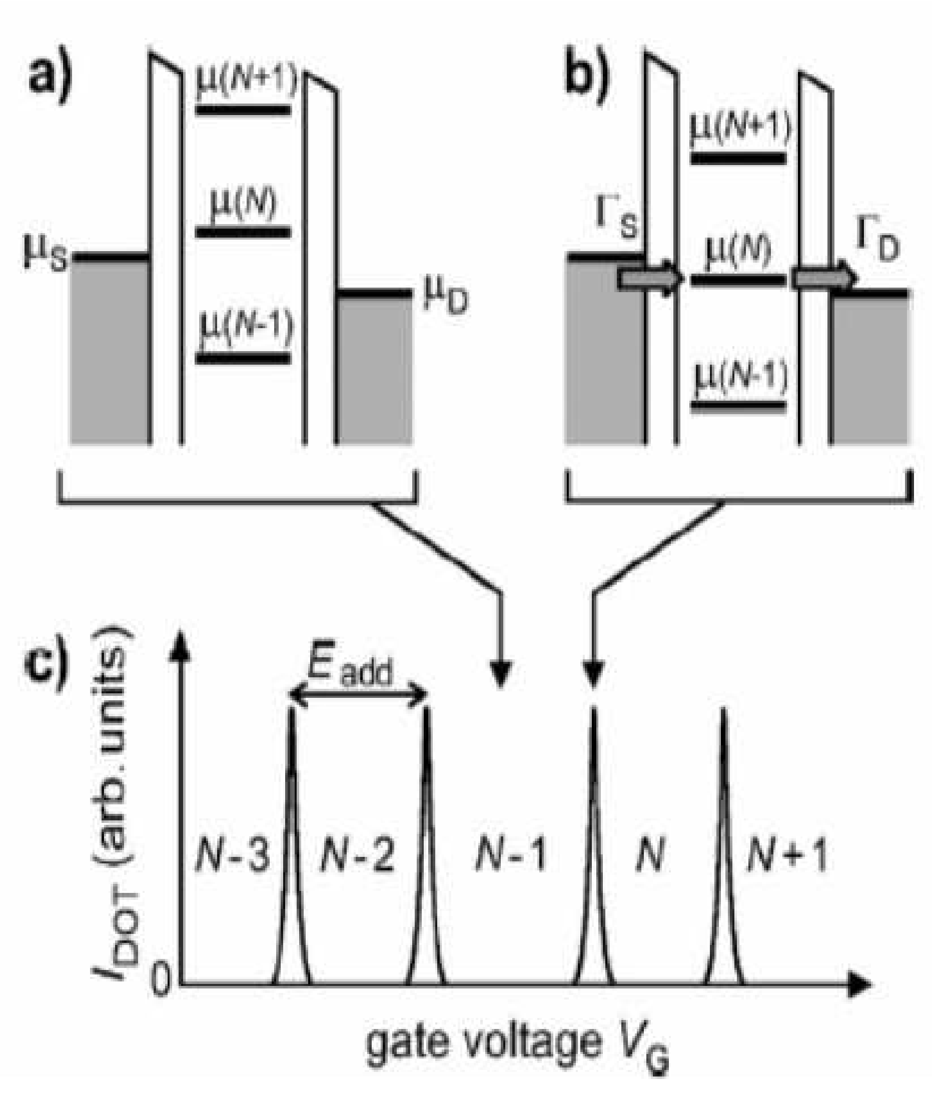

Figure 7.4: Schematic diagrams of the electrochemical potential levels of a quantum dot in the low-bias regime.

voltage is applied between the source and the drain, μ_S increases. The levels of the dot also increase, due to the capacitive coupling between the source and the dot. Again, a current can flow only when a level corresponding to a transition between ground states fall within the bias window. As shown in Fig. 7.5a when V_{SD} is increased further such that also a transition involving an excited state falls within the bias window, there are two paths available for electrons tunneling through the dot. In general, this will lead to a change in current, enable us to perform energy spectroscopy of the excited states. Increasing V_{SD} even more eventually leads to a situation where the bias window is larger than the addition energy as shown in Fig. 7.5b. Here, the electron number can alternate between $N-1$, N, and $N+1$, leading to a double-electron tunneling current.

Next, we would show how the current spectrum as a function of bias and gate voltage can be mapped out. First, the electrochemical potentials of all relevant transitions are calculated by applying Eq. 7.6. Considering two successive ground states, GS(N) and GS(N+1), and the excited states ES(N) and ES(N+1), which are separated from the GSs by $\Delta E(N)$ and $\Delta E(N+1)$ respectively.

As shown in Fig. 7.6, each transition indicates the gate voltage at which its electrochemical potential is aligned with μ_S and μ_D at $V_{SD}=0$. Analogous to low bias case, sweeping the gate voltage show electron tunneling only at the gate voltage indicated by $GS(N) \leftrightarrow GS(N+1)$. For all other gate voltages the dot is in Coulomb blockade. For each transition a V-shaped region is outlined in the schema, where its electrochemical potential is within the bias window. The slopes of the two edges of the V-shape depend on the capacitances. The transition between the N-electron GS and the (N+1)-electron GS (black solid lines) defines the regions of Coulomb blockade (outside the V-shape) and tunneling (within the V-shape). The other solid lines indicate where the current changes due to the onset of transitions involving excited states.

A measurement as shown in Fig. 7.6 is very useful for finding the energies of the excited states, where a line of a transition involving one excited state touches the Coulomb blockade region, the bias window exactly equals the energy level spacing. Here, we show the level diagrams at these special positions for both $ES(N) \leftrightarrow GS(N+1)$ and $GS(N) \leftrightarrow ES(N+1)$.

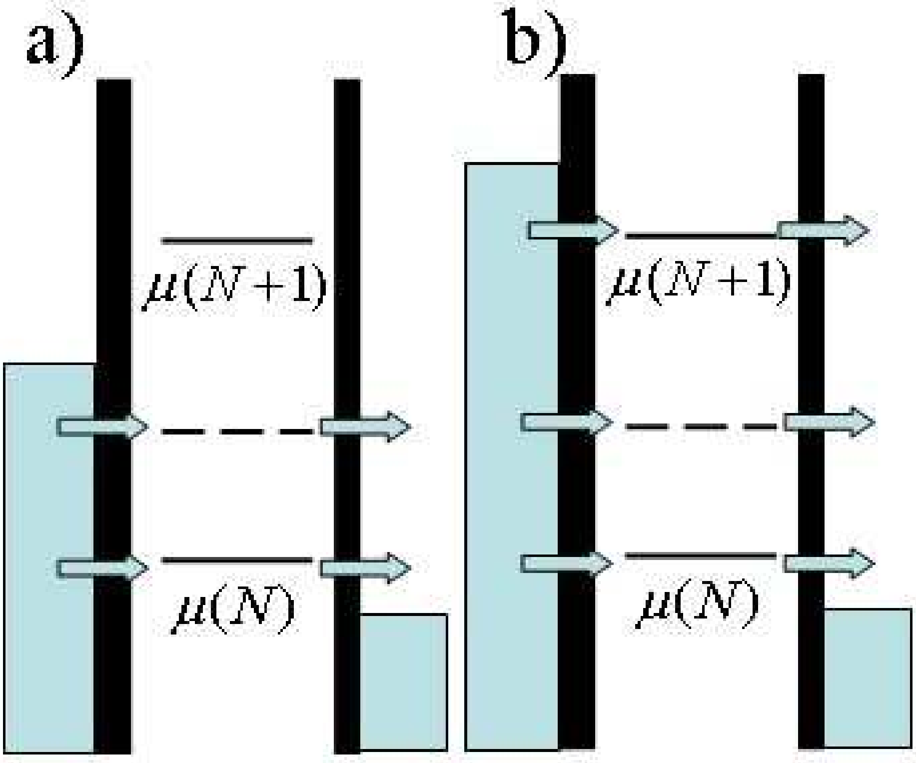

Figure 7.5: Schematic diagrams of the electrochemical potential levels of a quantum dot in the high-bias regime.

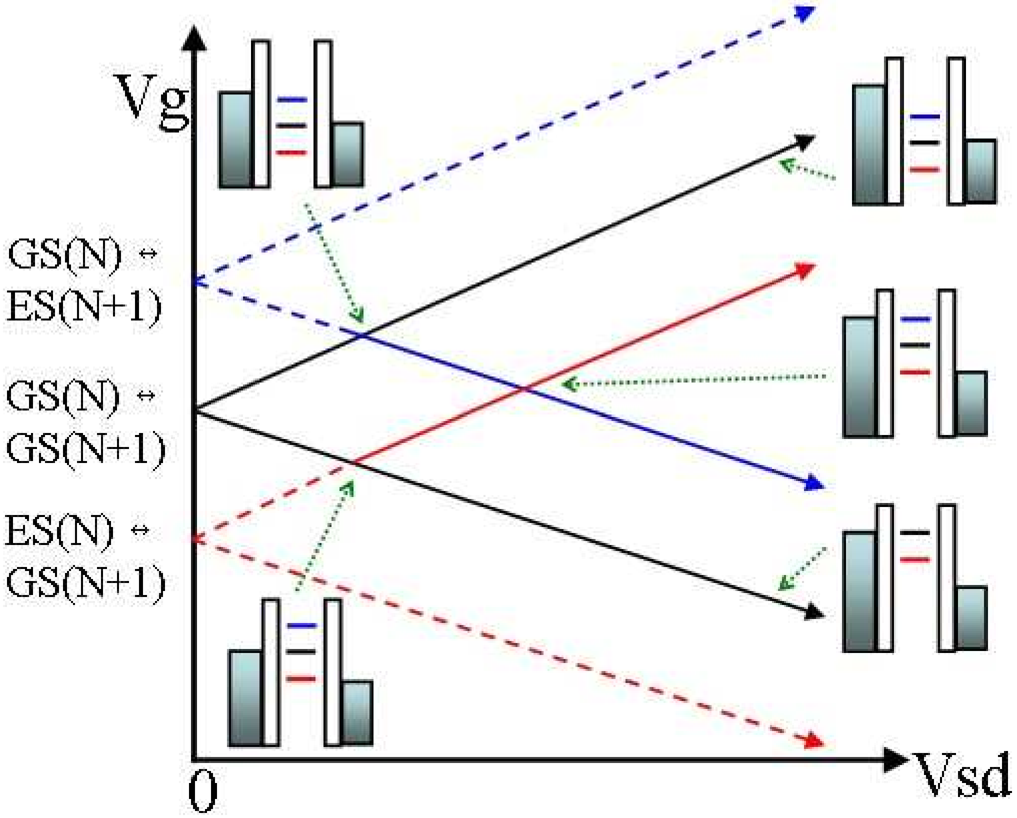

Figure 7.6: Schematic diagrams of the differential conductance as a function of source-drain voltage and gate voltage.

We briefly discuss the transition $ES(N) \leftrightarrow ES(N+1)$, that was neglected in the discussion thus far. The visibility of such a transition depends on the relative magnitudes of the tunnel rates and the relaxation rates. When the relaxation is much faster than the tunnel rates, the dot will effectively be in its ground state all the time and the transition $ES(N) \leftrightarrow ES(N+1)$ can therefore never occur. In the opposite limit where the relaxation is much slower than the tunneling, the transition $ES(N) \leftrightarrow ES(N+1)$ participates in the electron transition and will be visible in a plot like in Fig. 7.6. Thus, the visibility of transition can give information on the relaxation rates between different levels.(111)

If the voltage is swept across multiple electron transitions and for both signs of the bias voltage, the Coulomb blockade regions appear as diamond shapes in the plot. These are the well-known Coulomb diamonds.

7.7 Double Quantum Dots

In the section we introduce the stability (or honeycomb) diagram that visualizes the equilibrium charges states of two serially coupled dots.(112; 113; 114; 115) The double dot is modeled as a network of tunnel resistors and capacitors as shown in Fig. 7.7. The number of electrons on dot 1(2) is $N_{1(2)}$. Each dot is capacitively coupled to a gate voltage $V_{g1(2)}$ through a capacitor $C_{g1(2)}$ and to the source (S) or drain (D) contacts through a tunnel barrier represented by a tunnel resistor $R_{L(R)}$ and a capacitor $C_{L(R)}$ connected in parallel. The dots are coupled to each other by a tunnel barrier represented by a tunnel resistor R_m and a capacitor C_m in parallel. The bias V is applied to the source contact with the drain contact grounded. In this section we consider the linear transport regime, $V \approx 0$. If only concerning cross capacitances (such as between V_{g1} and dot 2), other voltage sources and stray capacitances are negligible, the double dot electrostatic energy reads

$$U(N_1, N_2) = \frac{1}{2}N_1^2 E_{C1} + \frac{1}{2}N_2^2 E_{C2} + N_1 N_2 E_{Cm} + f(V_{g1}, V_{g2}), \qquad (7.7)$$

where $E_{C1(2)}$ is the charging energy of the individual dot 1(2), E_{Cm} is the electrostatic coupling energy, and $-|e|$ is the electron charge. The coupling energy E_{Cm}

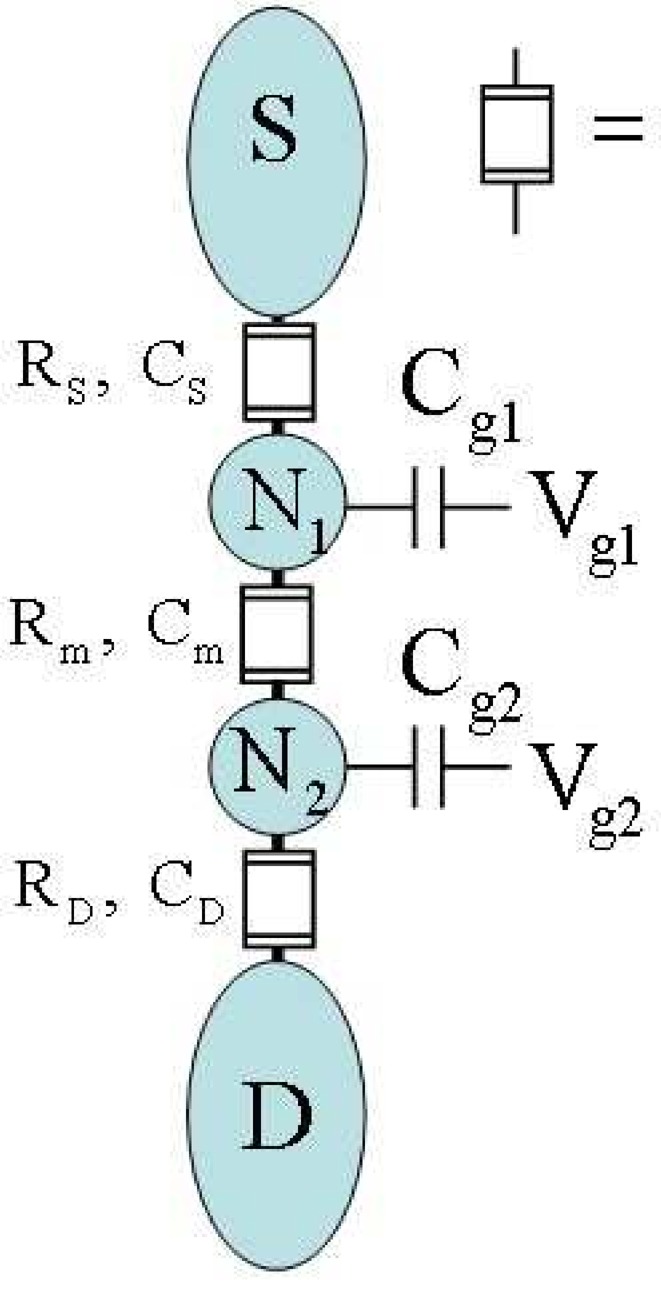

Figure 7.7: Network of tunnel resistors and capacitors representing two quantum dots coupled in series.

is the change in the energy of one dot when an electron is added to the other dot. $f(V_{g1}, V_{g2})$ is defined as:

$$f(V_{g1}, V_{g2}) = \frac{1}{-|e|}\{C_{g1}V_{g1}(N_1 E_{C1} + N_2 E_{Cm}) + C_{g2}V_{g2}(N_1 E_{Cm} + N_2 E_{C2})\}$$

$$+\frac{1}{e^2}\{\frac{1}{2}C_{g1}^2 V_{g1}^2 E_{C1} + \frac{1}{2}C_{g2}^2 V_{g2}^2 E_{C2} + C_{g1}V_{g1}C_{g2}V_{g2}E_{Cm}\},$$

These energies can be expressed in terms of the capacitances as follows:

$$E_{C1} = \frac{e^2}{C_1}(\frac{1}{1-\frac{C_m^2}{C_1 C_2}}), \tag{7.8}$$

$$E_{C2} = \frac{e^2}{C_2}(\frac{1}{1-\frac{C_m^2}{C_1 C_2}}),$$

$$E_{Cm} = \frac{e^2}{C_m}(\frac{1}{\frac{C_1 C_2}{C_m^2}-1}),$$

Here $C_{1(2)}$ is the sum of all capacitances attached to dot 1(2) including C_m, $C_{1(2)} = C_{S(D)+C_{g1(2)}+C_m}$. Note that $E_{c1(2)}$ can be interpreted as the charging energy of the single, uncoupled dot 1(2) multiplied by a correction factor that accounts for the coupling. When $C_m = 0$, and hence $E_{cm} = 0$, Eq.7.7 reduces to

$$U(N_1, N_2) = \frac{(-N_1|e| + C_{g1}V_{g1})^2}{2C_1} + \frac{(-N_2|e| + C_{g2}V_{g2})^2}{2C_2}. \tag{7.9}$$

This is the sum of the energies of two independent dots. In the case when C_m becomes the dominant capacitance ($C_m/C_{1(2)} \rightarrow 1$), the electrostatic energy is given by

$$U(N_1, N_2) = \frac{\{-(N_1 + N_2)|e| + C_{g1}Vg1 + C_{g2}Vg2\}^2}{2(\tilde{C}_1 + \tilde{C}_2)}. \tag{7.10}$$

This is the energy of a single dot with a charge $N_1 + N_2$ and a capacitance of $\tilde{C}_1 + \tilde{C}_2$, where $\tilde{C}_{1(2)} = C_{1(2)} - C_m$ is the capacitance of dot 1(2) to the outside world. Thus a large interdot capacitance C_m effectively leads to one big dot.

The electrochemical potential $\mu_{1(2)}(N_1, N_2)$ of dot 1(2) is defined as the energy needed to add the $N_{1(2)}$th electron to dot 1(2), while having $N_{2(1)}$ electrons on dot 2(1). Using the expression for the total energy Eq. 7.7, the electrochemical potentials of the two dots are

$$\begin{aligned} \mu_1(N_1,N_2) &\equiv U(N_1,N_2) - B(N_1-1,N_2) \\ &= (N_1-\frac{1}{2})E_{C1} + N_2E_{Cm} - \frac{1}{|e|}(C_{g1}V_{g1}E_{C1} + C_{g2}V_{g2}E_{Cm}), \end{aligned} \tag{7.11}$$

$$\begin{aligned} \mu_2(N_1,N_2) &\equiv U(N_1,N_2) - B(N_1,N_2-1) \\ &= (N_2-\frac{1}{2})E_{C2} + N_1E_{Cm} - \frac{1}{|e|}(C_{g1}V_{g1}E_{Cm} + C_{g2}V_{g2}E_{C2}). \end{aligned} \tag{7.12}$$

The change in $\mu_1(N_1,N_2)$ if, at fixed gate voltages, N_1 is changed by 1, $\mu_1(N_1+1,N_2) - \mu_1(N_1,N_2) = E_{C1}$, is called the addition energy of dot 1 and equals the charging energy of dot 1 in this classical regime. Similarly, the addition energy of dot 2 equals E_{C2}, and $\mu_1(N_1,N_2+1) - \mu_1(N_1,N_2) = \mu_2(N_1+1,N_2) - \mu_2(N_1,N_2) = E_{Cm}$. In the next section we will discuss the addition energy in the quantum regime, where also the spacing between discrete energy levels plays a role.

From the electrochemical potentials in Eq. 7.11 and Eq. 7.12 we construct a charge stability diagram, giving the equilibrium electron numbers N_1 and N_2 as a function of V_{g1} and V_{g2}. We define the electrochemical potentials of the source and drain leads to be zero if no bias voltage is applied, $\mu_S = \mu_D = 0$. Hence the equilibrium charges on the dots are the largest values of N_1 and N_2 for which both $\mu_1(N_1,N_2)$ and $\mu_2(N_1,N_2)$ are less than zero. If either is larger than zero, electrons escape to the leads. This constraint, plus the fact that N_1 and N_2 must be integers, creates hexagonal domains in the (V_{g1},V_{g2}) phase space in which the charge configuration is stable.

For completely decoupled dots ($C_m = 0$) the diagram looks as in Fig. 7.8a. The gate voltage $V_{g1(2)}$ changes the charge on dot 1(2), without affecting the charge on the other. If the coupling is increased, the domains become hexagonal as shown in Fig. 7.8b. The vertices of the square domains have separated into triple points. When C_m becomes the dominant capacitance ($C_m/C_{1(2)} \equiv 1$), the triple point separation reaches it maximum as shown in Fig. 7.8c. The double dot behaves like one dot with charge $N_1 + N_2$, as see from Eq. 7.10.

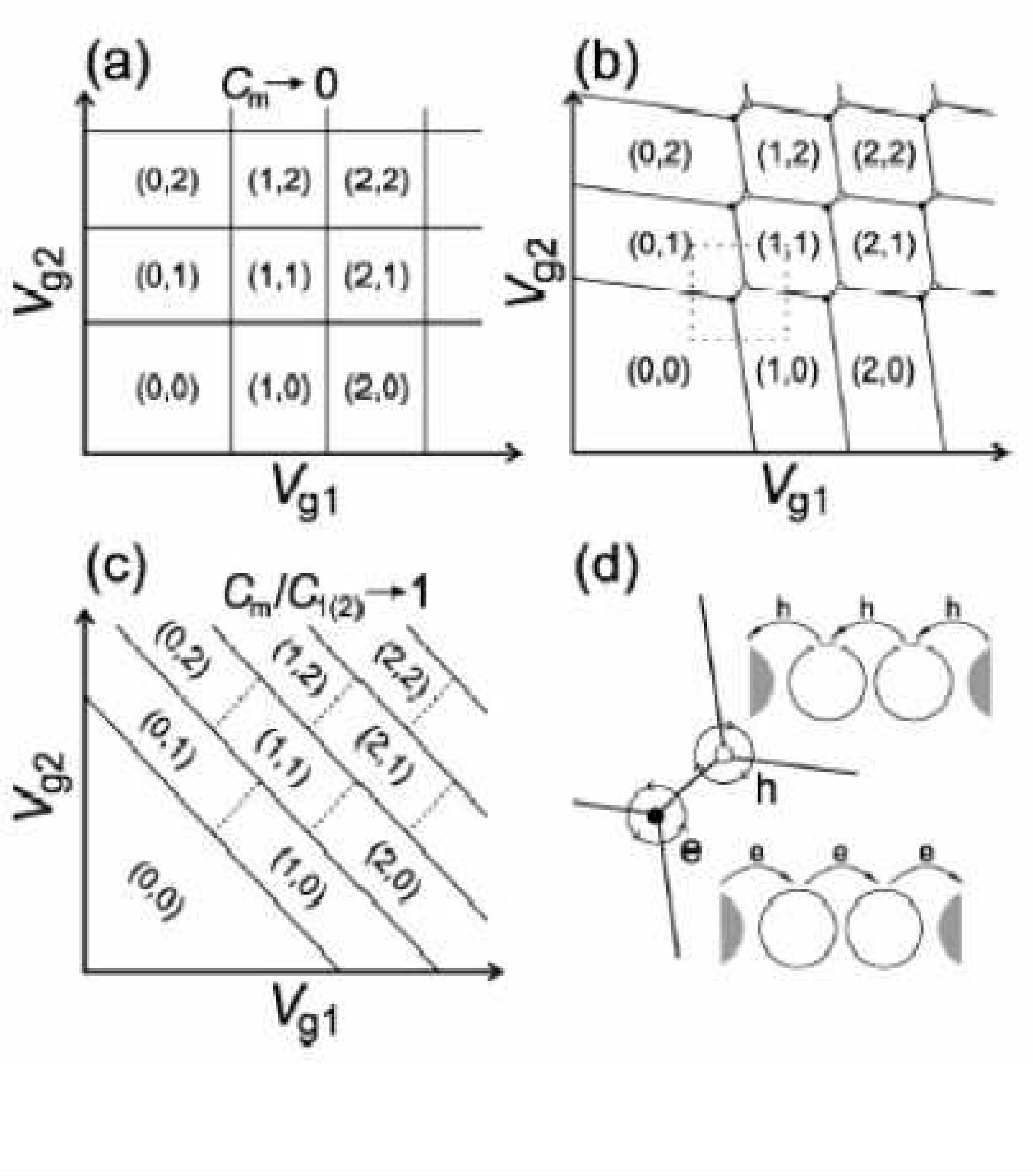

Figure 7.8: Schematic stability diagram of the double dot system for (a) small, (b) intermediate, and (c) large interdot coupling. The equilibrium charge on each dot in each domain is denoted by (N_1, N_2). The two kinds of triple points corresponding with the electron transfer process (•) and the hole transfer process (∘) are illustrated in (d).

We are considering the linear region of conductance, implying $\mu_S - \mu_D \approx 0$. In order to obtain a measurable current, the tunnel barriers need to be sufficiently transparent. At the same time, however, the tunnel barriers need to be sufficiently opaque to ensure a well-defined electron number on each dot. For double dots coupled in series, a conductance resonance is found when electrons can tunnel through both dots. This condition is met whenever three charge states become degenerate, i.e. whenever three boundaries in the honeycomb diagram meet in one point. In Fig. 7.8d two kinds of such triple points are distinguished, (•) and (◦), corresponding to different charge transfer processes. At the triple point (•), the dots cycle through the sequence

$$(N_1, N_2) \equiv (N_1 + 1, N_2) \equiv (N_1, N_2 + 1) \equiv (N_1, N_2),$$

which shittle one electron through the system. This process is illustrated by the counterclockwise path e and the diagram of an electron sequentially tunneling from the left lead to the right lead in Fig. 7.8d. At the other triple point (◦), the sequence is

$$(N_1 + 1, N_2 + 1) \equiv (N_1 + 1, N_2) \equiv (N_1, N_2 + 1) \equiv (N_1 + 1, N_2 + 1),$$

corresponding to the clockwise path h in Fig. 7.8d. This can be interpreted as the sequential tunneling of a hole in the direction opposite to the electron. The energy difference between both processes determines the separation between the triple point (•) and (◦) and is given by E_{Cm} as defined in Eq.7.8.

As shown in Fig. 7.9 the dimensions of the honeycomb cell can be related to the capacitances using Eq. 7.11 and Eq. 7.12. From

$$\mu_1(N_1, N_2; V_{g1}, V_{g2}) = \mu_1(N_1 + 1, N_2; V_{g1} + \Delta V_{g1}, V_{g2}), \tag{7.13}$$

we obtain

$$\Delta V_{g1} = \frac{|e|}{C_{g1}}, \tag{7.14}$$

and similarly we can derive

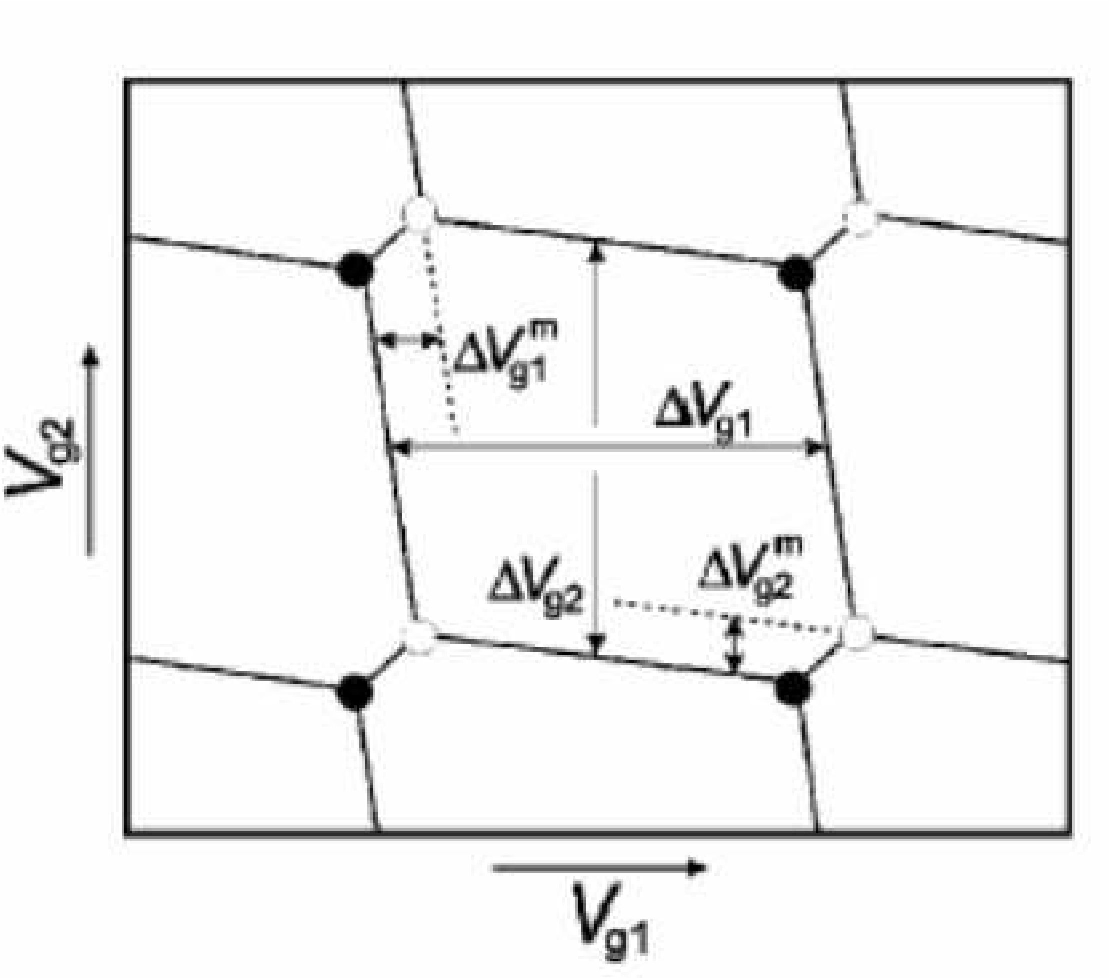

Figure 7.9: Schematic stability diagram showing the Coulomb peak sapcings.

$$\Delta V_{g2} = \frac{|e|}{C_{g2}}. \tag{7.15}$$

From

$$\mu_1(N_1, N_2; V_{g1}, V_{g2}) = \mu_1(N_1, N_2 + 1; V_{g1} + \Delta V_{g1}^m, V_{g2}), \tag{7.16}$$

we obtain

$$\Delta V_{g1}^m = \frac{|e|C_m}{C_{g1}C_2} = \Delta V_{g1}\frac{C_m}{C_2}, \tag{7.17}$$

and similarly we can derive

$$\Delta V_{g2}^m = \frac{|e|C_m}{C_{g2}C_1} = \Delta V_{g2}\frac{C_m}{C_1}. \tag{7.18}$$

Chapter 8

Experimental and Technical Considerations

8.1 Introduction

A quantum dot is an artificially structured system that can be filled with electrons or holes. The dot can be coupled via tunneling barriers to reservoirs, with which electron can be exchanged. By attaching current and voltage probes to these reservoirs, we can measure the electronic properties. The dot is also coupled capacitively to one or more gate electrodes, which can be used to tune the electrostatic potential of the dot with respect to the reservoirs. There are many kinds of systems which can act as quantum dot. For examples: carbon nanotubes,(116) normal metal,(117) semiconductor nanowires,(118) semiconductor lateral(119; 120) or vertical dots.(121) In my work, I focus on the semiconductor heterostructure vertical double quantum dots.

The vertical quantum dots are fabricated from heterostructures of GaAs (InGaAs) and AlGaAs grown by molecular beam expitaxy. By doping the AlGaAs layer with Si, free electrons are introduced. These accumulate at the GaAs/AlGaAS interface, typically 50 $\sim$ 100 nm below the surface, forming a two-dimensional electron gas (2DEG), a thin ($\sim$ 10nm) sheet of electrons that can only move along the interface. The 2DEG can have a high mobility and relatively low electron density (typically 10^5 cm^2/Vs and $1 \sim 5 \times 10^{15}$ m^{-2}, respectively).

Electron-beam lithography enables fabrication of gate structures with dimensions down to a few tens of nanometers. In the section of experiment on quantum dot, we would discuss the method of fabrication and consideration of measurement.

8.2 Sample Fabrication

As shown in Fig. 8.1, there are eight processes for fabricating a quantum dot.

Step (a): Designed and growed the anticipated structure of 2DEG.

Step (b): Depositing the source and drain contacts. The depositing material is Ti/Au.

Step (c): Dry etching: undercut the 2DEG by plasma.

Step (d): Wet etching: etch the 2DEG to make the "pillar" narrow by solvent of acid.

Step (e): Depositing the side gate.

Step (f): Undercut the edge of 2DEG. This step is a preparation for next step.

Step (g): Depositing the insulator.

Step (h): Depositing the contact of back gate.

Because a quantum dot is so small to all of the process should be done in high level cleaning room. It needs several exquisite fabrications and also proficient and careful operation in many delicate machines such as e-bean lithography, plasma etching, STM, e-bean evaporator, wire bonding, etc.

Figure 8.2 shows the fabricated quantum dot and its wiring from the microscopic scale to macroscopic scale. The diameter of the quantum dot is 0.5 μm.

8.3 Amplitude and Lineshape of Coulomb Oscillations

The tunneling amplitude and line shape of coulomb oscillations depends on the temperature of electron. In the quantum Coulomb regime, $k_B T \ll \Delta E \ll e^2/C$, tunneling occurs through a single level.(122) The temperature dependence of single peak conductance is given by

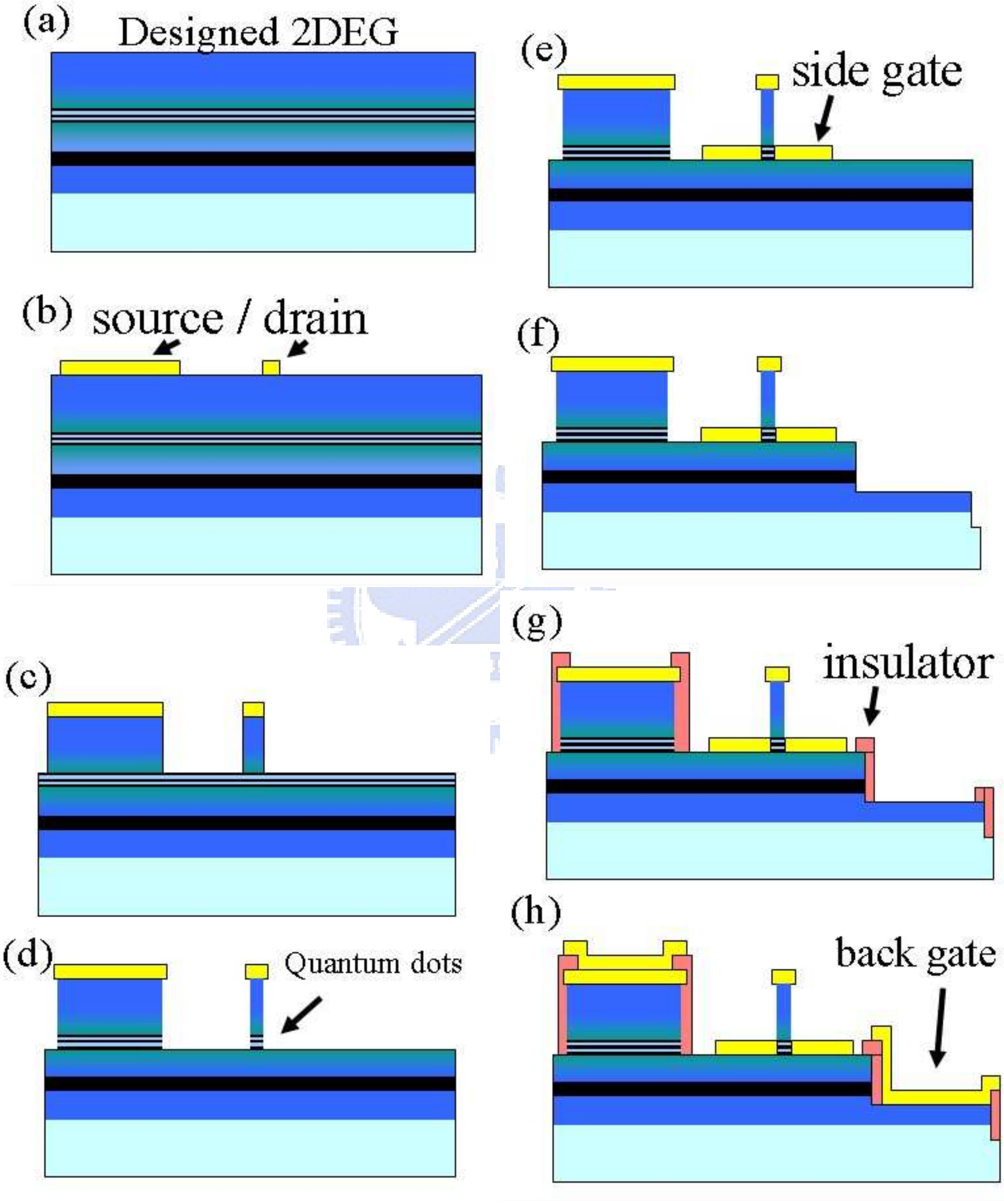

Figure 8.1: The processes for fabricating quantum dot.

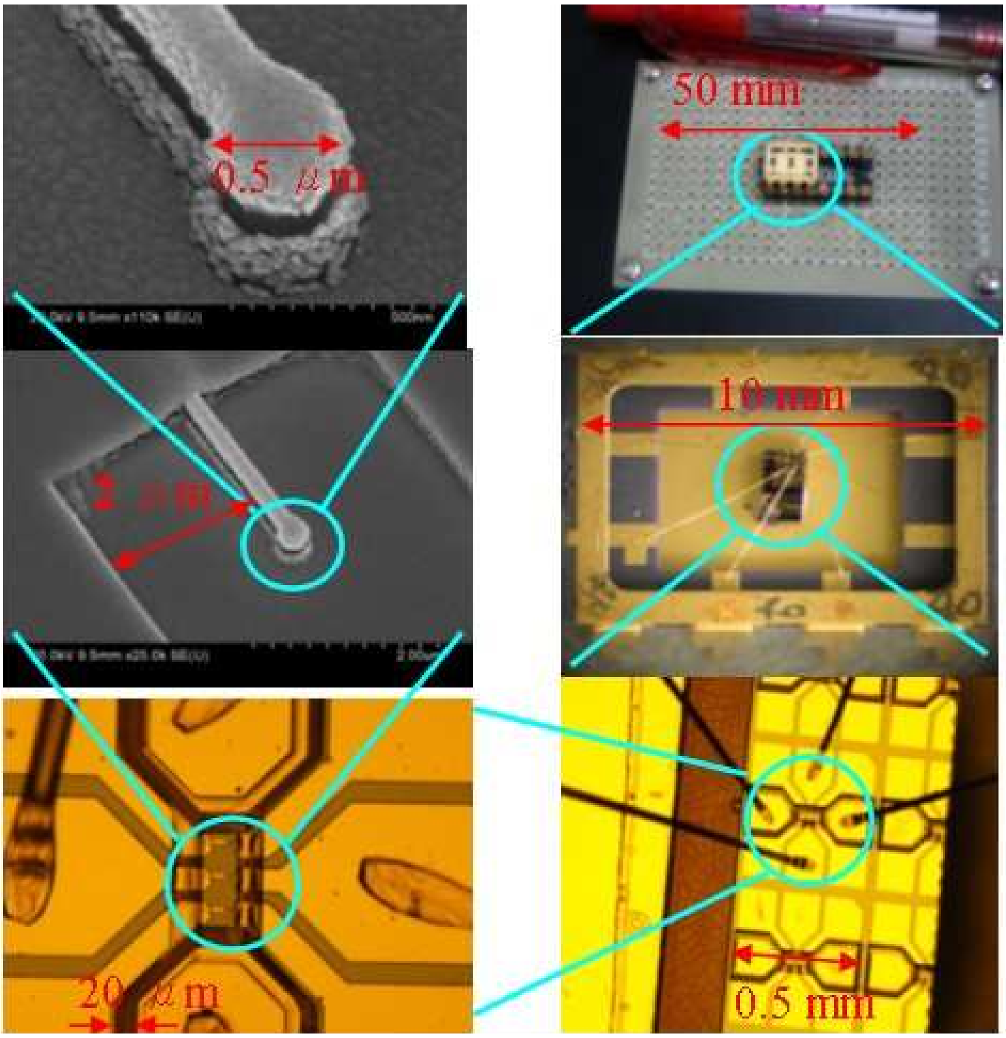

Figure 8.2: The fabricated quantum dot and wirings.

$$\frac{G}{G_\infty} = \frac{\Delta E}{4k_BT} cosh^{-2}(\frac{\delta}{2k_BT}). \tag{8.1}$$

With the assumption that ΔE is independent of E and N. δ measures the distance to the center of the peak in units of energy, which expressed in gate voltage is $\delta = e(C_g/C)|V_{g,res} - G_g|$, with $V_{g,res}$ the gate voltage at resonance. The lineshape in the classical and quantum regimes are virtually the same, except for the different "effective temperature". However, the peak maximum $G_{max} = G_\infty(\Delta E/4k_BT)$ decreases linearly with increasing temperature in the quantum regime, while it is constant in the classical regime. The distinguishes a quantum peak from a classical peak. Figure 8.3 show several lineshapes in quantum regime at different temperatures. The parameter are $\Delta E = 0.01e^2/C$ and $k_BT/\Delta E =$ 0.5, 1, 7.5, and 15 for line a, b, c, and d respectively. One important we should know is that the full width at half maximum determines the temperature of electrons.

8.4 Low Temperature Measurement

To observe the effects of the atom-like orbits and the charging energy on transport, the thermal energy k_BT must be well below the energy scales of the dots, which correspond to temperatures of order 1 K (≈86 μeV). Therefore, our experiments were performed in a dilution refrigerator that can cool down to 10 mK. The effective electron temperature that we achieved in semiconductor quantum dots was about 100 mK. Special care must be taken to avoid spurious heating of the electrons in the device. Below we give a brief enumeration of the issues involving in doing these sensitive measurements. The noise of measurement is less than 30 fA.

8.4.1 Filter

A significant source of heating is the noise coming from the measurement electronics. Filters, used to attenuate the noise that arrives at the samples, have to be effective over a very large band width. Figure 8.4 shows the schema of the filters we used in the measurement of quantum dot. A thin resistive wire go through

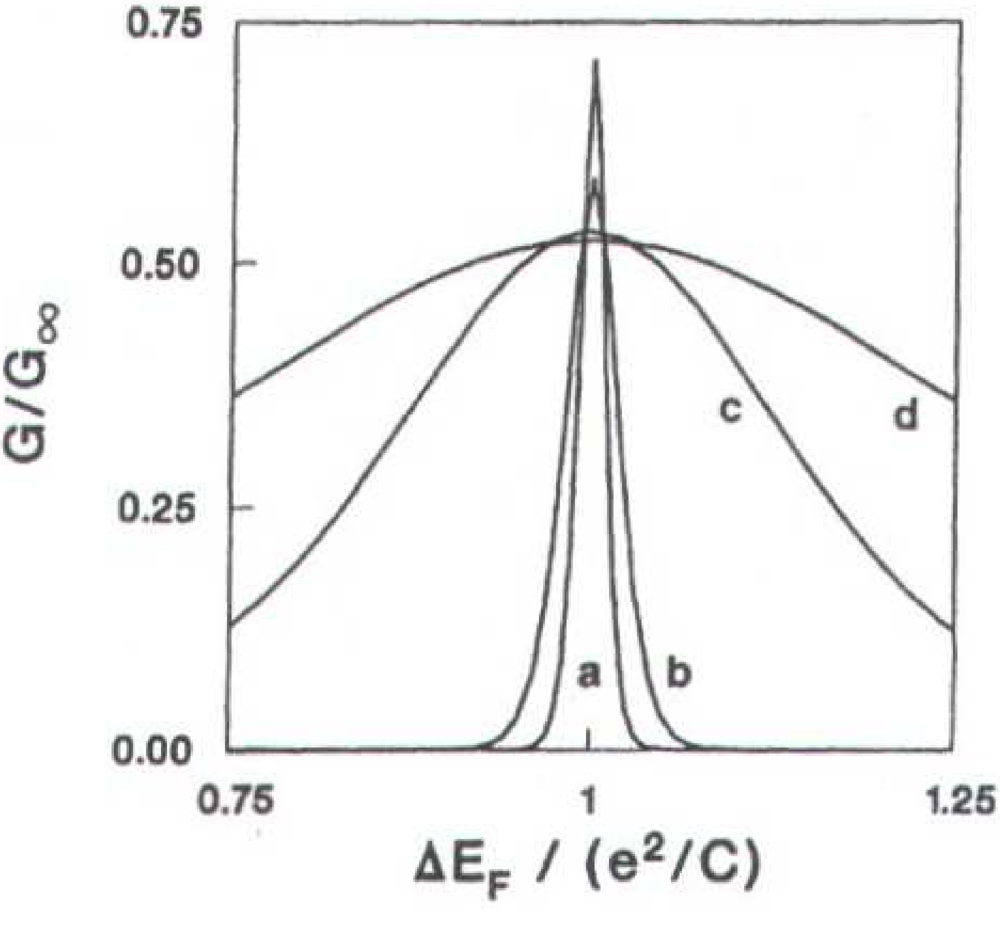

Figure 8.3: The lineshape of Coulomb oscillation in quantum regime at different temperature. The parameter are $\Delta E = 0.01e^2/C$ and $k_BT/\Delta E = 0.5$, 1, 7.5, and 15 for line a, b, c, and d respectively.

a copper power medium. In the filters, we use manganin wires as the resistive wires. The manganin wire is made of Cu (86%), Mn (12%), and Ni (2%) and the resistance is about 105 Ω/m. The network is equal to a RC filter. The filters are installed at low temperature to minimize the thermal noise of the resistors contained in the filters. The filters are integrated with the sample holder in such a way that all sample wires are carefully shielded once they are filtered. Except of power supplier of magnet, all of the instruments are located in the shielding room to attenuate the high frequency noise from outside.

8.4.2 Shielding Room and Power

In order to avoid the external noise coming into the measuring system, all of electric meters and cryostat are put in shielding room and all of the experiments are operated in shielding room. The shielding room we used is a commercial product. The attenuate amplitude is about 100 dB for the frequency ranging from 500 KHz to 1 GHz. Besides, the current is filtered by LC filters before enters the shielding room. The attenuate amplitude of the LC filter is 60 dB for frequency ranging from 500 KHz to 1 GHz. The Fig. 8.5 shows the connection of filters of power.

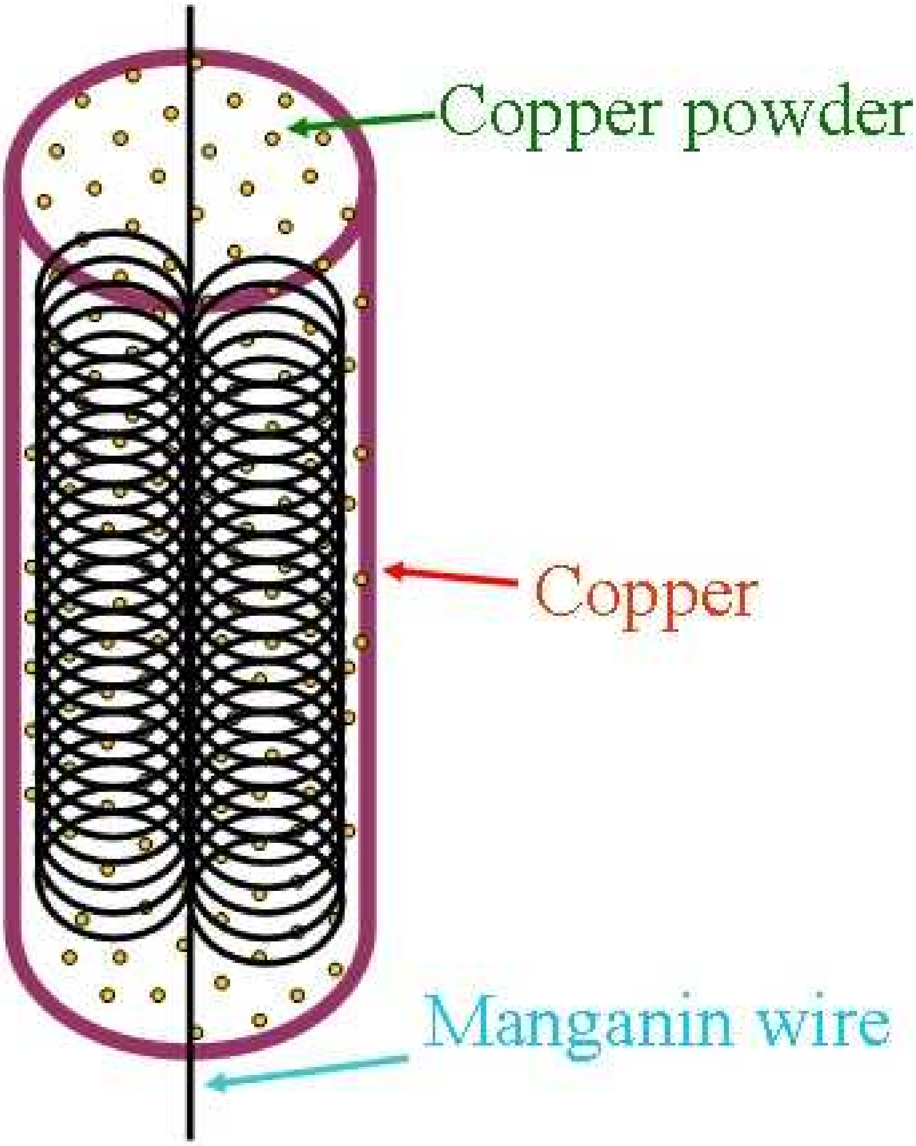

Figure 8.4: The transection of filter.

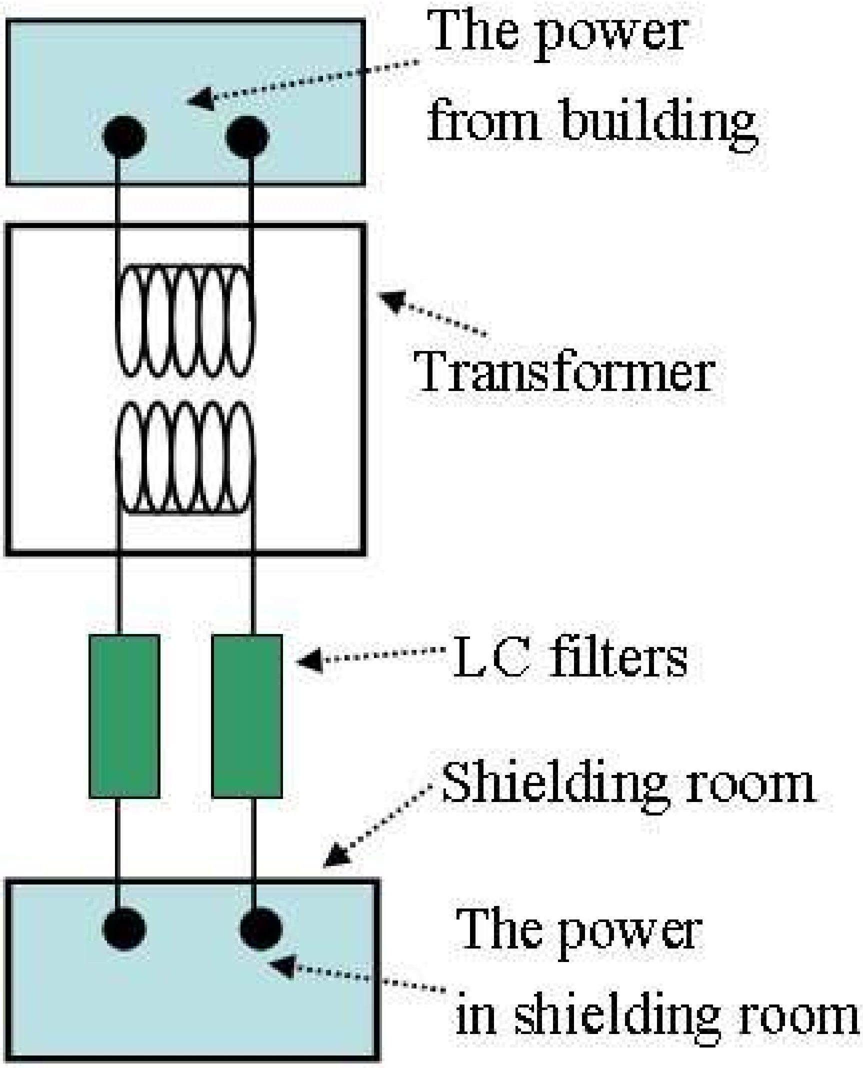

Figure 8.5: The schema of the power in shielding room.

Chapter 9

Results and Discussions

9.1 Introduction

The study of individual spin is motivated by an interest in fundamental physics, but also by possible applications.(123; 124; 125; 126) First of all, miniaturized spintronics is developing towards single spins. A second area of applications is quantum information science. Here spin states are qubits. By entangling two spins, quantum logic can be performed such as the controlled-NOT operation. The original proposed be Loss and DiVincenzo has been the guide in this field.(124) Many of works have done in progress.(127; 128; 129; 130; 131; 132) We have done two topics in the series of work on the quantum dot. First one is the spin selection rule. The second one is spin transport in double quantum dots with Zeeman mismatch.

9.2 Spin Selection Rule

A study of spin-dependent transport has attracted considerable attention over the past several decades, because the advantages of two intrinsic states and a long relaxation time result in the great potential of application of spintronics and quantum information. A confined semiconductor quantum dot is a popular material to study, because it can be regarded as an artificial atom, since its electronic properties resemble the ionization energy and discrete excitation spectrum of atoms.(133) However, the spins in the confined semiconductor quantum dot often couple with other environmental freedom components; thus, to understand spin states is an important issue in the study. For single electron states, it is already well studied using a two-dimensional harmonic potential.(134) In non-single-particle electron systems, electron states are often characterized by the total electron number and electron spin in the presence of Coulomb interaction. Electron spin states have been identified in several systems, such as the two-singlet state replaced by a spin-polarized phase, at which electrons occupy some orbit states in the first and second Landau levels,(135) and a quantum two-level system based on the two-electron spin state in a double quantum dot.(104)

In spin-dependent transport, both spin states and effective transition processes are important. Recently, the Zeeman splitting peaks in a few-electron quantum have been investigated.(136) The excited state of Zeeman splitting depends on whether the total spin is raised or lowered. On the other hand, one-electron Zeeman splitting is clearly resolved at both zero-to-one and one-to-two electron transitions in a lateral quantum dot. The spin of the electrons transmitted through the dot is expected to be that of an electrically tunable, bipolar spin filter.(137)

In this study, we investigated the single-electron transport in a vertical double quantum dot and two-electron spin states and transitions. We observed spin-selection-rule-induced blockade. We also observed that a spin excitation spectrum is missing owing to the spin selection rule between the spin doublet and spin triplet states.

Figure 9.1 shows the structure of vertical double quantum dots. Double quantum dots are prepared from semiconductor multibarrier heterostructures surrounded by metal gate electrodes. $\mathrm{In_{0.05}Ga_{0.95}As}$ dots are located between $\mathrm{Al_{0.22}Ga_{0.78}As}$ heterostructure barriers. From bottom to top, the dots consist of an n-doped GaAs substrate, undoped layers of 75 Å $\mathrm{Al_{0.22}Ga_{0.78}As}$, 120 Å $\mathrm{In_{0.05}Ga_{0.95}As}$, 60 Å $\mathrm{Al_{0.22}Ga_{0.78}As}$, 120 Å $\mathrm{In_{0.05}Ga_{0.95}As}$, and 75 Å $\mathrm{Al_{0.22}Ga_{0.78}As}$, and an n-doped GaAs top layer. The electrons in the dots are confined in all directions. By decreasing the gate voltage V_g, we can reduce the effective dot area and hence tune the effective electron number one by one down to zero in the dots.

A sample is mounted on the mixing chamber of a dilution refrigerator with a base temperature of 20 mK. We apply magnetic fields up to 15 T vertical to the

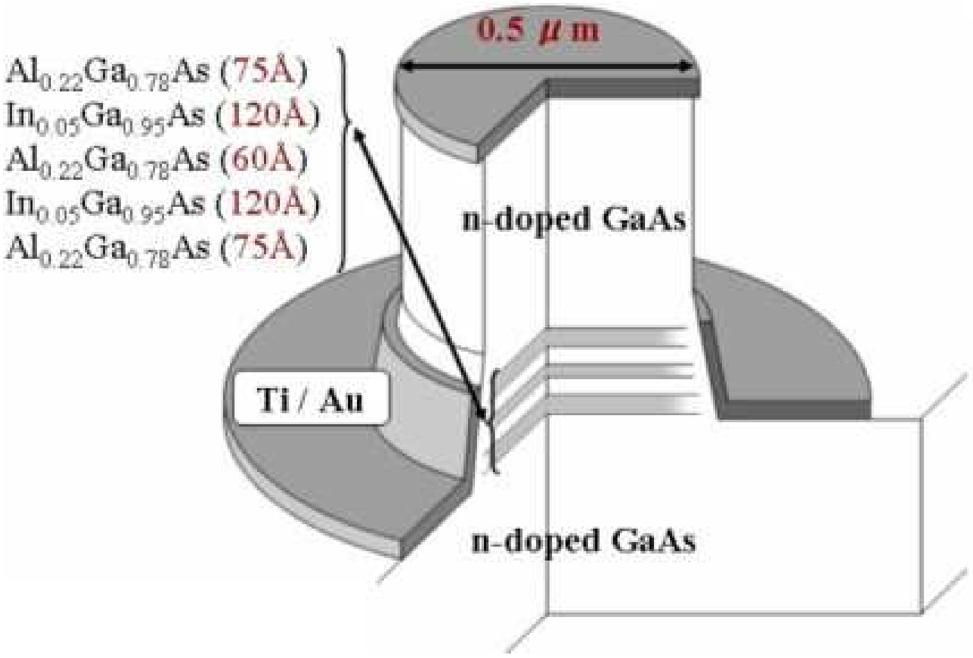

Figure 9.1: The structure of vertical double quantum dots.

heterostructures.

The inherent asymmetry in the tunneling barriers of few electron dots induces intrinsically different tunneling currents for forward and reverse source-drain biases in a nonlinear transport regime.(138) We set the tunneling rate of the incoming barrier to be much smaller than that of the outgoing barrier. As a result, more excited state spectra are shown and the intensity of the current increases.

Figure 9.2 shows the differential conductance as a function of source-drain voltage and gate voltage. The three colors, blue, red, and white, represent negative, positive, and zero differential conductances, respectively. It shows several parallelograms which are commonly known as Coulomb diagrams, in the white regions. In order to measure the electron transportation via ground state and excited states of quantum dots as a function of magnetic fields, we apply a constant source-drain voltage and sweep gate voltage and magnetic fields.

Figure 9.3 shows the measured differential conductance, dI_{sd}/dV_g at large bias region as a function of V_g and magnetic field B. The three colors, blue, red, and white, represent negative, positive, and zero differential conductances, respectively. As shown in Fig. 9.3, we label electron number states as ($N1$, $N2$) in different regions, where $N1$ and $N2$ are the total numbers of electrons in Dot 1 and Dot 2, respectively. The middle stripe denotes the third electron transport spectrum, which shows the transport states of the $(1,1) \leftrightarrow (1,2)$ transition.

At different regimes, the electron tunneling processes are different. We label A, B, C, and D for different tunneling regions. Figure 9.4 indicates the tunneling processes of different regimes. We clearly observe that the color in the region A is lighter than that of the region B. It means that the differential conductance, i.e, the transition rate, in the region A is smaller than that in the region B. At low temperatures, high-order transport processes can dominate tunneling processes. In the region A, even though only the energy state of right dot locates within the transport window, electron tunnels through the left dot to the state of right dot via high-order transport processes. The tunneling process is commonly known as co-tunneling event.(139) The tunneling in the region B and region D are normal resonance tunneling processes. The regime C is in Coulomb blockage region.

M. Wagner and co-workers(140; 141) consider a case of that two interacting electrons confined to a quantum dot in a perpendicular magnetic field. They

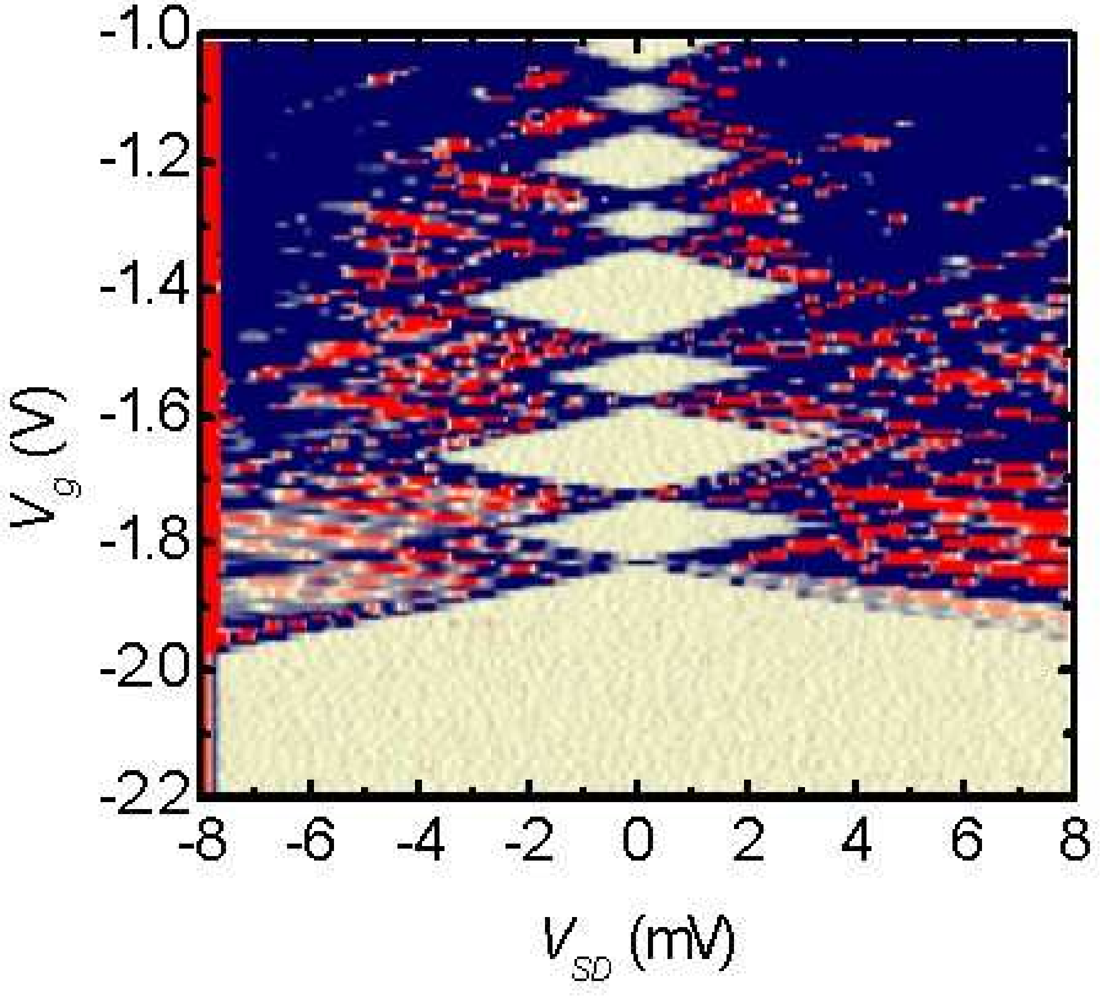

Figure 9.2: Coulomb diamond.

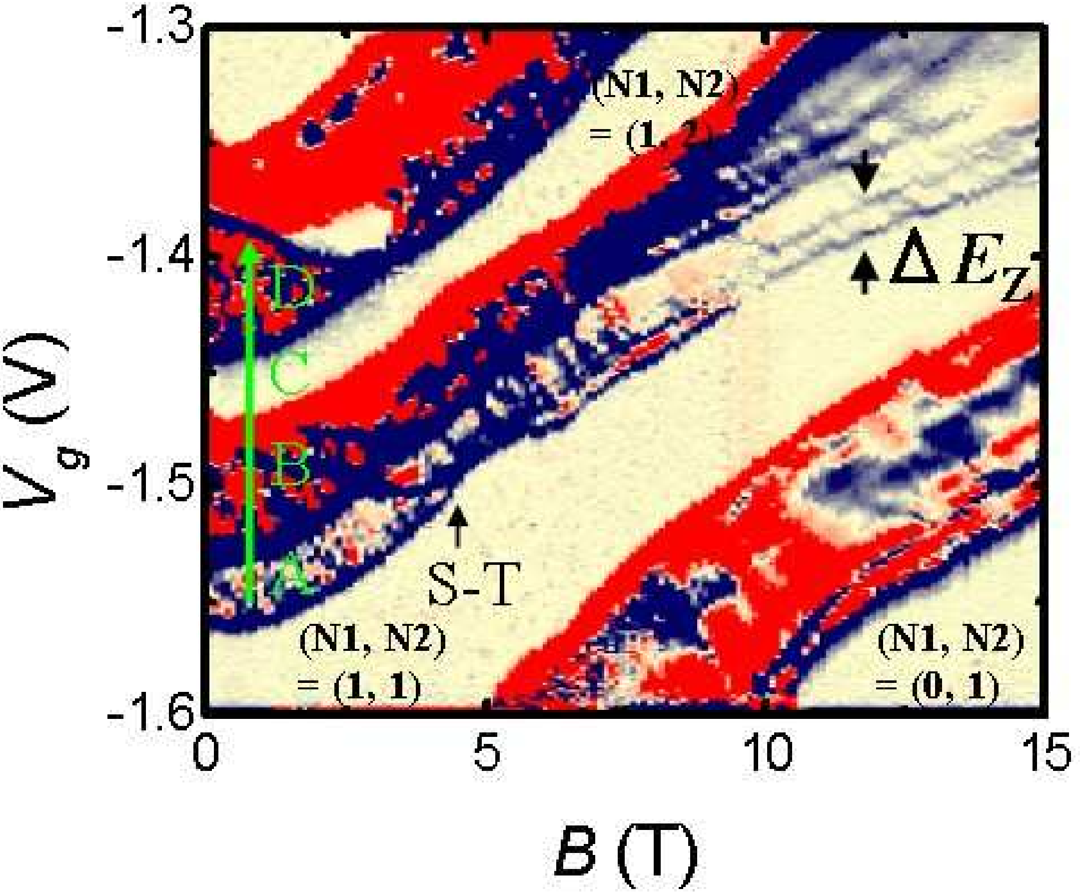

Figure 9.3: The measured differential conductance as a function of gate voltage and magnetic fields.

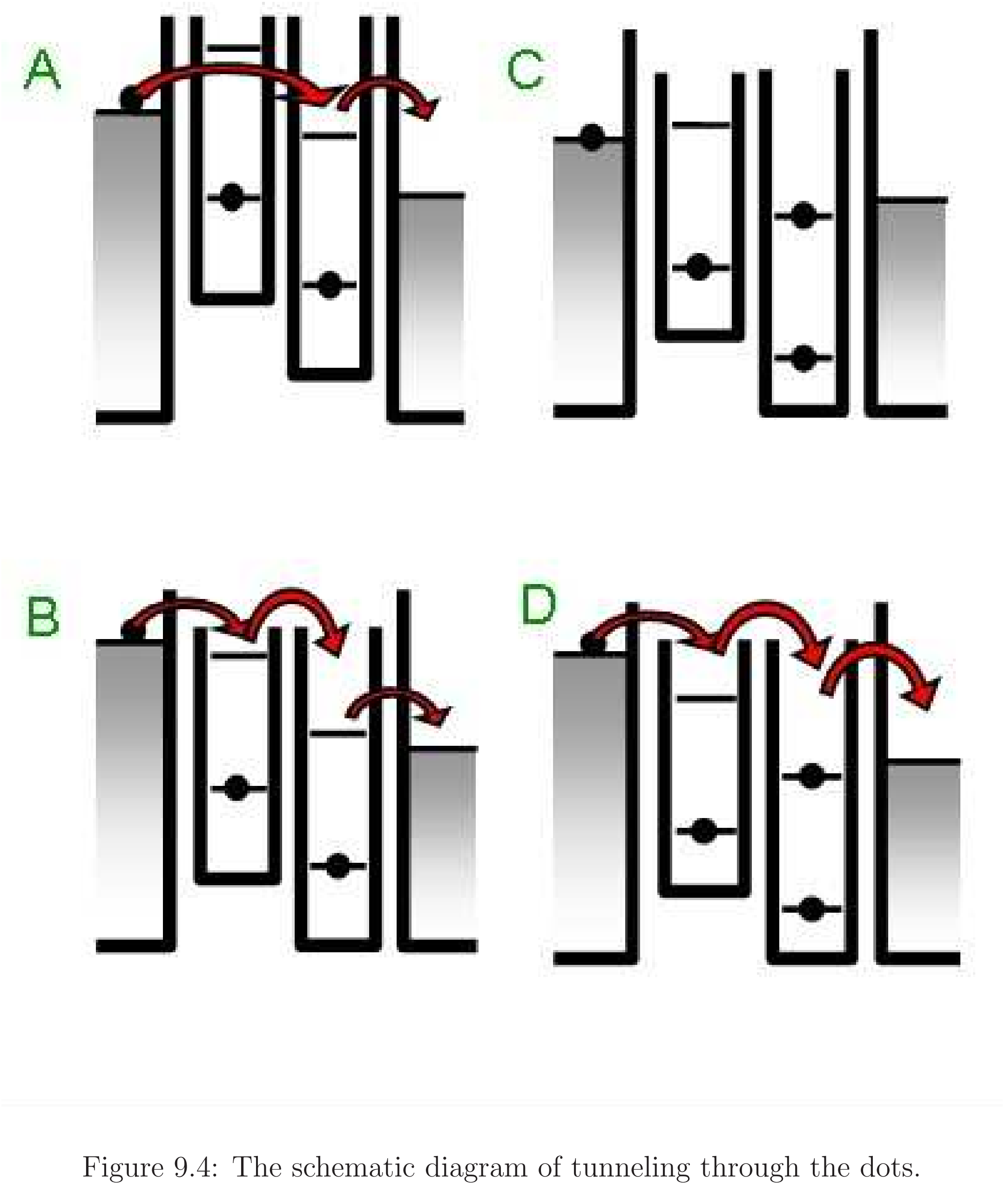

Figure 9.4: The schematic diagram of tunneling through the dots.

investigate the ground state of the two-electron system as a function of dot size and magnetic field strength. The important feature of the ground state to be discussed here is that its angular momentum, l, does depend on the Coulomb interaction. If neglecting the Coulomb interaction, the $l = 0$ state is always the ground state. If including the Coulomb interaction, the state $l = 0$ remains as a ground state only for low magnetic fields. As the magnetic field increases, the state rise in energy while the state $l = -1, -2, ...$ drop, thus leading to a sequence of different ground states $l = 0, -1, -2, ...$ as the magnetic field is swept. The reason for these changes of symmetry of the ground is found in the competition of the various energies contributing to the energy of the relative motion. On the one hand, a higher angular momentum l means higher rotational energy, but on the other hand, the average distance between the two electrons is then increased and hence the Coulomb energy get smaller.

From now on, we will focus our discussion only on the transport spectrum of region A in Fig. 9.3. It is the transportation of $(N_1, N_2) = (1, 1) \leftrightarrow (1, 2)$. At zero magnetic fields, the ground state of right dot follows the Pauli exclusion rule indicating that two electrons have opposite spins of the same angular momentum quantum number $l = 0$. The total electron spin is zero, indicating the spin singlet state. As discussed above, the Coulomb interaction and single-particle states become important when a magnetic field changes the size of on electron state. In the presence of a magnetic field, the electron state shrinks in the redial direction. When two electrons occupy the same angular momentum state, the average distance between the two electrons decreases with magnetic field, and hence, the Coulomb interaction increases. At a critical magnetic field B_c, the Coulomb interaction is reduced by an exchange energy. One electron occupies the $l = 0$ angular momentum state and the other one occupies the $l = 1$ state. The two electrons can take on parallel spins. The ground state is considered the spin triplet state, in which one electron is in the angular momentum state $l = 0$ and the other electron in the angular momentum state $l = 1$, to reduce the Coulomb interaction. We mark the singlet-triplet transition point by a arrow. The spin singlet-triplet transition is observed at 5 T which agrees with the literature well.(142)

As the magnetic field further increasing, we observe two Zeeman splitting lines. The Zeeman splitting energies are labeled as ΔE_Z. Figure 9.5 shows the extracted Zeeman splitting energy as a function of magnetic fields. The Zeeman energy of the two lines is linear with magnetic fields up to 15 T and the effective Zeeman g-factor is 0.36 ± 0.02. One interesting point is that there should be four states, one spin singlet state and three spin triplet states, if we only consider two lowest angular momentum states, $l = 0$ and $l = 1$. Instead of observing two Zeeman sub-levels, we should observe four transition lines.

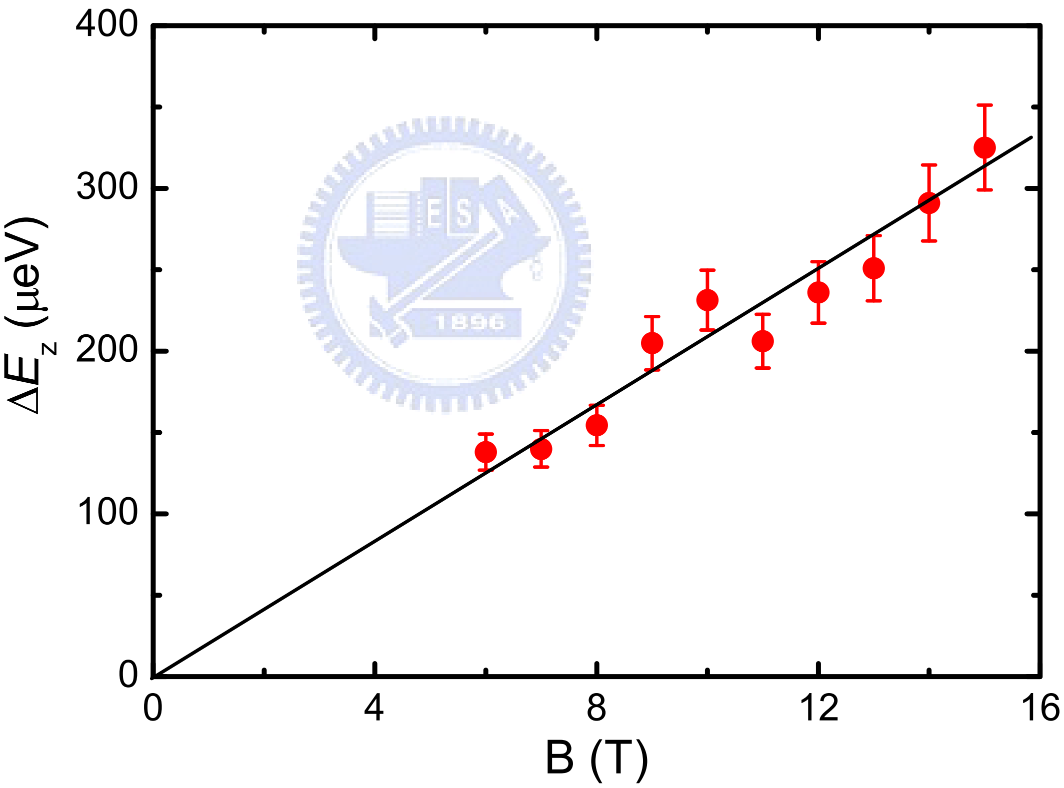

Figure 9.5: The extracted Zeeman energy as a function of magnetic fields.

D. Weinmann and co-workers(143) reported the spin blockade in linear and nonlinear transport through quantum dots. The transport properties of a quantum dot that is weakly coupled to leads are investigated by using the exact quantum states of a finite number of interacting electrons. The results show that, in addition to the Coulomb blockade, spin selection rules strongly influence the low temperature transport and lead to experimentally observable effects. Transition probabilities between states that correspond to successive electron numbers vanish if the total spins differ by $|\Delta S| > 1/2$. In nonlinear transport, this can lead to negative differential conductances. The linear conductance peaks are suppressed if transitions between successive ground states are forbidden.

Figure 9.6 shows the schematic of spin transition model. The x-axis is the magnetic filed and y-axis is the energy of right dot. There is only one electron in the right dot at low energy region and are two electrons in the right dot at higher energy region. In the $N_2 = 1$ case, two spin states, $|\uparrow>$ and $|\downarrow>$, are generate in the presence of magnetic field. In the $N_2 = 2$ case, there are three spin sub-levels,$|\uparrow\uparrow>$,$|\downarrow\downarrow>$, and $(|\uparrow\downarrow> -|\downarrow\uparrow>)/\sqrt{2}$, generate in the presence of magnetic field and one singlet state,$(|\uparrow\downarrow> -|\downarrow\uparrow>)/\sqrt{2}$. The energy of singlet state are lower than triplet states at low magnetic field and situation is opposite at high magnetic field. The energy of singlet state increases rapidly and becomes much higher than the triplet states after the magnetic field is high than the B_c.

Assuming that the $|\uparrow>$ is the initial state, only $|\uparrow\uparrow\rangle$, and $(|\uparrow\downarrow\rangle+|\downarrow\uparrow\rangle)/\sqrt{(2)}$ could be the final states. The transition from $|\uparrow\rangle$ to $|\downarrow\downarrow\rangle$ is forbidden because of the spin selection rule. The total spin difference between N-1 and N electrons cannot be more than 1/2. There are two transition processes for the initial $|\uparrow\rangle$ state, and the Zeeman energy difference is $g\mu_B B$

R. Hanson and co-workers(144) have measured the spin relaxation time of a single electron confined in a semiconductor quantum dot. They observed a lower bound at a spin relaxation time of 50 μs at 7.5 T. The relaxation time is longer than the electron tunneling time of 1 μs at 15 T in the $(1,1) \leftrightarrow (1,2)$ transport. The doublet transition is much slower than the tunneling; therefore, wether the initial state is $|\uparrow\rangle$ or $|\downarrow\rangle$, both electrons with spin up or spin down can tunnel through the dot before the spin relaxation occurs. Both $|\downarrow\rangle$ and $|\uparrow\rangle$ can be the initial states. As shown in Fig. 9.6, there are four transition processes which is indicted by blue lines. We should take care that although there are four possible

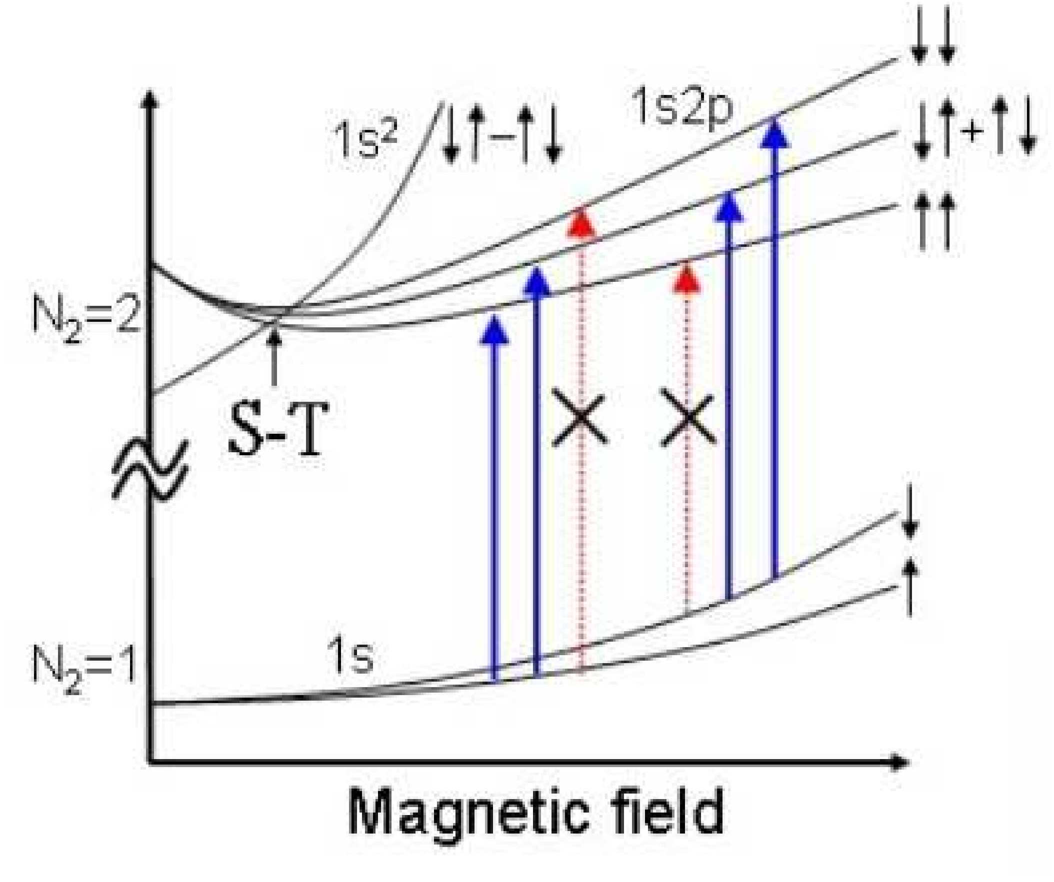

Figure 9.6: The schematic diagram of spin selection rule.

transitions but only two effective Zeeman splitting energies. The Zeeman splitting energy is $g\mu_B B$.

To confirm the accuracy of the result, we also measure the transport spectra of GaAs double quantum dots by the same method. Figure 9.7 shows the differential conductance as a function of source-drain voltage and gate voltage. We can observe two clear Zeeman sub-levels from the transition spectra of $Nt = 2 \leftrightarrow Nt = 3$. Figure 9.8 shows the extracted Zeeman energy, ΔE_Z. This result shows the Zeeman energy is almost linear with magnetic field and the effective $g = 0.25 \pm 0.02$, which agrees with literatures well.(137; 145)

The optical detection of conduction-electron spin resonance was previously performed in a bulk $\mathrm{In}_x\mathrm{Ga}_{1-x}\mathrm{As}$ system, where x ranges from 0 to 0.1. The measured g factor of pure bulk GaAs is -0.44, and the g factor decreases if Ga is replaced by In. The g factor of bulk $\mathrm{In}_{0.05}\mathrm{Ga}_{0.95}\mathrm{As}$ is -0.6.(146) It is often found that the absolute g value in confined electron systems is reduced from the bulk modulus.(130; 137; 144; 145) The ratio of the g factor of pure bulk GaAs to that of pure bulk $\mathrm{In}_{0.05}\mathrm{Ga}_{0.95}\mathrm{As}$ is 0.72, which is near the ratio of our confined quantum dots of 0.69. The results support that our measured g value is high accurate.

We measured the $(1, 1) \leftrightarrow (1, 2)$ electron transport state spectra of an $\mathrm{In}_{0.05}\mathrm{Ga}_{0.95}\mathrm{As}$ vertical double quantum dot by a large-source-drain-voltage method. A spin singlet-triplet transition is observed at 5 T, followed by the observation of two clear Zeeman splitting lines at magnetic fields higher than 5 T. Zeeman splitting energies are linear with magnetic fields up to 15 T. Doublet spin relaxation is much slower than electron tunneling; therefore, both $|\uparrow>$ and $|\downarrow>$ can be the initial electron states. On the basis of the spin selection rule, the transitions $|\uparrow>\rightarrow|\downarrow\downarrow>$ and $|\downarrow>\rightarrow|\uparrow\uparrow>$ are forbidden, because the total spin difference between the initial and final states is larger than 1/2. There are four transitions in tunneling processes, but only two energy differences lead to the two Zeeman sublevels in the obtained excitation spectrum.(147)

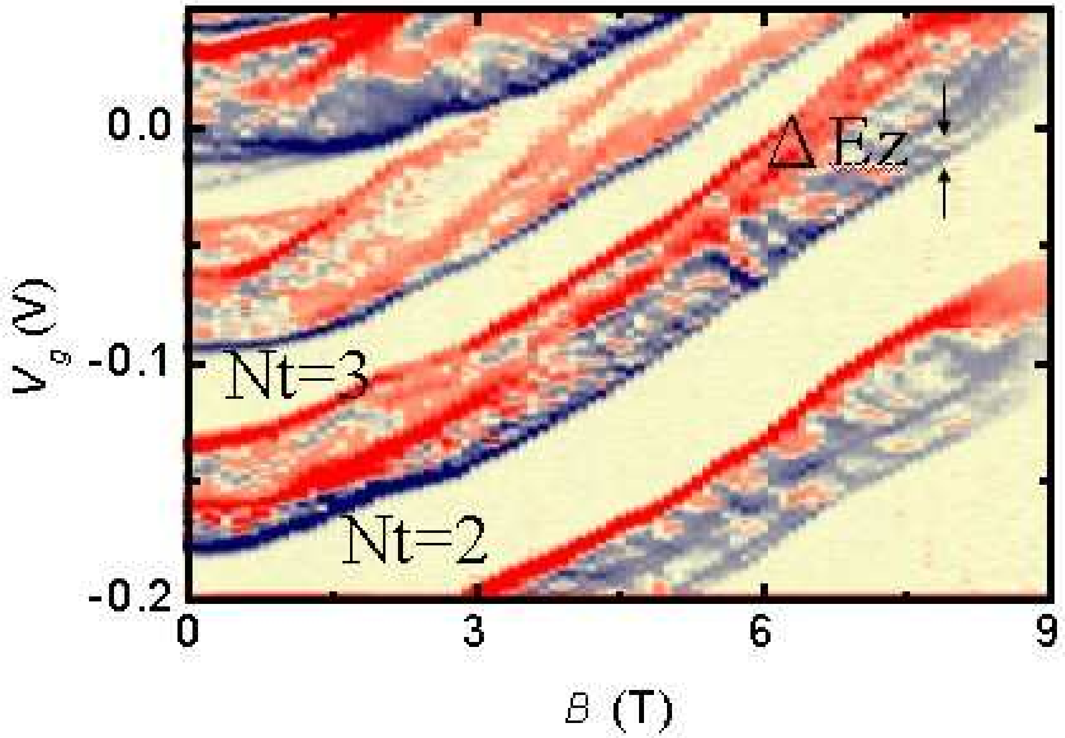

Figure 9.7: The differential conductance of GaAs as a function of source-drain voltage and gate voltage.

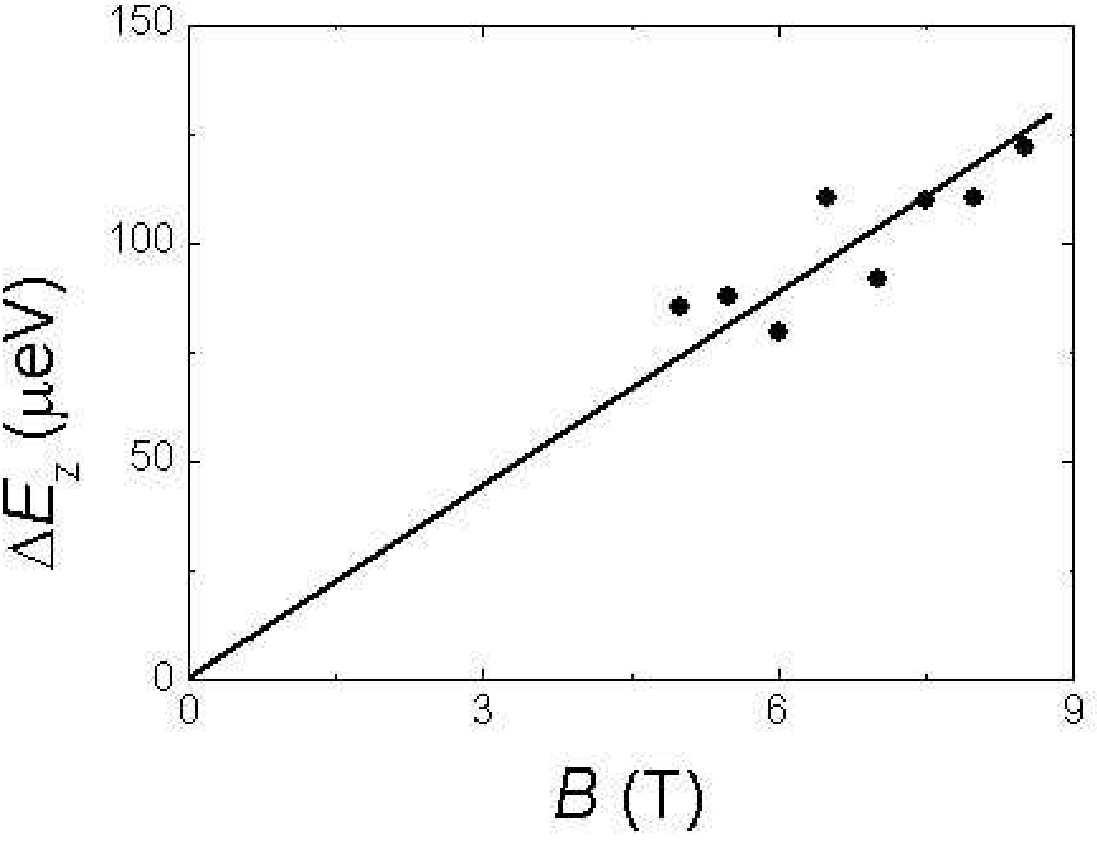

Figure 9.8: The extracted Zeeman energy of GaAs as a function of magnetic field.

9.3 Spin Transport in Double Quantum Dots with Zeeman Mismatch

The study and control of electron spins is gaining increasing attention, because of potential applications in quantum information and spintronic devices.(125; 148) For the implementation of quantum information processing, there are two crucial requirements: fast and coherent control of individual spins and controlled exchange coupling with the environment.(124; 149) For example, nuclear spins are manipulated with the use of a combination of static and radio-frequency magnetic fields and one can rotate electron spins arbitrarily.(150) There are several approaches for controlling spin-based quantum information in semiconductors. Because of easy operation and fast tuning, electric-field control of the electron's g-factor has been achieved. Application of an electric field across the heterostructure leads to a displacement of the electron's wavefunction in the quantum well, and hence gate-voltage-mediated control of coherent spin precession was demonstrated.(151) Gigahertz-frequency voltage control and optical detection of the electron spin in a capacitively gated heterostructure semiconductor has also been demonstrated.(152)

Early reports suggested that the quantum information process can be reached in the use of electrical gates to bring electrons into contact with an inhomogeneous magnetic field or an inhomogeneous g-factor environments.(124; 149) It is a challenge to create a inhomogeneous magnetic field through two quantum dots. Recently, inhomogeneous magnetic field between two neighboring quantum dots is proposed in electric dipole spin resonance experiment.(103) However, the technics are not easy. In contrast to create an inhomogeneous an inhomogeneous magnetic field through a small area it is much easier to engine g factors in double quantum dots. A double quantum dots with different g factors in presence of homogeneous magnetic field is equal to the environment with inhomogeneous magnetic field.

It is known that spin up and spin down states are always on site at the same time in quantum dots with the same g factor. In quantum dots with different g factors, the tunneling processes are expected as only spin-up states resonance, spin-down states resonance, or spin blockade by suitable tuning source-drain voltage and gate voltage. The behavior of the tunneling is much more complicated and not yet studied. In the letter, we report electron tunneling in a vertical double quantum dots with different g-factors.

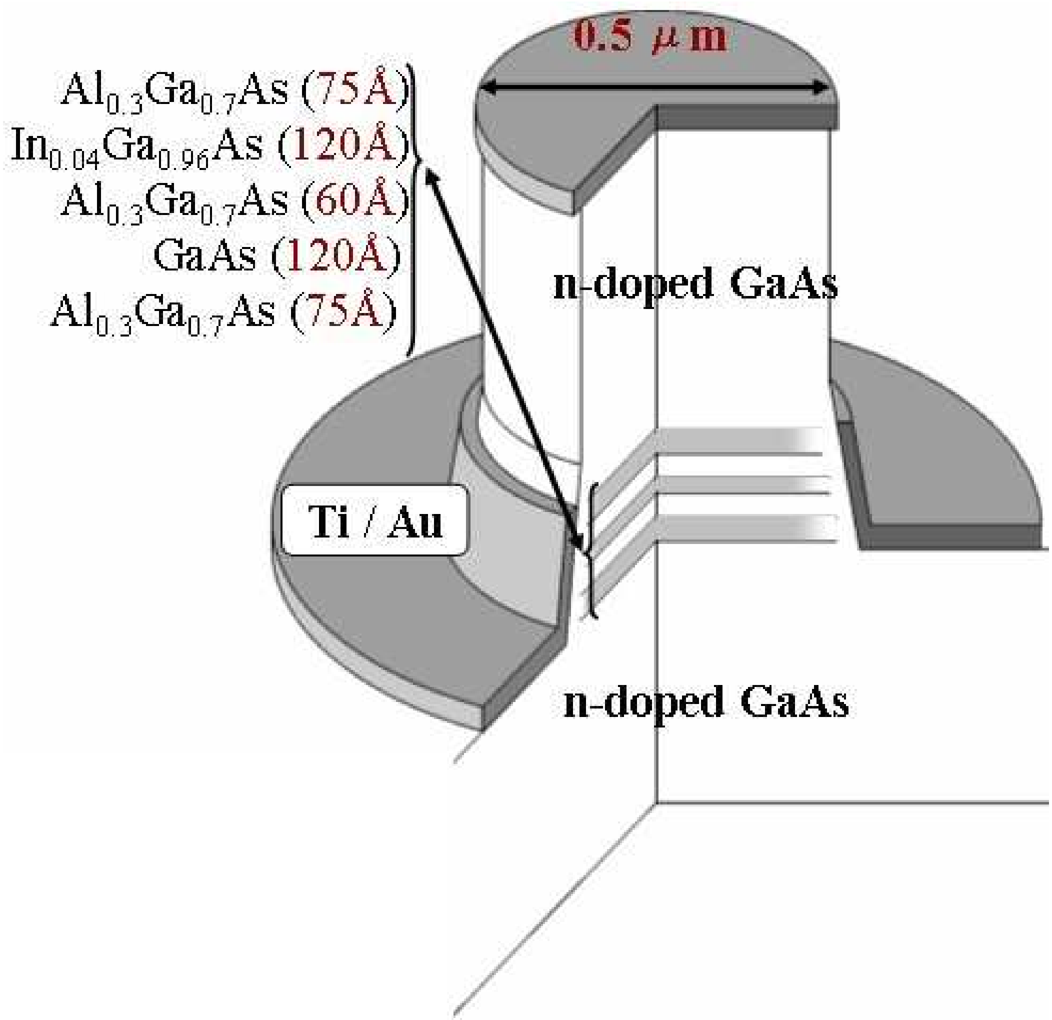

Figure 9.9: The structure of vertical double quantum dots with different g factors.

The vertical double quantum dots is fabricated by the standard processes. The figure 9.9 shows our quantum dots structure. Two quantum dots locate between $Al_{0.03}Ga_{0.97}As$ heterostructure barriers and were surrounded by metal gate electrode. From bottom to top, the dots consist of 100Å $Al_{0.03}Ga_{0.97}As$,

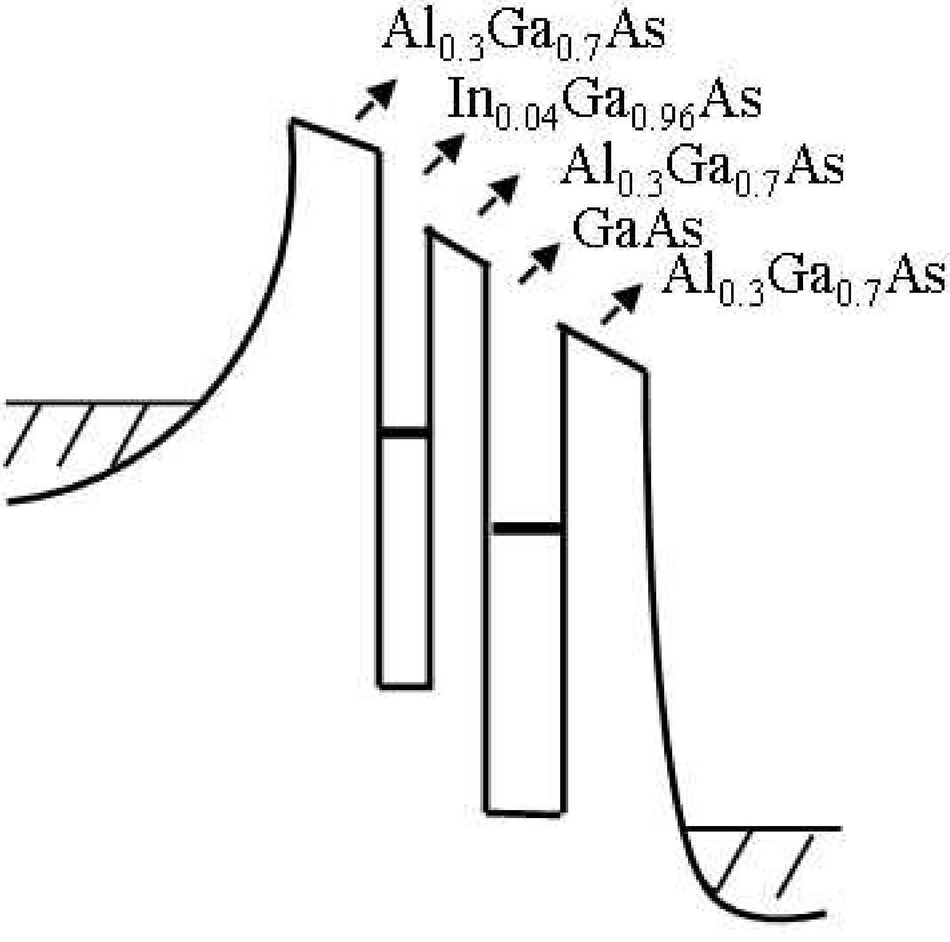

Figure 9.10: The schema of the potential barrels of the dots.

100Å GaAs, 65Å $Al_{0.03}Ga_{0.97}As$, 75Å $In_{0.04}Ga_{0.96}As$, 100Å $Al_{0.03}Ga_{0.97}As$. The geometric barrier potential high is also shown in Fig. 9.10. Measurements were performed in a dilution refrigerator at 20 mK and up to 15 T magnetic fields perpendicular to heterostructure. The effective electron temperature is about 100 mK which is known from Coulomb blockade width.

Figure 9.11 shows the differential conductance, dI_{SD}/dV_{SD}, as a function of source-drain voltage and gate voltage. The "non-closed" Coulomb diamond is always observed in weakly coupled doublet dot structure with energy offset.(114; 153; 154) "Bottom-line" of the Coulomb diamond defines the current threshold for the sequential tunneling from $N = 0$ region. By appropriately tuning side gate voltage, V_g, and source-drain voltage, V_{SD}, electron number in the left dot is always one or zero and the left dot acts as a turnstile.(121) The arrows in Fig. 9.11 mark several tunneling peaks where electrons from left dot elastically tunnel to different states of right dot. As shown in Fig. 9.12, there are two tunneling lines, L1 and L2, at low bias region. Besides the resonance tunneling transition, L1, there is an other high order tunneling transition, L2, in which electrons directly tunnel through the left dot to the states of right dot, even though the states of left dot are not within the transport window.(139) In this co-tunneling process, the current is much weaker than resonance tunneling. The slopes of the tunneling lines indicate ratios of voltage drop across respective barrel to applied source-drain voltage. The experimental results show that the voltage drop ratio of first barrel to second barrel is 0.5.

Stoof and Nazarov give a detailed description of photon assisted tunneling in a double quantum dot. The basic idea is that electrons can absorb fixed quanta of energy hf from a classical oscillating field. An as voltage drop $V = V_{ac}cos(2\pi ft)$ across a tunnel barrier modifies the tunnel rate through the barrier as

$$\tilde{\Gamma}(E) = \sum_{n=-\infty}^{\infty} J_n^2(\alpha)\Gamma(E + nhf) \tag{9.1}$$

where $\tilde{\Gamma}$ and Γ are the tunnel rates at energy E with and without an ac voltage, respectively. $J_n^2(\alpha)$ is the square of the n^{th} order Bessel function evaluated at $\alpha = \frac{eV_{ac}}{hf}$, which describes the probability that an electron absorbs or emits n photons of energy hf.

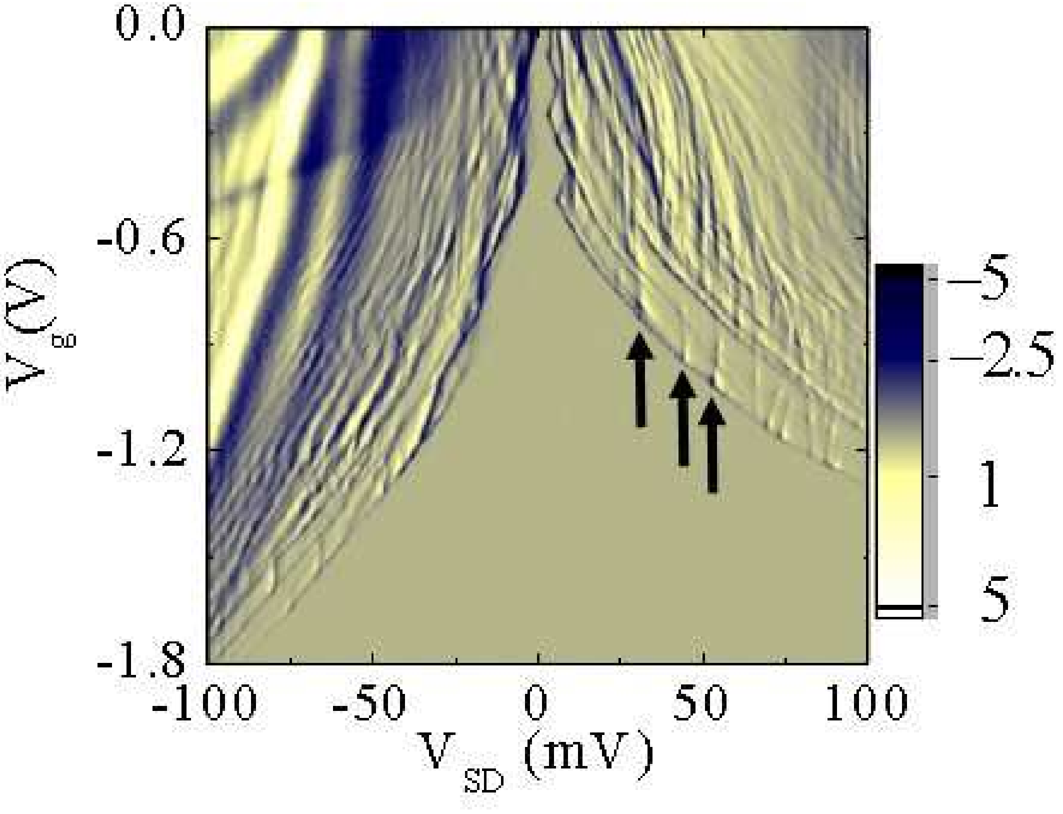

Figure 9.11: Differential conductance, dI_{sd}/dV_{sd}, as a function of source-drain voltage and gate voltage. The arrows mark the resonance tunneling peaks of from ground state of left dots to different states of right dot.

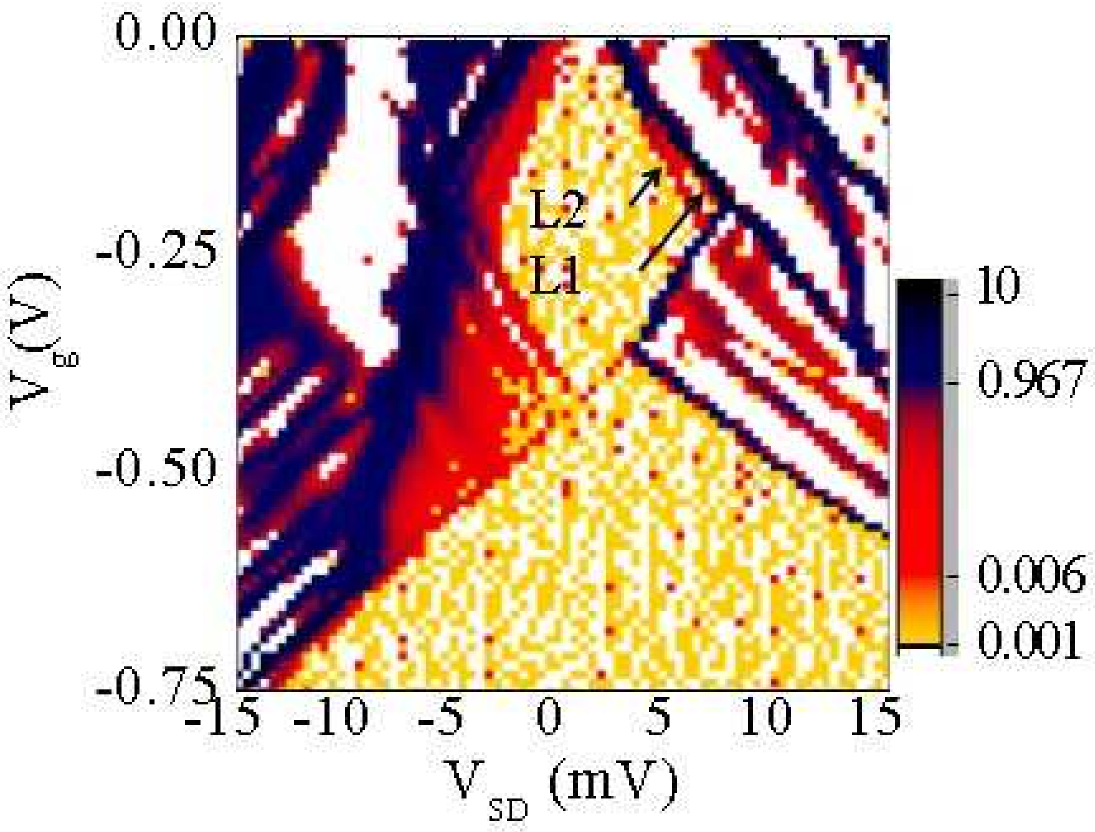

Figure 9.12: Resonance tunneling and co-tunneling peaks.

Figure 9.13 shows differential conductance of chose inter-dot tunneling at high bias region. The "bottom-line", L3, is transition peak from ground state of left dot to right dot state. Because of decreasing of carrier concentration in source reservoir at high bias, the slope of L3 is half of L1. Figure 9.14 shows the photon-assisted tunneling spectrum along the arrow shown in Fig. 9.13. The applied power intensities are from 0 dBm up to -15 dBm and the microwave frequency is 39.327 GHz. Each curve has been consecutively shift up by a constant value. The current through the system vs source-drain voltage consists of a series of peaks corresponding to photon-assisted tunneling between two dots.(155) The source-drain voltage difference between two neighboring absorption (emission) resonance peaks is 0.836 mV. It deduces that the α factor, the ratio of source-drain voltage to gate voltage, between two dots is 0.193, α_2, and between source and left dot is 0.1, α_1.

In a system of quantum dots with the same g factor, it is always one resonance peak because both spin states are on site at the same time. Considering a double quantum dots system with different g factors, the tunneling is much more complicated. The single tunneling peak splits into two peaks due to mismatch of Zeeman splitting of two dots. The tunneling current depends both on relative position of the states of two dots and the strength of coupling with environment. In the limit of weak coupling with environment, the tunneling takes place only when spin-up states on site, no other peaks appear due to either spin up or spin down blockade. In the appearance of phonon (and/or photon) coupling, it is expected that two resonance peaks, spin up and spin down resonance tunneling, appears and the energy splitting of the two peaks equals to the Zeeman energy difference of the two dots. In the limit of strong coupling, the current is dominated by the barrier that is the same as the case of quantum dots with the same g factor.

Assuming that Zeeman splitting in the left dot is larger than that in the right dot and neglecting high order tunneling processes. As shown in Fig. 9.15, by appropriate tuning V_{SD} and V_g, it is expected different tunnelings dominate different regions. First of all, two parallel tunneling lines, Z_1 and Z_2 which are the Zeeman splitting lines of left dot are observed.(137) The difference of Zeeman energy of two dots does not affect the appearance of this two lines. Besides, as shown in Fig. 9.16, there are several distinctive lines A, B,C, and

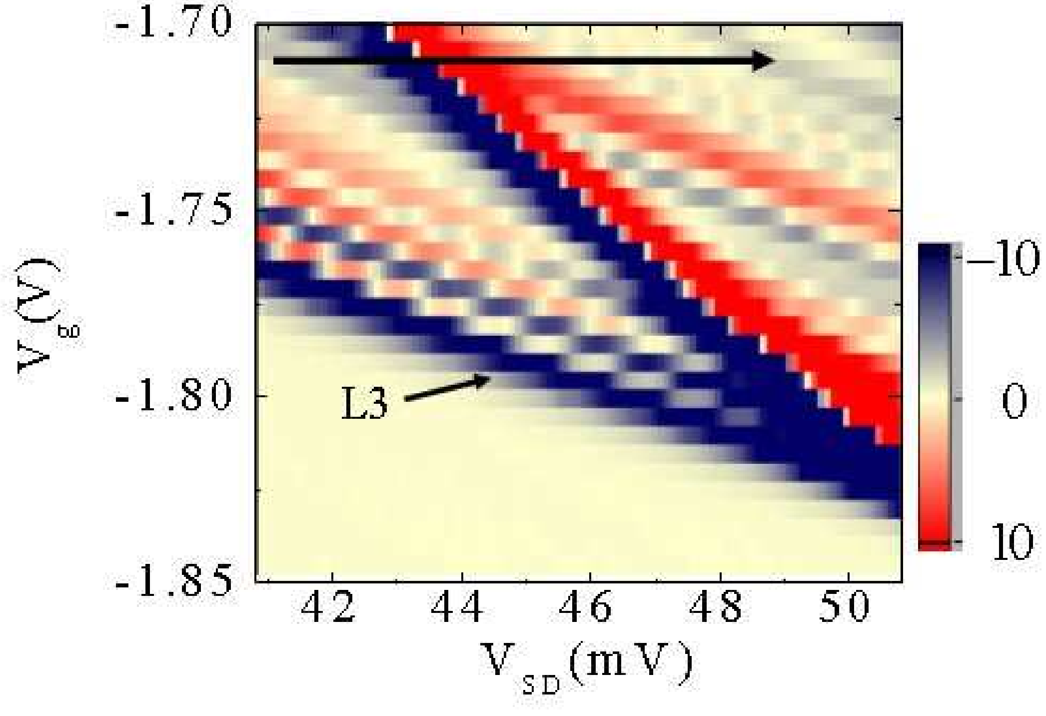

Figure 9.13: The inter-dot tunneling peak of chose state.

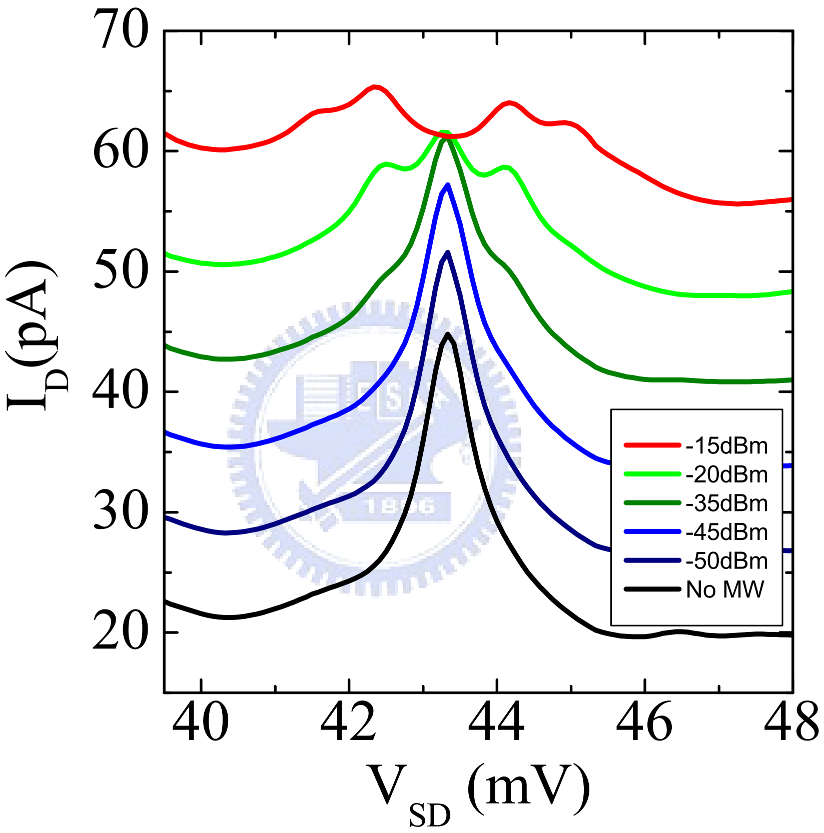

Figure 9.14: The current through the system vs source-drain voltage consists of a series of peaks corresponding to photon-assisted tunneling line between two dots.

D. The schema A $\sim$ schema D show he respective tunneling processes. Schema A shows spin up states line up and only electrons with spin up could do the resonance tunneling. However, in the schema B, even though spin down states line up, Coulomb blockade takes place because the spin down states are not in the transport window. On the other hand, in the schema C and D, both spin up and spin down states of the two dots are within the transport window. In the schema C, the spin up states line up, and electrons with spin up could tunnel through the dots resonantly. On the contrast, although spin down states of both two dots are also within the transport window, it is not on-site. Once, electrons with spin down enter the state of the left dot, spin blockade occurs. A phonon emission is necessary for spin down electrons of left dot to release extra energy to tunnel to the spin down states of right dot. The current of the schema C depends on the phonon-assisted relaxation time. Similar to schema C, in schema D, although spin down states are line up, it would be blockade once spin up electrons occupy the left dot. Spin-up electrons need absorbing energy tunneling to right dot. Phonon absorbing time dominates the tunneling process. The phonon-assisted times are critical time scales for these two tunneling processes. It is well known that the phonon emission time is often shorter than phonon absorbtion time. Therefore, it is expected that the current at $A \geq C \geq D \geq B$.

T. Fujisawa and co-workers, studied the phonon mission assisted relaxation time. Their results deduce that the energy relaxation time from $2P$ state to $1S$ state is 10ns at 1 T and they predict that the energy relaxation time between Zeeman splitting states is larger than 1 ms at 5 T and larger than 100 μs at 9 T.(126) It indicates that the current due to phonon-assisted tunneling is order of fA.

Figure 9.17 $\sim$ Fig. 9.20 show the experimental results of differential conductance, dI_{sd}/dV_{sd}, as a function of source-drain voltage and gate voltage at several different magnetic fields. There are two characteristic splitting energies, δ_1 and δ_2, where δ_1 is Zeeman splitting energy of left dot and δ_2 is characteristic energy of inter-dots tunneling.(121; 137) As discussed above, the α_1 and α_2 connect the gate voltages to the splitting energies. As shown in Fig. 9.21 and Fig. 9.22, the two splitting energies are both linear with magnetic fields. The results show the

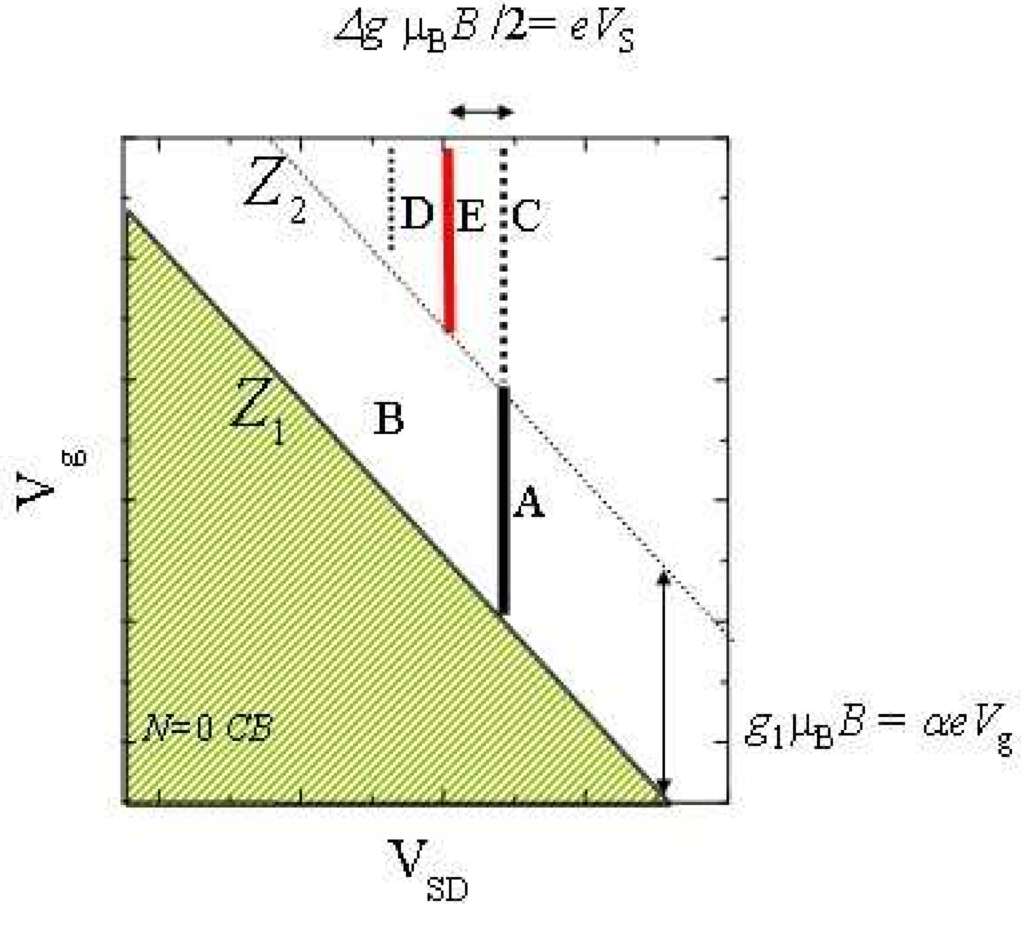

Figure 9.15: Splitting of tunneling peak due to Zeeman mismatch.

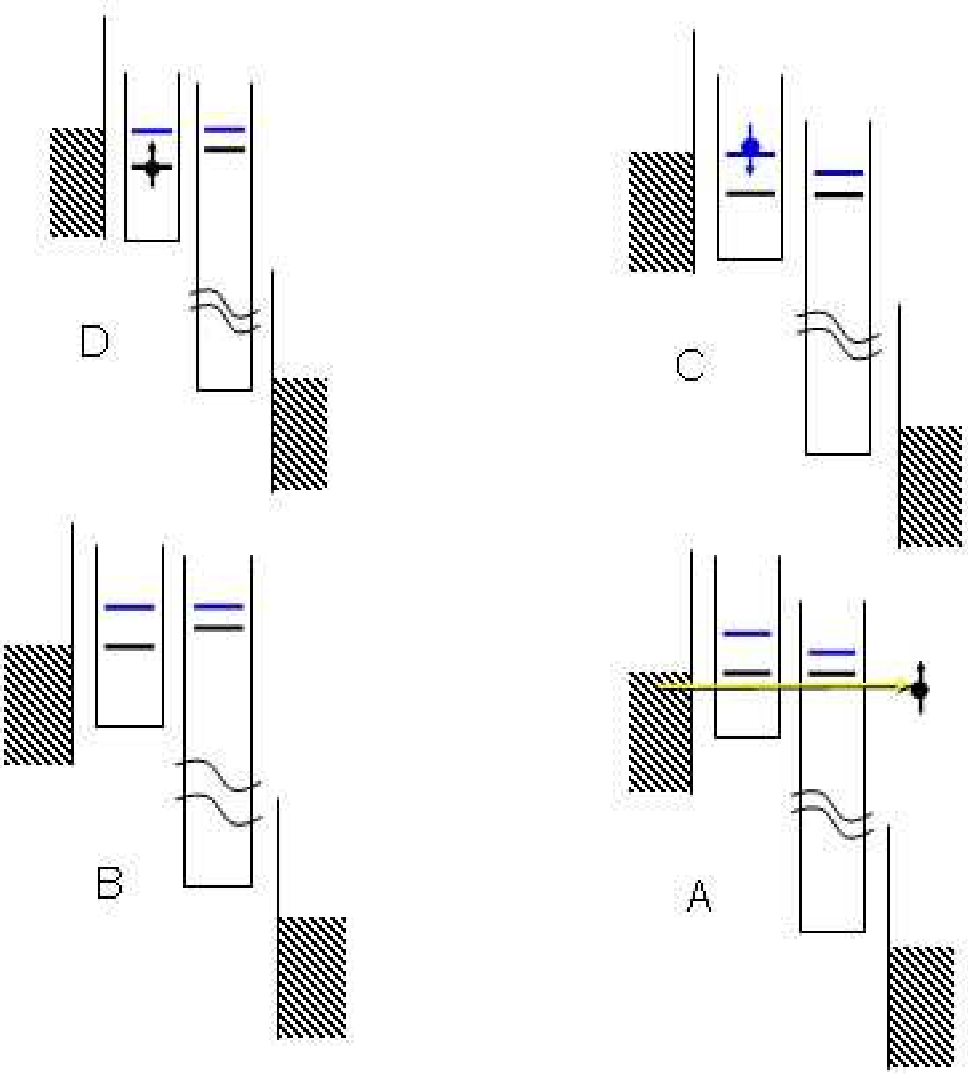

Figure 9.16: The respective Schematic figures of tunneling peak due to Zeeman mismatch.

resonant tunneling time is about 10 ns which is much short than the phonon-assisted relaxation time. It indicates that the barriers dominate over the phonon assisted effect. The system is in the limit of the weak phonon coupling.

Recently, Y. Tokura evaluates the resonant tunneling current via series quantum dots by Bloch equation and finds that the resonant current is always singly peaked whose peak bias condition depends on the gate voltage.(156; 157) Table 1 shows current peaks and full width at half maximum (FWHM) in two cases. Case A is that only spin up state of let dot is within transport window and case B is that both spin up and down states of left dot are within transport window. For a weak tunneling region, $\Omega \ll \gamma_L, \gamma_R$, the peak current in case A is much larger than current in the case B. For strong tunneling region, the peak current saturates and current in case B is about 10% larger than current in case A. On the other hand, for a weak tunneling region, FWHM in case A is smaller than in case B. By increasing Ω, the FWHM increase almost linearly. For strong tunneling region, the FWHM are almost the same for case A and case B.

In our results, the effective FWHM of the tunneling peaks are about 0.1 meV which are 1 order larger than thermal noise and the FWHM are mainly controlled by bandwidths of coupling. $\Omega^{-1}+\gamma_L^{-1}$ is about 4.6×10^{-2} ns which is much shorter than γ_R^{-1} which is about 10 ns. Based on the prediction of the theory, both of the current values and FWHM are about 10% different in two cases and this is consistent with our experimental results.

The theory deduces that the current peak positions for two cases are independent of gate voltage for a given region.(157) When gate voltage increase from case A to case B, the current peak position shifts by $(E_{ZL} - E_{ZR})/2$, which is equivalent to the shift in source-drain voltage by $(E_{ZL} - E_{ZR})/(4e\eta)$. E_{ZL} (E_{ZR}) means the Zeeman energy of left (right) dot and e is the electron charge. 2η means the ratio of voltage drop between two dots to source-drain voltage which is 0.193 in this experiment.

Figure 9.21 and Fig. 9.22 show the extracted δ_1 and δ_2 as function of magnetic field. The δ_1 and δ_2 respectively mean the Zeeman energy of left dot and Zeeman mismatch energy. The results show that the g factor of left dot ($\mathrm{In}_{0.04}\mathrm{Ga}_{0.96}\mathrm{As}$) is 0.89 and the g factor difference of two dots is 0.56. It deduces that the g factor of right dot (GaAs) is 0.33. This large g factor of GaAs only was observed in

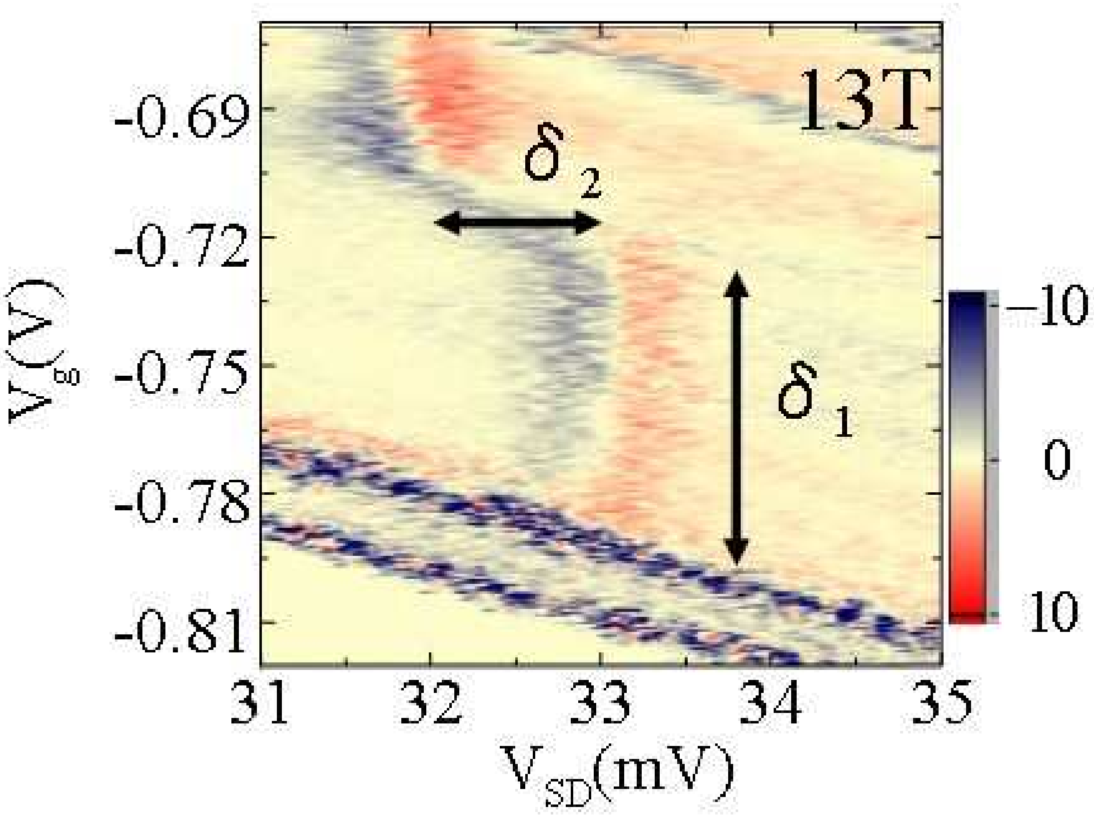

Figure 9.17: The measured results of differential conductance at 13 T.

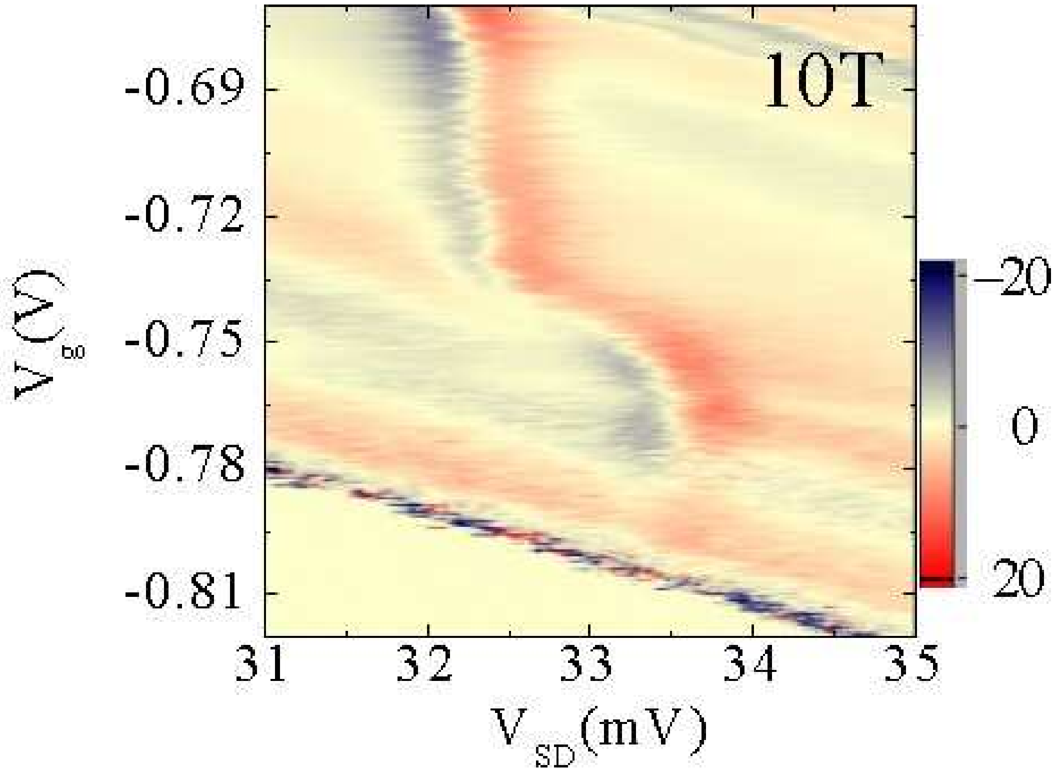

Figure 9.18: The measured results of differential conductance at 10 T.

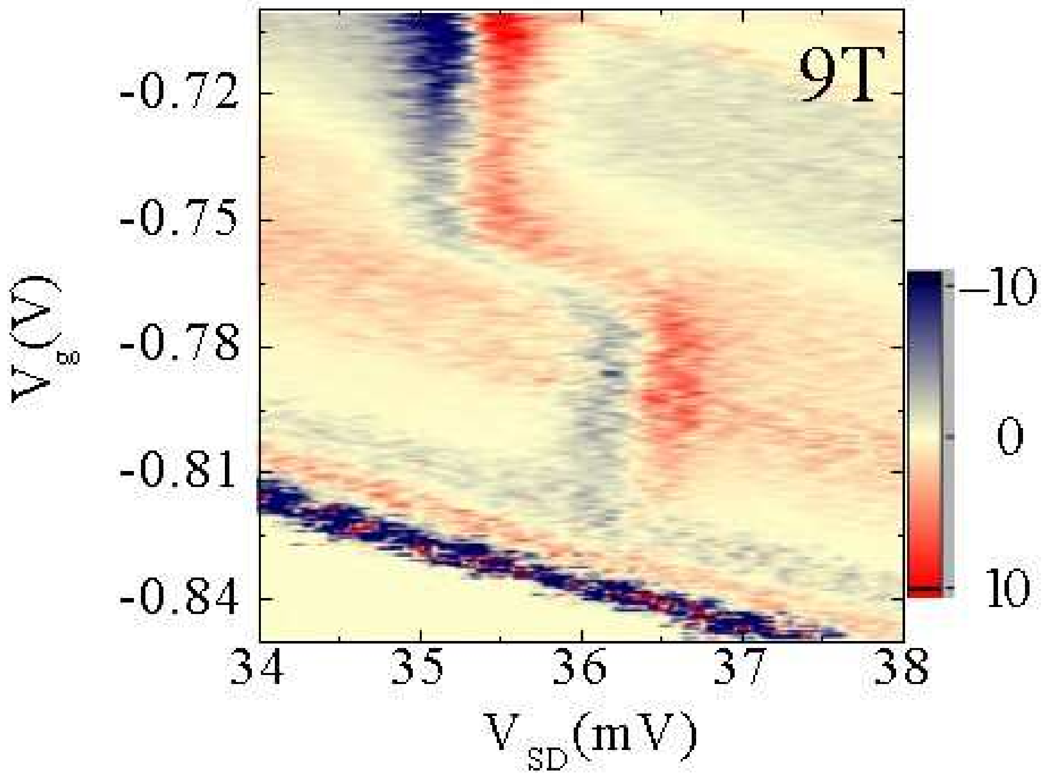

Figure 9.19: The measured results of differential conductance at 9 T.

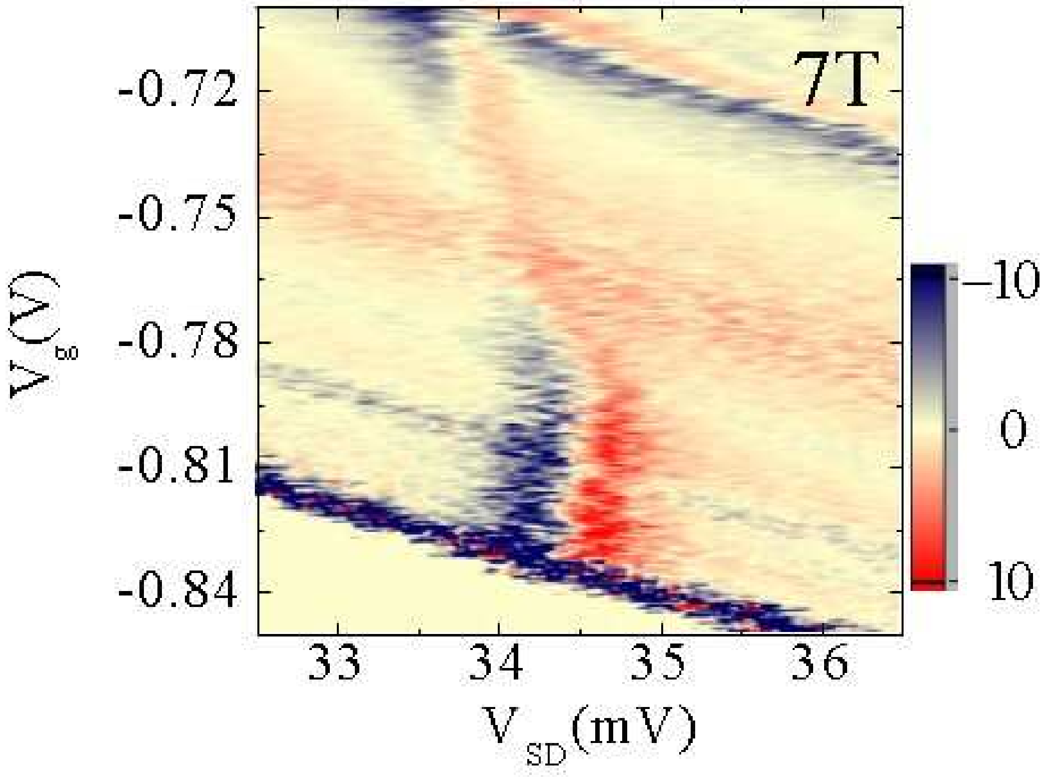

Figure 9.20: The measured results of differential conductance at 7 T.

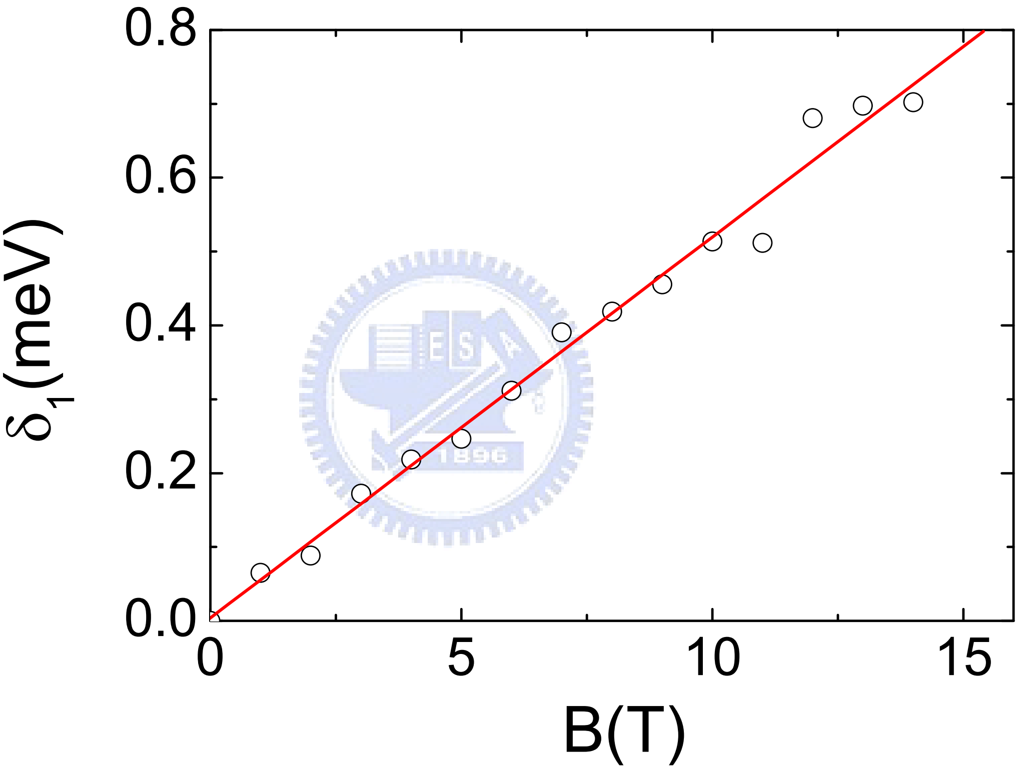

Figure 9.21: The extracted Zeeman energy, δ_1.

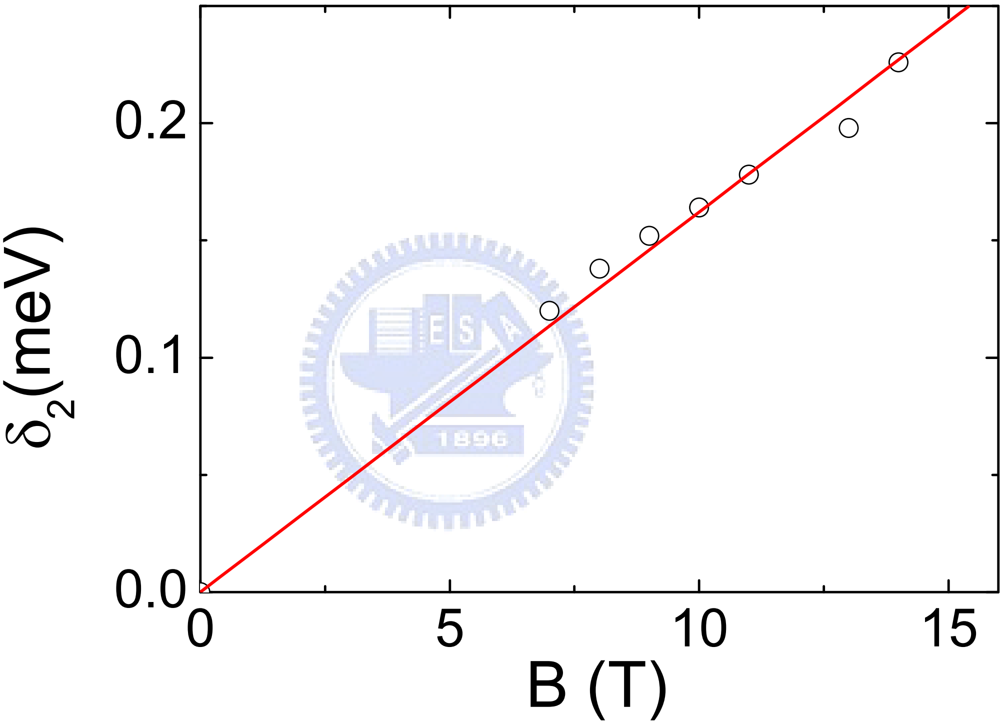

Figure 9.22: The extracted Zeeman energy, δ_2.

the recent experiments.(103) Weisbuch and co-workers studied g factor of Bulk $\mathrm{In}_x\mathrm{Ga}_{1-x}\mathrm{As}$ where x ranges from 0 to 0.1. The results show that g factor is -0.44 for GaAs and -0.779 for $\mathrm{In}_{0.09}\mathrm{Ga}_{0.91}\mathrm{As}$.(158) While increasing 1% In, the g factor would decrease 0.0376. It seems that the observed large g factor, -0.89, would correspond to g factor of $\mathrm{In}_{0.11}\mathrm{Ga}_{0.89}\mathrm{As}$. Possible reasons might be from the reports of highly nonuniform composition distribution with an In-rich core in $\mathrm{In}_{0.5}\mathrm{Ga}_{0.5}\mathrm{As}$ alloy quantum dots or size dependence effect of quantum well.(159; 160)

Creating a non-uniform magnetic field between two quantum dots is a step to realize quantum information processing and this is achieved recently in EDSR experiment.(103; 124; 149) However, the associated splitting energy is small and technics are difficult. A vertical double quantum dots with different g factors is equal to the non-uniform magnetic field through two quantum dots and it is much easier to achieve in experiment. The tunneling current is measured in the inhomogeneous g factor quantum dots. The tunneling currents strongly depend on the coupling strength with phonon. In the weak coupling case, phonon-assisted relaxation time is too long that only the resonance tunneling of spin-up states is observed and the Zeeman mismatch peaks are not observed. The bandwidth resonance tunneling current through the system is also observed. The results show that the peak shifting between only one Zeeman sublevel within the transport window and both two Zeeman sublevels within the transport window is half of Zeeman energy difference.

Chapter 10

Conclusions and Future Works

We studied two topics in mesoscopic transport. First one is about the low temperature electron dephasing time and second one is about the spin transport in vertical quantum dots.

In the topic of low temperature dephasing time, we have studied the low temperature dephasing time in $Cu_{93}Ge_4Au_3$ thin films (~ 200 Å) with different levels of disorder. The results show that the electron-phonon inelastic scattering dominates the dephasing rates above 10 K. The scattering times are inverse proportion to square of temperature, $\tau_\varphi \sim AT^{-2}$. A is 0.53 ± 0.1 nsec K^2 and independent of levels of disorder. The dephasing times are a constant values between 10 K and 5 K and it is the same for all samples. From the analysis of the concentration of magnetic impurities and temperature dependent resistances at high magnetic field, it indicates that the plateau is not from the Kondo effect. The most distinctive phenomenon is that the dephasing times below 5 K increase as temperature decreasing and the dephasing increasing rates depend on levels of disorder. The $\tau_\varphi \propto T^{-0.5}$ for the most disordered film and dephasing time is almost no increasing for the weakest disordered film. The well studied electron-electron inelastic scattering rate is 2 orders weaker than our results and the Kondo effect can not explain the sample dependent scattering rate. The measured temperature dependent dephasing times do not agree with the prediction of Kondo effect. On the other hand, resistances are also measured. All of the films show that resistances increase logarithmically from 10 K down to 30 mK and are insensitive to magnetic field up to 15 Tesla. Moreover, this behavior does not dependent on the dimensionality of samples. All of the results support that the less studied dynamic structure defeat scattering dominates the behavior of the system.

In the topic of spin transport in vertical quantum dots, we have studied two subjects. First one is about spin selection rule and the second one is about spin tunneling in Zeeman mismatch doublet quantum dots.

In the subject of spin selection rule, we measured the transport spectrum of $(1,1) \leftrightarrow (1,2)$ in $\mathrm{In_{0.05}Ga_{0.95}As}$ and GaAs vertical double quantum dots, where $(N(L), N(R))$ mean the electron number in left dot and right dot respectively. At low magnetic field, the ground state of 2 electron system is 1S2. Two electrons occupy the 1S state with anti-parallel spins. We observe spin singlet-triplet transition at 5 Tesla which is the same with the literatures. The triplet states become ground state when magnetic field is higher than 5 Tesla and the energy of singlet state increases drastically. We observe two Zeeman sublevels instead of three Zeeman sublevels for triplet at magnetic field from 6 Tesla to 15 Tesla. Spin selection rule predicts that the total spin difference between N electrons and N+1 electrons can not be larger than 1/2. Assume that the initial spin state is spin up, the transitions from the state of $|\uparrow>$ to the states of $|\uparrow\uparrow>$ and $(|\uparrow\downarrow> + |\downarrow\uparrow>)/\sqrt{2}$ are allowed, but the transition from the state of $|\uparrow>$ to the state of $|\downarrow\downarrow>$ is forbidden. The measured result shows that the tunneling rate is about 1νs which is much short than the relaxation time, which is longer than 50νs, from state of spin down to spin up. It means that the state of spin down also can be the initial state. The transitions from the state of $|\downarrow>$ to the states of $|\downarrow\downarrow>$ and $(|\uparrow\downarrow> + |\downarrow\uparrow>)/\sqrt{2}$ are allowed, but the transition from the state of $|\downarrow>$ to the state of $|\uparrow\uparrow>$ is forbidden. There are totally four possible transport processes contributing to the spectrum. However, the adding energy of from $|\uparrow>$ to $(|\uparrow\downarrow> + |\downarrow\uparrow>)/\sqrt{2}$ is equal to that from $|\downarrow>$ to $|\downarrow\downarrow>$ and the adding energy of from $|\uparrow>$ to $|\uparrow\uparrow>$ is equal to that from $|\downarrow>$ to $(|\uparrow\downarrow> + |\downarrow\uparrow>)/\sqrt{2}$. There are four transition processes, but only two energy values could be observed. The results show that the g factors are 0.36 ± 0.02 and 0.25 ± 0.02 for $\mathrm{In_{0.05}Ga_{0.95}As}$ and GaAs respectively.

In the subject of spin tunneling in Zeeman mismatch double quantum dots. The tunneling behavior has been well studied in double quantum dots with the same g factors for two dots. The spin-up states and spin-down states are always on-site at the same time, so only one resonance tunneling peak would appear. In the double quantum dots with different g factors for two dots, the spin-up states and spin-down states would not line up at the same time. By appropriately tuning the respective position of energy states of two dots, it is expected that two resonance tunneling peaks appear and the distance of two peaks is equal to the difference of Zeeman energies of two dots. Further analysis the system, we found that the phonon-assisted relaxation dominate the tunneling processes. The phonon-assisted relaxation time is so long that make it is difficult to observe the splitting of two Zeeman mismatch peaks. Only the resonance tunneling peak of spin-up is observed. Instead of the splitting of two Zeeman mismatch peaks, we observe the bandwidth tunneling peak in the Zeeman mismatch system. The results show that the position of bandwidth tunneling peak depends on the states which is within the transport window. Two splitting peaks are observed in the experiments and the distance of the two peaks is equal to half of difference of two Zeeman energies.

In the first part of my future work, I plan to continuous the previous work and make a full understanding of the spin transport through mismatch spin states. Second, we also plan to study the photon-assisted resonant tunneling by using microwave. The understanding of the influence of external microwave helps us analysis and know the potential transport processes. It also helps us to know another crucial problem, the coherence time of spin entanglement. Combine these two parts, the results would make us understand the spin transport a lot and further realize the quantum computing in the future.

Reference

[1] P. W. Anderson. *Phys. Rev.*, **109**:1492, 1958. 3, 9

[2] D. J. Thouless. *Phys. Rep.*, **13C**:93, 1974. 4

[3] D. J. Thouless. *Phys. Rev. Lett.*, **39**:1167, 1977. 4

[4] J. T. Edwards and D. J. Thouless. *J. Phys. C.*, **5**:807, 1972. 4

[5] D. C. Licciardello and D. J. Thouless. *Phys. Rev. Lett.*, **35**:4159, 1975. 4

[6] D. C. Licciardello E. Abrahams, P. W. Anderson and T. V. Ramakrishnan. *Phys. Rev. Lett.*, **42**:673, 1979. 4

[7] B. L. Altshuler and A. G. Aronov. *Solid State Commun.*, **36**:115, 1979. 4

[8] B. L. Altshuler and A. G. Aronov. *Sov. Phys. JETP*, **50**:968, 1979. 4, 60

[9] A. G. Aronov B. L. Altshuler and P. A. Lee. *Phys. Rev. Lett.*, **44**:1288, 1980. 4, 5

[10] A. I. Larkin B. L. Altshuler, D. Khmel'nitzkii and P. A. Lee. *Sov. Rev. B*, **22**:5142, 1980. 4, 5

[11] P. Chaudhari and H. U. habermeier. *Phys. Rev. Lett.*, **44**:40, 1980. 4, 8

[12] G. J. Dolan and D. D. Osheroff. *Phys. Rev. Lett.*, **43**:712, 1979. 4

[13] N. Giordano. *Phys. Rev. B*, **22**:5635, 1980. 4

[14] W. Gilson N. Giordano and D. E. Prober. *Phys. Rev. Lett.*, **43**:725, 1979. 4

[15] A. I. Larkin S. Hikami and Y. Nagaoka. *Prog. Theor. Phys.*, **63**:707, 1980. 5

[16] B. L. Altshuler and A. G. Aronov. *JETP Lett.*, **33**:499, 1981. 5

[17] G. Bergmann. *Phys. Rep.*, **107**:1, 1984. 5, 14

[18] M. E. Gershenzon B. L. Al'tshuler, A. G. Aronov and Yu. V. Sharvin. *Sov. Sci. Rev. A*, **9**:223, 1987. 5

[19] G. Bergmann. *Phys. Rev. Lett.*, **43**:1357, 1979. 5

[20] G. Bergmann. *Solid. State. Commun.*, **42**:815, 1982. 5

[21] G. Bergmann. *Phys. Rev. Lett.*, **48**:1046, 1982. 5

[22] G. Bergmann. *Phys. Rev. B*, **28**:515, 1983. 5

[23] T. Ootuka S. Kobayashi, F. Komori and W. Sasaki. *J. Phys. Soc. Jpn.*, **54**:3018, 1985. 5

[24] G. Bergmann. *Phys. Rev. Lett.*, **49**:162, 1982. 5

[25] G. Bergmann. *Phys. Rev. B*, **25**:2937, 1982. 5

[26] G. Bergmann. *Phys. Rev. B*, **28**:2914, 1983. 5

[27] J. J. Lin and N. Giordano. *Phys. Rev. B*, **33**:1519, 1986. 5

[28] J. J. Lin and N. Giordano. *Phys. Rev. B*, **35**:545, 1987. 5

[29] J. J. Lin and C. Y. Wu. *Phys. Rev. B*, **48**:5021, 1993. 5, 64

[30] J. J. Lin and C. Y. Wu. *Europhys. Lett.*, **29**:141, 1995. 5, 64

[31] J. J. Lin and C. Y. Wu. *Physica B*, **68**:219, 1996. 5, 64

[32] A. C. Ehrlich B. J. Dalrymple, S. A. Wolf and D. J. Gillespie. *Phys. Rev. B*, **33**:7514, 1986. 5

[33] S. Friendrichowski and G. Dumpich. *Phys. Rev. B*, **58**:9689, 1998. 5

[34] R. S. Germain R. C. Richardson M. L. Roukes, M. R. Freeman and M. B. Ketchen. *Phys. Rev. Lett.*, **55**:422, 1985. 5

[35] R. P. Peter and G. Bergmann. *J. Phys. Soc. Jpn.*, **54**:3478, 1985. 5

[36] M. Yu. Reizer and A. Y. Sergeev. *Sov. Phys. JETP*, **63**:616, 1986. 5

[37] A. Y. Sergeev and V. Mitin. *Phys. Rev. B*, **61**:6041, 2000. 5, 63

[38] A. Y. Sergeev and V. Mitin. *Europhys. Lett.*, **51**:641, 2000. 5, 63

[39] E. M. Q. Jariwala P. Mohanty and R. A. Webb. *Phys. Rev. Lett.*, **78**:3366, 1997. 6

[40] Gassem M. Alzoubi and Norman O. Birge. *Phys. Rev. Lett.*, **97**:226803, 2006. 6, 70

[41] A. Anthore H. Pothier D. Esteve F. Pierre, A. B. Gougam and Norman O. Birge. *Phys. Rev. B*, **68**:085413, 2003. 6

[42] W. Rabaud F. Schopfer, C. Bäuerle and L. Saminadayar. *Phys. Rev. Lett.*, **90**:056801, 2003. 6

[43] J. J. Lin and J. P. Bird. *J. Phys. Condens. Matter*, **14**:R501, 2002. 6

[44] J. J. Lin and L. Y. Kao. *J. Phys. Condens. Matter*, **13**:L119, 2001. 6, 78

[45] P. Mohanty and R. A. Webb. *Phys. Rev. Lett.*, **91**:066604, 2003. 6, 7

[46] F. Pierre and Norman O. Birge. *Phys. Rev. Lett.*, **89**:206804, 2002. 6

[47] Norman O. Birge H. Pothier B. Huard, A. Anthore and D. Esteve. *Phys. Rev. Lett.*, **95**:036802, 2005. 6

[48] Jan von Delft A. Zawadowski and D. C. Ralph. *Phys. Rev. Lett.*, **83**:2632, 1999. 6, 23, 77

[49] K. H. Ahn and P. Mohanty. *Phys. Rev. B*, **63**:195301, 2001. 6

[50] A. D Zaikin D. S Golubev, C. P Herrero. *Europhys. Lett.*, **63**:426, 2002. 6

[51] Dmitrii S. Golubev and Andrei D. Zaikin. *Phys. Rev. Lett.*, **81**:1074, 1998. 6

[52] B. L. Altshuler I. L. Aleiner and Y. M. Galperin. *Phys. Rev. B*, **63**:201401, 2001. 6

[53] J. Kroha and A. Zawadowski. *Phys. Rev. Lett.*, **88**:176803, 2002. 6, 23

[54] A. Zawadowski L. Borda and G. Zarand. *Europhys. Lett.*, **63**:426, 2002. 6

[55] Y. M. Galperin V. L. Gurevich V. V. Afonin, J. Bergli and V. I. Kozub. *Phys. Rev. B*, **66**:165326, 2002. 6

[56] H. Fukuyama Y. Imry and P. Schwab. *Europhys. Lett.*, **47**:608, 1999. 6, 23

[57] H. Pothier D. Esteve A. B. Gougam, F. Pierre and N. O. Birge. *J. Low Temp. Phys.*, **118**:447, 2000. 7

[58] F. Pierre. *Ann. Phys.*, **26**:4, 2001. 7

[59] P. Mohanty and R. A. Webb. *Phys. Rev. Lett.*, **84**:4481, 2000. 7

[60] J. Vranken C. Van Haesendonck and Y. Bruynseraede. *Phys. Rev. Lett.*, **58**:1968, 1987. 7

[61] C. Van Haesendonck J. Vranken and Y. Bruynseraede. *Phys. Rev. B*, **37**:8502, 1988. 7

[62] R. Niewa A. Schlechte Yu. Prots F. Steglich R. Kniep M. Schmidt, T. Cichorek. *J. Phys. Condens. Matter*, **17**:5481, 2005. 7, 77

[63] A. Jakovác O. Újsághy and A. Zawadowski. *Phys. Rev. Lett.*, **72**:205119, 2005. 7

[64] Z. Ovadyahu. *J. Phys. C*, **16**:L845, 1983. 7, 78

[65] Z. Ovadyahu. *Phys. Rev. Lett.*, **52**:569, 1984. 7, 78

[66] Z. Ovadyahu. *Phys. Rev. B*, **63**:235403, 2001. 7, 78

[67] J. Custers P. Gegenwart F. Steglich Z. Henkie Eric D. Bauer T. Cichorek, H. Aoki and M. Brian Maple. *Phys. Rev. B*, **68**:144411, 2003. 7

[68] P. Gegenwart F. Weickert A. Wojakowski Z. Henkie G. Auffermann S. Paschen R. Kniep T. Cichorek, A. Sanchez and F. Steglich. *Phys. Rev. Lett.*, **94**:236603, 2005. 7, 77

[69] P. Chaudhari and H. U. Habermeier. *Solid State Commun.*, **34**:687, 1980. 8

[70] Y. L. Zhong J. J. Lin and T. J. Li. *Europhys. Lett.*, **57**:872, 2002. 8

[71] G. Stephan and G. Bergmann. *Phys. Rev. Lett.*, **68**:2520, 1992. 14

[72] H. Fukuyama and K. Hoshino. *J. Phys. Soc. Jpn.*, **50**:2131, 1981. 16

[73] B. I. Halperin P. W. Anderson and C. M. Varma. *Philos. Mag.*, **25**:1, 1972. 22

[74] W. A. Phillips. *J. Low Temp. Phys.*, **7**:161, 1971. 22

[75] J. O. Strom-Olsen R. W. Cochrane, R. Harris and M. J. Shraiman. *Phys. Rev. Lett.*, **35**:676, 1975. 23, 77

[76] J. Kondo. *Physica B*, **84**:40, 1976. 23

[77] J. Kondo. *Physica B*, **84**:207, 1976. 23

[78] P. A. Lee E. Abrahams, P. W. Anderson and T. V. Ramakrishnan. *Phys. Rev. B*, **24**:6783, 1981. 60

[79] H. Fukuyama and E. Abrahams. *Phys. Rev. B*, **27**:5976, 1983. 60

[80] J. von Delft G. Zarand, L. Borda and N. Andrei. *Phys. Rev. Lett.*, **93**:107204, 2004. 69

[81] T. A. Costi T. Micklitz and A. Rosch. *Phys. Rev. B*, **75**:054406, 2005. 69

[82] T. A. Costi T. Micklitz, A. Altland and A. Rosch. *Phys. Rev. Lett.*, **96**:226601, 2005. 69

[83] T. A. Costi T. Micklitz and A. Rosch. *Phys. Rev. Lett.*, **75**:054406, 2007. 69

[84] F. Schopfer D. Mailly-G. Eska C. Bäuerle, F. Mallet and L. Saminadayar. *Phys. Rev. Lett.*, **95**:266805, 2005. 70

[85] D. Mailly S. Unlubayir-D. Reuter A. Melnikov A. D. Wieck T. Micklitz A. Rosch T. A. Costi L. Saminadayar F. Mallet, J. Ericsson and C. Bäuerle. *Phys. Rev. Lett.*, **97**:226804, 2006. 70

[86] F. Mallet Y. Baines-D. Mailly F. Y. Lo A. Melnikov A. D. Wieck L. Saminadayar T. Capron, Y. Niimi and C. Bäuerle. *Phys. Rev. Lett.*, **77**:033102, 2008. 70

[87] V. I. Kozub Y. M. Galperin and V. M. Vinokur. *Phys. Rev. B*, **69**:073102, 2004. 78

[88] H. Akimoto-K. Kono S. M. Huang, T. C. Lee and J. J. Lin. *Phys. Rev. Lett.*, **99**:046601, 2007. 78

[89] B. Dóra and M. Gulácsi. *arXiv:0806.1680v1*, 2008. 80

[90] M. D. Barrett. *Nature*, **429**:737, 2004. 83

[91] C. F. Roos W. Hansel J. Benhelm G. P. T. Lancaster T. W. Korber C. Becher F. Schmidt-Kaler D. F. V. James M. Riebe, H. Haffner and R. Blatt. *Nature*, **429**:734, 2004. 83

[92] Y. Monarkha H. Akimoto K. Shirahama D. Konstantinov, H. Isshiki and K. Kono. *Phys. Rev. Lett.*, **98**:235302, 2007. 83

[93] J. I. Cirac and P. Zoller. *Phys. Rev. Lett.*, **74**:4091, 1995. 83

[94] G. Schon Y. Makhlin and A. Shnirman. *Rev. Mod. Phys.*, **73**:357, 2001. 83

[95] Y. Tokura K. Ono, D. G. Austing and S. Tarucha. *Science*, **297**:1313, 2002. 83

[96] M. P. Hanson A. C. Johnson, C. M. Marcus and A. C. Gossard. *Phys. Rev. B*, **71**:115333, 2005. 83

[97] L. H. Willems van Beveren B. Witkamp L. M. K. Vandersypen J. M. Elzerman, R. Hanson and L. P. Kouwenhoven. *Nature*, **430**:431, 2004. 83

[98] C. M. Marcus M. P. Hanson J. R. Petta, A. C. Johnson and A. C. Gossard. *Phys. Rev. Lett.*, **93**:186802, 2004. 83

[99] D. G. Austing L. P. Kouwenhoven and S. Tarucha. *Rep. Prog. Phys.*, **64**:701, 2001. 83, 90

[100] P. L. McEuen Y. Nagamune J. Motohisa D. C. Dixon, L. P. kouwenhoven and H. Sakaki. *Phys. Rev. B*, **53**:12625, 1996. 83

[101] Yu. V. Nazarov C. J. P. M. Harmans N. C. van der Vaart, S. F. Godijn and J. E. Mooij. *Phys. Rev. Lett.*, **74**:4702, 1995. 83

[102] W. G. van der Wiel B. W. Broer R. Aguado S. Tarucha T. Fujisawa, T. H. Oosterkamp and L. P. kouwenhoven. *Science*, **282**:932, 1998. 83

[103] E. I. Rashba C. M. Marcus M. P. Hanson E. A. Laird, C. Barthel and A. C. Gossard. *Phys. Rev. Lett.*, **99**:246601, 2007. 83, 128, 147

[104] A. C. Johnson A. Yacoby M. D. Lukin C. M. Marcus M. P. Hanson J. R. Petta, J. M. Taylor and A. C. Gossard. *Phys. Rev. Lett.*, **100**:067601, 2008. 83, 115

[105] M. Pioro-Ladriere Y. Tokura S. Tarucha N. Lambert, I. Mahboob and H. Yamaguchi. *Phys. Rev. Lett.*, **100**:136802, 2008. 83

[106] D. V. Averin and K. K. Likharev. *J. Low Temp. Phys.*, **62**:345, 1986. 87

[107] C. G. Darwin. *Cambridge Philos. Soc.*, **27**:86, 1930. 88

[108] V. Fock. *Z. Phys.*, **47**:446, 1928. 88

[109] P. Pieriläinen V. Halonen, P. Hyvönen and Tapash Chakraborty. *Phys. Rev. B*, **53**:6971, 1996. 88

[110] J. E. B. Katari S. Tarucha R. M. Westervelt L. P. kouwenhoven, C. M. McEuen and N. S. Wingreen. *mesoscopic Electron Transport*, volume **345**. Kluwer, Series E, 1997. 90

[111] Y. Tokura Y. Hirayama T. Fujisawa, D. G. Austing and S. Tarucha. *Phys. Rev. Lett.*, **88**:236802, 2002. 97

[112] P. L. McEuen Y. Nagamune J. Motohisa D. C. Dixon, L. P. kouwenhoven and H. Sakaki. *Phys. Rev. B*, **53**:12625, 1996. 97

[113] C. Urbina D. Estéve H. Pothier, P. Lafarge and M. H. Devoret. *Europhys. Lett.*, **17**:249, 1992. 97

[114] E. I. Levin I. M. Ruzin, V. Chandrasekhar and L. I. Glazman. *Phys. Rev. B*, **45**:13469, 1992. 97, 131

[115] S. Tarucha T. Fujisawa. *Appl. Phy. Lett.*, **68**:526, 1996. 97

[116] M. Suzuki Y. Aoyagi S. Moriyama, T. Fuse and K. Ishibashi. *Phy. Rev. Lett.*, **94**:186806, 2005. 105

[117] K. Honkala M. Walter, P. Frondelius and H. Hakkinen. *Phy. Rev. Lett.*, **99**:096102, 2007. 105

[118] K. Ensslin A. Pfund, I. Shorubalko and R. Leturcq. *Phy. Rev. Lett.*, **99**:036801, 2007. 105

[119] J. S. Greidanus L. H. Willems van Beveren S. de Franceschi L. M. K. Vandersypen S. Tarucha J. M. Elzerman, R. Hanson and L. P. Kouwenhoven. *Phys. Rev. B*, **67**:161308(R), 2003. 105

[120] L. H. Willems van Beveren L. M. K. Vandersypen J. M. Elzerman, R. Hanson and L. P. Kouwenhoven. *Phys. Rev. Lett.*, **84**:4617, 2004. 105

[121] Y. Tokura K. Ono, D. G. Austing and S. Tarucha. *Physica B*, **314**:450, 2002. 105, 131, 137

[122] C. W. J. Beenakker. *Phys. Rev. B*, **44**:1646, 1991. 106

[123] A. V. Khaetskii and Y. V. Nazarov. *Phys. Rev. B*, **61**:12639, 2000. 114

[124] D. Loss and D. P. DiVincenzo. *Phys. Rev. A*, **57**:120, 1998. 114, 128, 147

[125] R. A. Buhrman J. M. Daughton S. von Molnar M. L. Roukes A. Y. Chtchelkanova S. A. Wolf, D. D. Awschalom and D. M. Treger. *Science*, **294**:1488, 2001. 114, 128

[126] Y. Tokura Y. Hirayama T. Fujisawa, D. G. Austing and S. Tarucha. *Nature (London)*, **419**:278, 2002. 114, 137

[127] P. Hawrylak C. Gould P. Zawadzki S. Jullian Y. Feng M. Ciorga, A. S. Sachrajda and Z. Zasilewsli. *Phys. Rev. B*, **61**:R16315, 2000. 114

[128] H. Ohon. *Science*, **281**:951, 1998. 114

[129] J. S. Weiner L. N. Pfeiffer S. J. pearton K. W. Baldwin R. C. Ashoori, H. L. Stormer and K. W. West. *Phys. Rev. Lett.*, **68**:3088, 1992. 114

[130] C. M. Marcus V. Umansky M. Hanson R. M. Potok, J. A. Folk and A. C. Gossard. *Phys. Rev. Lett.*, **91**:016802, 2003. 114, 125

[131] D. G. Austing S. Sasaki and S. Tarucha. *Appl. Phys. Lett.*, **77**:2183, 2000. 114

[132] Y. Hirayama H. D. Cheong T. Fujisawa, T. Hayashi and Y. H. Jeong. *Appl. Phys. Lett.*, **84**:2343, 2004. 114

[133] M. W. S. Danoesastro M. Eto D. G. Austing T. Honda L. P. Kouwenhoven, T. H. Oosterkamp and S. Tarucha. *Science*, **278**:1788, 1997. 115

[134] T. Honda R. J. van der Hage S. Tarucha, D. G. Austing and L. P. Kouwenhoven. *Phys. Rev. Lett.*, **77**:3613, 1996. 115

[135] M. Pioro-Ladriere M. Korkusinski J. Kyriakidis A. S. Sachrajda M. Ciorga, A. Wensauer and P. Hawrylak. *Phys. Rev. Lett.*, **88**:256804, 2002. 115

[136] G. Shinkai T. Fujisawa and T. Hayashi. *Phys. Rev. B*, **76**:041302(R), 2007. 115

[137] L. H. Willems van Beveren J. M. Elzerman I. T. Vink R. Hanson, L. M. K. Vandersypen and L. P. Kouwenhoven. *Phys. Rev. B*, **70**:241304(R), 2004. 115, 125, 134, 137

[138] D. G. Austing S. Tarucha D. V. Melnikov, T. Fujisawa and J.-P. Leburton. *arXiv:0707.4271v1*. 117

[139] J. M. Elzerman W. G. van der Wiel S. Tarucha S. De. Franceschi, S. Sasaki and L. P. Kouwenhoven. *Phys. Rev. Lett.*, **86**:878, 2001. 117, 131

[140] M. Eto. *Jpn. J. Appl. Phys.*, **36**:3924, 1997. 117

[141] U. Merkt M. Wagner and A. V. Chaplik. *Phys. Rev. B*, **45**:1951, 1992. 117

[142] J. W. Janssen L. P. Kouwenhoven D. G. Austing T. Honda W. G. van der Wiel, T. H. Oosterkamp and S. Tarucha. *Physica B*, **258**:173, 1998. 121

[143] W. HaLusler D. Weinmann and B. Kramer. *Phys. Rev. Lett.*, **74**:984, 1995. 122

[144] L. M. K. Vandersypen L. H. Willems van Beveren J. M. Elzerman R. Hanson, B. Witkamp and L. P. Kouwenhoven. *Phys. Rev. Lett.*, **91**:196802, 2003. 123, 125

[145] I. T. Vink F. H. L. Koppens L. P. Kouwenhoven L. H. Willems van Beveren, R. Hanson and L. M. K. Vandersypen. *New J. Phys.*, **7**:182, 2005. 125

[146] C. Weisbuch and C. Hermann. *Phys. Rev. B*, **15**:816, 1997. 125

[147] K. Kono J. J. Lin S. Tarucha S. M. Huang, H. Akimoto and K. Ono. *Jpn. J. Appl. Phys.*, **47**:3257, 2008. 125

[148] N. Samarth D. D. Awschalom and D. Loss, editors. *Semiconductor Spintronics and Quantum Computation.* Springer-Verlag, Berlin, Germany, 2002. 128

[149] D. P. DiVincenzo and D. Loss. *J. Magn. Magn. Mater.*, **200**:202, 1999. 128, 147

[150] H. A. Engel and D. Loss. *Phys. Rev. Lett.*, **86**:20, 2001. 128

[151] K. Ensslin D. C. Driscoll A. C. Gossard G. Salis, Y. Kato and D. D. Awschalom. *Nature*, **414**:619, 2001. 128

[152] D. C. Driscoll A. C. Gossard J. Levy Y. Kato, R. C. Myers and D. D. Awschalom. *Science*, **299**:1201, 2003. 128

[153] T. Honda D. G. Austing and S. Tarucha. *Jpn. J. Appl. Phys.*, **36**:1667, 1997. 131

[154] M. Kemerink and L. W. Molenkamp. *Appl. Phys. Lett.*, **65**:1012, 1994. 131

[155] W. G. van der Wiel K. Ishibashi R. V. Hijman S. Tarucha T. H. Oosterkamp, T. Fujisawa and L. P. Kouwenhoven. *Nature*, **395**:873, 1998. 134

[156] T. H. Stoof and Yu. V. Nazarov. *Phys. Rev. B*, **53**:1050, 1996. 140

[157] T. Tokura. *to be Published*. 140

[158] C. Weisbuch and C. Hermann. *Phys. Rev. B*, **51**:816, 1977. 147

[159] M. Bayer R. Kotlyar, T. L. Reinecke and A. Forchel. *Phys. Rev. B*, **63**:85310, 2001. 147

[160] O. Baklenov A. L. Holmes Jr. N. Liu, J. Tersoff and C. K. Shih. *Phys. Rev. Lett.*, **84**:334, 2000. 147